CONSTRAINTS AND APPLICATIONS OF U-TH SYSTEMATICS TO CLIMATE RECONSTRUCTIONS

A Dissertation

by

MATTHEW ROBERT LOVELEY

Submitted to the Office of Graduate and Professional Studies of
Texas A&M University
in partial fulfillment of the requirements for the degree of

DOCTOR OF PHILOSOPHY

Chair of Committee,	Franco Marcantonio
Committee Members,	Mitchell Lyle
	Brendan Roark
	Brent Miller
Head of Department,	Mike Pope

August 2017

Major Subject: Geology

ABSTRACT

The objective of this dissertation is to understand the dynamics of U-Th isotope behavior in deep sea marine sediment cores extracted from the Panama Basin located in the eastern Equatorial Pacific. Specifically, I attempt to further our understanding of the potential biases inherent in these proxies which are used to reconstruct past global climate change (export production, continental aridity, atmospheric circulation, deep-ocean circulation) over the past several hundred thousand years.

First, I have investigated the effects that biasing of specific grain size fractions during deep-sea sediment redistribution processes have on the ^{230}Th-normalization technique. This method is used frequently in the paleoceanographic community to reconstruct past changes in a number of climate-related processes. Recent studies have shown that sediment fluxes calculated by the ^{230}Th method may be biased because of the fractionation of ^{230}Th-enriched fine-grained particles (i.e. clay-sized) during sediment focusing processes. The results of my study show that there is biasing of ^{230}Th-normalized sediment fluxes at sites that have experienced extremes in sediment redistribution both spatially and temporally. However, in general terms, the biasing remains insufficient to alter interpretations estimated by this method, especially when corrections of biasing can be made.

Secondly, I have investigated the use of redox-sensitive authigenic uranium in marine sediments over the past 25 kyr in the Panama Basin. Authigenic U has been used previously as both a proxy for biologic productivity and bottom water oxygen content.

However, the ability to directly separate out which process controls the distribution of authigenic U at our Panama Basin sites is essential to reconstructing past climate conditions. It appears at our Panama Basin sites, only 1 of the 4 cores analyzed remain unaffected by early sediment diagenesis (i.e. burn down of relict organic carbon and migration of the uranium signal to shallower or deeper depths).

Thirdly, I have applied a multiproxy approach to investigate the relationship shared between global climate and the iron fertilization hypothesis on millennial time scales. The Panama Basin is a region where biologic productivity is limited by essential micronutrients (i.e. iron). I suggest that through increased deposition and dissolution of continentally-derived material (i.e. dust that is rich in iron), iron limitation within the Panama Basin is relaxed and biological productivity is increased. For the first time, I present multiple proxy records that suggest increases in productivity are correlated with increases in both upwelling and increased deposition of iron through the dissolution of dust. The timing of each of these increases is tightly linked to Northern Hemisphere Heinrich stadial events.

CONTRIBUTORS AND FUNDING SOURCES

This dissertation and the studies conducted within were designed by Matthew Loveley and Franco Marcantonio. Matthew Loveley sampled the cores, and performed the U-Th isotope analyses with help of Luz Romero. Matthew Loveley and Marilyn Wisler performed the Ba analyses with help of Luz Romero. Matthew Loveley separated the foraminifera for oxygen isotope analysis and analyzed with the help of Chris Maupin. Matthew Loveley and Jennifer Hertzberg separated the foraminifera for radiocarbon analysis. All committee members provided comments and revisions. We especially thank Luz Romero for her technical assistance in the lab.

This research was funded by NSF grant OCE-0851056 to Franco Marcantonio and Mitch Lyle. Additional financial support was provided to Franco Marcantonio by the Jane and R. Ken Williams Chair in Ocean Drilling Science, Technology, and Education.

DEDICATION

This dissertation is dedicated to my mother and in loving memory to my father who always asked how my dirt was going. This could never have been accomplished if I did not have the support, continued enthusiasm, and encouragement of either for my success and accomplishments.

ACKNOWLEDGEMENTS

I am especially thankful for my mentor, Dr. Franco Marcantonio. Without Franco's hunger for my own personal success and his need for "more data!", this dissertation would have never come to full fruition. I am truly and greatly appreciative of the time, patience, investment, and especially the friendship we established over the course of my education. I would like to thank my committee members, Dr. Mitch Lyle, Dr. Brent Miller, and Dr. Brendan Roark for their constructive criticism, guidance and insights throughout the course of my research.

I would like to extend my unyielding gratitude to the Department of Geology & Geophysics at Texas A&M University for the facilities, financial support (Ocean Drilling and Sustainable Earth Science Fellowship and numerous departmental scholarships) and education. My success would not have been guaranteed without the foundations established by the department. I would also like to thank the Oregon State University Core Repository for the use of their lab facilities for sample storage and collection.

I would like to extend a most sincere and special appreciation to Grecia Ivonne Lopez, Maya Reimi, Jennifer Hertzberg for their intellectual help and friendship. I would also like to extend a most singular gratefulness to Luz Romero for her expertise, guidance, and friendship throughout the course of my scientific ventures.

TABLE OF CONTENTS

LIST OF FIGURES

Page

LIST OF TABLES

Page

CHAPTER I

INTRODUCTION

The knowledge and accurate quantification of marine sediment fluxes to the deep ocean are quintessential for the reconstruction of past climatic and oceanographic conditions through time. Over recent geologic time, the Earth has progressed through extended periods of Milankovitch-regulated warm (i.e. interglacials) and cool (glacial) climates. However, during the last glacial, on millennial time scales, there have even been abrupt global cooling events (i.e. Heinrich events) that are thought to be controlled by changes in North Atlantic deep-ocean circulation, specifically the shutdown of the Atlantic Meridional Overturning Circulation (AMOC). These millennial changes in North Atlantic AMOC are related to changes in 1) atmospheric circulation, manifest by decreases in the northern hemisphere monsoon which are related to southern shifts in the intertropical convergence zone (ITCZ), and 2) ventilation of Southern Ocean intermediate-deep waters which is related to increases in the CO_2 content of the atmosphere.

My goal in this dissertation is to investigate high-resolution sediments of the Eastern Equatorial Pacific (EEP) using U-Th isotope systematics in order to further our understanding of the low-latitude connection to the high-latitude events that seem to play such a crucial role in driving climate change on a planetary scale. However, before applying the U-Th system, a clearer understanding of the way the ^{230}Th and authigenic uranium proxies work is necessary. For the ^{230}Th proxy I tackle the important problem

of sediment redistribution processes and how the fractionation of fine-grained sediments bias the bulk ^{230}Th concentrations and, potentially, estimated sediment mass accumulation rates (Chapter 2). For the authigenic uranium proxy, I attempt to address the problem of diagenesis on the redox behavior of uranium in different sedimentary environments (Chapter 3). In Chapter 4, I apply the knowledge garnered from Chapters 1 and 2, and extend them to a high-resolution (sub-millennial) study of climate variability in the EEP.

CHAPTER II

SEDIMENT REDISTRIBUTION AND GRAIN SIZE EFFECT OF ^{230}TH NORMALIZED FOCUSING FACTORS AND MASS ACCUMULATION RATES IN THE PANAMA BASIN

Introduction

The knowledge and accurate quantification of marine sediment fluxes in the deep ocean are pivotal to reconstructing past oceanographic conditions. The Eastern Equatorial Pacific (EEP) has been a region of intense study for many researchers because some of the highest rates of primary productivity in the world occur here (Chavez and Barber 1987, Murray et al., 1994, Pennington et al., 2006, Thomas et al., 2000). Within the EEP, changes in the fluxes of calcium carbonate (Anderson et al., 2008; Loubere et al., 2004; Loubere and Richaud, 2007; Lyle et al., 2002; Marcantonio et al., 2014; Mekik et al., 2012), opal (Bradtmiller et al., 2009, Dubois et al., 2010, Hays et al., 2011, Kienast et al., 2006, 2007, Marcantonio et al., 2014), barium (Dean et al., 1997, Francois et al., 1995, Marcantonio et al., 2001, Paytan et al., 1997), and dust (McGee et al., 2007, Singh et al., 2011) have been used to interpret past changes in productivity, carbonate dissolution, sediment redistribution, and dust fluxes on glacial-interglacial timescales. Many of these studies used the ^{230}Th technique for estimating changes in fluxes through time.

^{230}Th is produced in the water column at a rate of 0.0267 dpm m^{-3} yr^{-1} by the radioactive decay of ^{234}U, which is dissolved ubiquitously in the world's oceans. ^{230}Th

is a particle reactive isotope with a short residence time in the water column (decades; Bacon and Anderson, 1982) compared to its parent isotope, ^{234}U (200-400 kyr; Henderson et al., 2002). Dissolved ^{230}Th is rapidly scavenged by sinking particulates and deposited on the seafloor. It is often assumed that the flux of ^{230}Th that reaches the seafloor is equal to its production rate in the overlying water column, so that the mass accumulation rate (MAR) of marine sediments can be determined. A corollary of the thorium methodology is that the flux of vertically "rained" particles from the surface ocean can be differentiated from the flux of laterally advected sediments along the seafloor. This corollary leads to the definition of a focusing factor (Suman and Bacon, 1989), Ψ, which quantifies syndepositional lateral addition (i.e., $\Psi>1$) or removal (i.e., $\Psi<1$) of sediment to a site that has experienced redistribution by deep-sea currents.

A key assumption of the ^{230}Th method for determining bulk sediment MARs is that there is no fractionation of sediment composition in sediment that has been differentially redistributed. Yet, it is well known that sediment drift deposits, for example, have much higher concentrations of fine-grained sediments, which often have a distinct chemical composition from the bulk sediment. This may cause a problem in using ^{230}Th in regions that have undergone focusing because ^{230}Th is preferentially contained in the finest grained sediment fraction (Thomson et al., 1993). However, only a few studies have addressed this grain size effect and its effect on ^{230}Th-normalized MARs and focusing factors (Thomson et al., 1993; McGee et al., 2010; Kretschmer et al., 2010). The grain size study of Kretschmer et al. (2010) demonstrated that between 50 and 90% of the $xs^{230}Th$ was found in the finest fraction (<2 μm). They determined

that sites that had experienced large degrees of focusing overestimated focusing factors and underestimated MARs to a greater extent than sites at which smaller degrees of focusing had occurred. However the extent to which focusing factors and MARs needed to be corrected amounted to no more than 25%.

In the Panama Basin of the EEP there has been controversy over the extent of sediment focusing and its effect on the ^{230}Th proxy, mainly because some of the largest sediment focusing factors in the open ocean were discovered there (e.g., Singh et al. 2011 and references therein). Recent work by Marcantonio et al. (2014) on the Cocos and Carnegie Ridges has shown that although the ^{230}Th-derived fluxes for late Holocene sediments are not biased when determining the fluxes of fine-grained (<63 μm) sedimentary components, the same cannot be said for the fluxes of the coarser-grained (>63 μm) fraction. In addition, Lyle et al (2014) showed that significant excess ^{230}Th was trapped in near-bottom sediment traps in the equatorial Pacific, along with excess Al presumably from resuspended clays. However, the largest captured ^{230}Th fluxes occurred not when currents were strongest but when the largest vertical sediment fluxes occurred, indicating scavenging of near-bottom particle field by high particle rain rates.

Here, we add to the study of Marcantonio et al. (2014) in two ways. From the same paired Panama Basin sites used in that study: 1) we measure ^{230}Th, ^{232}Th, and ^{238}U in several different grain size classes (<4 μm, 4-20 μm, 20-63 μm, and >63 μm) and 2) investigate the differences in the U-Th systematics of the different grain sizes between Holocene and LGM time slices. The paired cores at each site represent areas that have undergone varying degrees of sediment redistribution. Hence, our goal is to determine

the extent ^{230}Th-derived fluxes are biased by grain size effects both spatially and temporally.

Seismic Surveys and Site Sampling

Research cruise MV1014 (*RV Melville*, Oct. 2010) conducted seismic surveys along Cocos and Carnegie Ridges to identify potential sediment redistribution and independently estimate regional sedimentation (Figure 2-1; Liao and Lyle, 2014; Brooks, 2014). Paired core locations near each ridge were identified at which winnowing and focusing likely occurred. The two ridges provide different sedimentation regimes. The Carnegie Ridge sits close to the equator in a zone of high primary productivity and upwelling. The Cocos Ridge, at ~6°N (4JC and 8JC, Figure 2-1), is located in a region where, primary productivity and upwelling are significantly lower. However, the Cocos Ridge site is near the core of the P-E maximum that marks the Intertropical Convergence Zone (Fiedler and Talley, 2006). Two core sites at each ridge were chosen based on seismic evidence that indicated either potential winnowing (zones that show pinching closer to ridge crests), or focusing (where there are thick sediment piles closer to the basin center). The potential winnowed or "thin" sites are represented by sediment cores 4JC and 11JC, while the potential focused or "thick" sites are represented by sediment cores 8JC and 17JC from the Cocos and Carnegie Ridges, respectively (Figure 2-1). Throughout this work, we prefer the use of "thin" and "thick" to refer to the core site sediment thicknesses, rather than winnowed or focused, as they refer only to observations and not interpretations. Furthermore references to "thin versus thick sites,"

are short-hand notation for “core site at which there is a thinner (and potentially winnowed) sediment pile” versus “core site at which there is a thicker (and potentially focused) sediment pile.”

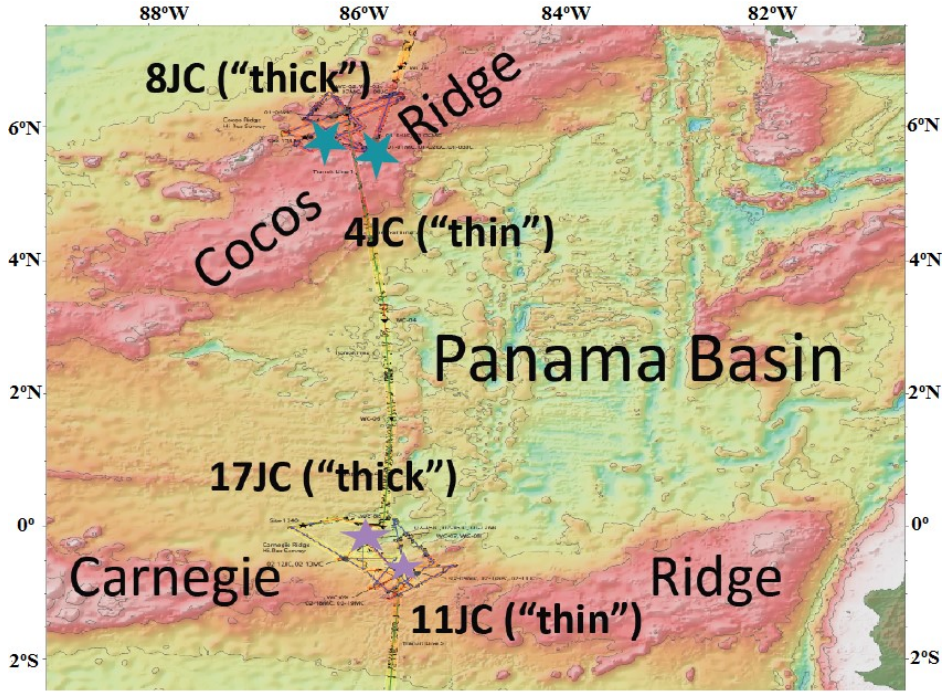

Figure 2-1
Jumbo piston sediment core locations from seismically identified thin and thick Cocos (blue stars) and Carnegie (purple stars) sites in the Panama Basin.

Chronology

Independent age models were constructed using monospecific $\delta^{18}O$ stratigraphy and radiocarbon age dating of the planktonic foraminifer, *Neogloboquadrina dutertrei.*

For oxygen isotope analyses, ~10 *N. dutertrei* (~150 μg) were picked and analyzed in the laboratory of Dr. Jean Lynch-Stieglitz at the Georgia Institute of Technology.

Radiocarbon analyses were performed at the NOSAMS site at the Woods Hole Oceanographic Institute (Table 2-1). Approximately 4-6 mg of N. *dutertrei* were picked from the >250 μm size fraction for radiocarbon analysis, following the same cleaning procedures for oxygen isotope analysis. Radiocarbon ages were converted to calendar ages using Calib 7.0 (Stuiver et al., 2006) with a marine reservoir age correction of 400 years.

MV1014-01-08JC

The age model for Cocos Ridge core MV1014-01-08JC is based on 7 radiocarbon dates (Table 2-1). Ages at sample depths 61 cm, 81 cm and 101 cm were previously published by Hertzberg et al. (2016). Linear interpolation between radiocarbon age control points was used to construct our age model that spans the Holocene to the LGM.

MV1014-01-04JC

The age model for Cocos Ridge core MV1014-01-04JC is based on 3 radiocarbon dates (Table 2-1). The upper most core section (<10 cm) was disturbed and partly lost during coring, thus, our age model starts at 10 cm depth. This assumption is based on comparison with authigenic U data from a nearby, paired multicore (1MC;

Marcantonio et al., 2014). Linear interpolation between radiocarbon age control points was used to construct our age model that spans the early Holocene until late MIS 3.

MV1014-02-17JC

The age model for Carnegie Ridge core MV1014-02-17JC is based on 7 radiocarbon (Table 2-1). Ages at sample depths 220 cm and 356.5 cm were previously published by Hertzberg et al. (2016). The core-top (0-2 cm) age was set to zero based on paired multicore data (16MC; Marcantonio et al., 2014). Linear interpolation between radiocarbon age control points was used to construct our age model that spans the Holocene to the LGM.

Interval	Depth (cm)	^{14}C age (yrs)	^{14}C age error ± (yrs)	Assension #	Mean Probability (yrs)	Range
Carnegie Ridge						
MV1014-02-17JC 40-41cm	40.5	3710	20	OS-119712	3627	3555-3699
MV1014-02-17JC 160-162cm	161	11150	35	OS-119853	12653	12573-12742
MV1014-02-17JC 210-212cm	211	13750	45	OS-119852	16058	15866-16238
MV1017-02-17JC 219-221cm	220	14350	60	OS-98923	16916*	16628 - 17145
MV1014-02-17JC 270-272cm	271	17850	65	OS-119864	21060	20829-21316
MV1014-02-17JC 300-301cm	300.5	18100	70	OS-119865	21415	21121-21693
MV1014-02-17JC 356-357cm	356.5	23800	180	OS-117129	27592*	27322 - 27848
Cocos Ridge						
MV1014-01-08JC 0-2cm	1	1570	20	OS-97690	1132	1054-1209
MV1014-01-08JC 5-7cm	6	1960	25	OS-97824	1504	1413-1594
MV1014-01-08JC 30-32cm	31	9270	45	OS-97830	10070	9932-10208
MV1014-01-08JC 40-42cm	41	11450	55	OS-97831	12913	12723-13102
MV1014-01-08JC 60-62cm	61	14600	80	OS-97832	17278*	16949-17606
MV1014-01-08JC 80-82cm	81	17750	110	OS-97822	20728*	20278-21177
MV1014-01-08JC 100-102cm	101	20200	150	OS-97823	23702*	23226-24178
MV1014-01-04JC 10-12cm	11	7990	40	OS-97691	8454	8365-8542
MV1014-01-04JC 19-21cm	20	17000	100	OS-97826	19766	19448-20084
MV1014-01-04JC 31-33cm	32	35800	980	OS-97688	40384	39375-41392

Table 2-1
Mean probable ages of Carnegie Ridge thick site (17JC) and Cocos Ridge thin (4JC) and thick (8JC) site. ^{14}C dates and ^{14}Cage errors as reported by NOSAMS. (*) denotes published radiocarbon dates from Hertzberg et al., (2016).

MV1014-02-11JC

The age model for Carnegie Ridge core MV1014-02-11JC is based on a $\delta^{18}O$ stratigraphy. Tie-points to marine isotope stage (MIS) 1/MIS 2 and MIS 2/MIS 3 boundaries were estimated, and a constant sedimentation rate is assumed between tie-points to construct an age vs depth relationship (Table 2-2). The N. *dutertrei* oxygen isotope data for core 11JC appear in the supplementary information section (Table 2-2).

Core ID	Depth (cm)	$\delta^{18}O$ (PDB)
MV1014-02-11JC	1	0.24
MV1014-02-11JC	11	0.45
MV1014-02-11JC	21	0.58
MV1014-02-11JC	31	0.66
MV1014-02-11JC	41	0.65
MV1014-02-11JC	51	0.89
MV1014-02-11JC	61	0.78
MV1014-02-11JC	71	1.56
MV1014-02-11JC	81	1.34
MV1014-02-11JC	91	1.52
MV1014-02-11JC	101	1.30
MV1014-02-11JC	111	1.56
MV1014-02-11JC	121	1.62
MV1014-02-11JC	131	1.22
MV1014-02-11JC	141	1.21
MV1014-02-11JC	151	1.28
MV1014-02-11JC	161	1.30
MV1014-02-11JC	171	0.93
MV1014-02-11JC	181	1.42
MV1014-02-11JC	191	0.99
MV1014-02-11JC	201	0.95

Table 2-2
Carnegie Ridge thin site (11JC) $\delta^{18}O$ N. *dutertrei* record.

Grain Size Separation Methods

Two time slices representative of the Holocene and LGM were selected for each piston core. Holocene time slices ages (from age models above) for 4JC, 8JC, 11JC, and 17JC were chosen for the early Holocene and were approximately 12, 10, 9, and 10 kyr in age, respectively. For the LGM time slices ages for 4JC, 8JC, 11JC, and 17JC were estimated to be approximately 20, 22, 18, and 21 kyr, respectively. Note, the 18 kyr sample for 11JC is slightly younger than the age of the LGM because samples at the LGM for this core were exhausted during the development of the grain size separation methodology.

Four grain-size fractions were separated for each time slice at both the Cocos and Carnegie Ridge sites. These grain sizes consisted of the >63 μm (sand), the 20-63 μm (silt/very fine sand), 4-20 μm (fine silt/mud) and <4 μm (clay) fractions. Approximately 2.5 g of bulk "wet" sediment was placed in a 50 mL centrifuge tube in a 5:1 volume ratio of Milli-Q water:sediment. Sediment was ultrasonicated for 45 seconds and centrifuged for 10 min at 1500 rpm. Washing and gentle ultrasonication was performed to remove any marine salts and break apart any existing aggregated clay particles. This process was repeated three times to fully ensure a clean and well-separated sample. To obtain a value for the dry bulk weight a separate aliquot of about 0.5 g was dried and weighed. Moisture loss from the 0.5 g sample should be proportional to the weight of "wet" sample. Particles >63 μm and 20-63 μm were wet-sieved using stacked 63 μm and 20 μm wire mesh sieves over a 400 mL glass beaker. Roughly 0.8-1 L of deionized (DI) water was passed through the sieves to fully separate the <20 μm fraction from each

sample. To separate the <20 μm fraction, two 500 mL graduated cylinders per sample were filled to the 420 mL mark with the collected 0.8-1 L sediment solution. The settling velocity used to extract the <4 μm fraction from the 4-20 μm fraction was 0.00087 cm s^{-1}. This rate was based on Stokes law for particles settling undisturbed in a viscous fluid. A calculated time of 4 hr 9 min was used to separate the <20 μm fraction into 4-20 μm and <4 μm size fractions. Then, a vacuum pump was used to siphon out the <4 μm sediment solution above 250 mL mark on the graduated cylinder, corresponding to the boundary between 4-20 μm and <4 μm size fractions. The settling velocity was modified to account for grain shape effects during settling (Gibbs et al., 1971; Komar & Reimers 1978; Wadell 1932; 1934). Each graduated cylinder was refilled with DI water to the 420 mL mark and vigorously stirred for 2 minutes before starting a new collection of sample. This process was repeated four times and corresponded to a distinctively low turbidity in the graduated cylinders above the 250 mL mark. Between each collection, the vacuum pump siphon was flushed for 5 minutes with DI water to prevent any sample retention in the tubing. Once separated, each grain size fraction was dried down in pre-weighed 250 mL Teflon beakers for uranium and thorium analysis.

U-Th Geochemistry

In addition to analyzing the grain size separates, bulk sediments for the same time intervals from each site (Cocos and Carnegie) were analyzed for uranium and thorium isotopes. For bulk U-Th analysis, a dried, approximate 2-gram aliquot of

sediment was gently homogenized using a mortar and pestle. For bulk and grain size fraction analysis, between 0.3 and 0.4 g of material was spiked with ^{229}Th and ^{236}U. Following dissolution with a mixture of $HClO_4$, HNO_3 and HF, and co-precipitation with Fe oxyhydroxides, the samples were purified for uranium and thorium by anion exchange chromatography (see Singh et al., 2011 for analytical details on uranium-thorium analyses). Uranium and thorium isotope ratios were measured on an *Element XR* magnetic sector ICP-MS at Texas A&M University.

Reproducibility, Blanks, and Uncertainties

Uncertainties in each analysis of thorium and uranium were calculated at the 1-sigma level. These include errors associated with uncertainties in spike weight, instrument drift, and counting statistics. Average 1-sigma values for thorium isotopes are <1% (^{230}Th, ±0.03 dpm g^{-1}, ^{232}Th, ±0.001 dpm g^{-1}) and <2% for uranium isotopes (^{234}U, ±0.03 dpm g^{-1}, ^{238}U, ±0.03 dpm g^{-1}). To correct of instrument drift throughout the run, the National Institute of Standards and Technology Uranium Standard (NIST U500) was measured before each new set of sediment core samples (n=5 standards per run). We assumed a similar mass fractionation between uranium and thorium. Average procedural blanks (n=6) contribute <1% to total measured activities for both uranium (^{234}U, 1.25x10^{-3} dpm g^{-1}, ^{238}U, 9.14x10^{-4} dpm g^{-1}) and thorium isotopes (^{230}Th, 1.03x10^{-2} dpm g^{-1}, ^{232}Th, 4.99x10^{-4} dpm g^{-1}). Duplicate runs of samples were limited (i.e. only four samples) due to limited sample materials at the Holocene and LGM time slices studied for each core.

Although reproducibility is low (i.e. higher % difference) between size fractions, the difference in weight is relatively small (i.e. tenths of a gram). Average % difference of thorium and uranium isotopes in each size fraction ranges between 14 and 24% (Table 2-3).

Core ID	Sample wt. (g)	^{230}Th activity (dpm g^{-1})	^{232}Th activity (dpm g^{-1})	^{238}U activity (dpm g^{-1})	Grain Size % Difference
MV1014-01 4JC 13-15 cm					
>63 µm	1.43	2.17	0.08	0.16	
20-63 µm	0.37	3.39	0.14	0.29	
MV1014-01 4JC 13-15cm					
>63 µm	1.18	2.24	0.08	0.14	19
20-63 µm	0.27	4.43	0.19	0.30	31
MV1014-01 4JC 16-18 cm					
>63 µm	1.64	1.04	0.07	0.10	
20-63 µm	0.09	1.97	0.25	0.39	
MV1014-01 4JC 16-18 cm					
>63 µm	1.6341	0.80	0.06	0.09	0.4
20-63 µm	0.1416	1.33	0.23	0.30	46
MV1014-01-08JC 20-22 cm					
>63 µm	0.26	1.76	0.06	0.08	
20-63 µm	0.2	5.83	0.27	0.32	
MV1014-01-08JC 20-22 cm					
>63 µm	0.36	2.15	0.05	0.11	32
20-63 µm	0.23	5.65	0.20	0.34	15
MV1014-01-17JC 60-62 cm					
>63 µm	0.36	1.84	0.04	0.91	
20-63 µm	0.23	4.43	0.22	2.27	
MV1014-01-17JC 60-62 cm					
>63 µm	0.25	2.31	0.06	1.19	36
20-63 µm	0.18	5.86	0.17	3.16	24

Grain Size	Ave. % Difference ^{230}Th	Ave. % Difference ^{232}Th	Ave. % Difference ^{238}U	Ave. Grain Size % Difference
>63 µm	18	14	20	22
20-63 µm	24	24	17	29

Table 2-3
Available Holocene and LGM time slice sample replicates and average percent difference of Th and U isotopes in the > 63 µm and 20-63 µm fractions of sediments from the Cocos and Carnegie Ridge sites.

Reproducibility of Grain Size Separations

To ensure that the grain size separation methodology was accurate, we compared the sum of the grain size fractions by weight with the original dry bulk weight for each sample. At Cocos Ridge thin and thick Holocene/LGM time slices, total sediment recovery ranged from 81-100% (see % sample return in Table 2-4). At Carnegie Ridge thin and thick Holocene/LGM time slices, total sediment recovery ranged from 80-99% (Table 2-4). It is possible that the cause of the lower recovery yields for the "thick sites," 8JC (Holocene, LGM) and 17JC (Holocene), was due to the greater amounts of very fine grained particles which may have been lost during the washing procedure. We also compared the recovery yields for the bulk ^{230}Th and grain size separated ^{230}Th analyses. Roughly 93 to 98% of the total ^{230}Th can be accounted for by summing up the ^{230}Th in each grain size fraction at both Cocos and Carnegie Ridge thin and thick sites (Table 2-4). Only in Holocene sample of 17JC was the ^{230}Th recovery less than this (i.e., 82%) (Table 2-4).

Time Stage	Core ID	Bulk ^{230}Th (dpm g^{-1})	Grain Analysis ^{230}Th (dpm g^{-1})	Mass Balance Yield ^{230}Th	Sample Return %
Holocene					
	MV1014-01 04JC	3.56	3.56	100	100
	MV1014-01 08JC	5.65	5.51	97.4	81.5
	MV1014-02 11JC	3.52	3.84	91.3	96.3
	MV1014-02 17JC	5.09	4.26	82.2	80.7
LGM					
	MV1014-01 04JC	2.42	2.37	97.9	93.4
	MV1014-01 08JC	5.62	5.29	93.9	81.1
	MV1014-02 11JC	2.52	2.31	91.5	99.6
	MV1014-02 17JC	5.48	5.28	96.3	95.3

Table 2-4
Mass balance of ^{230}Th in all grain sizes compared to bulk ^{230}Th analyses.

Results

Grain Size Distributions

For the thin sites (4JC—Cocos, 11JC—Carnegie), the coarse >63 μm fraction dominates, and makes up between 40 and 70 weight % of the bulk sediment (Table 2-6). Thick sites (8JC—Cocos, 17JC—Carnegie) are dominated by the <20 μm fraction, which ranges between 60 and 76 wt-% of the bulk sediment (Table 2-6). The fine fraction is approximately equally split between the <4 μm and the 4-20 μm fractions.

Distribution of ^{230}Th in Various Grain Sizes

At thick Carnegie and Cocos Ridge sites (17JC, 8JC, respectively), the <20 μm fine fraction accounts for 74-87% of the xs^{230}Th in the bulk sediment (Figure 2-2C, Figure 2-3C; Table 2-6). At thin Carnegie and Cocos Ridge sites (11JC, 4JC, respectively), the <20 μm fine fraction accounts for 25-40% of bulk sediment xs^{230}Th. The inventories of ^{230}Th seem to, in general, be controlled by the masses of the various grain size fractions. For example, sediments retrieved from glacial intervals at both thin sites contain 50-60% of their xs^{230}Th in the >63 μm size fraction (Table 2-6). The high concentration of xs^{230}Th in the >63 μm is most likely explained by the dominance of the >63 μm size fraction (68-70 wt% of total sample) in these samples (Figure 2-2A, Figure 2-3A).Thomson et al. (1993) analyzed ^{230}Th in four grain size fractions (>400 μm, 400-20 μm, 20-5 μm, <5 μm) from Atlantic Ocean sediments retrieved from sites ranging in depth from 2300 to 4500 m. Their analysis showed a threefold increase in xs^{230}Th with decreasing grain size.

In the Panama Basin, our thorium grain size results (Table 2-6) are similar to those observed in Thomson et al. (1993), McGee et al. (2010), and Kretschmer et al. (2010). At both Carnegie and Cocos thin and thick sites, we see on average a threefold increase in the specific activity of $xs^{230}Th$ with decreasing grain size from >63 μm to <4 μm. We see this pattern throughout the basin not only during the Holocene, but during the LGM as well (Figure 2-2E, Figure 2-3E). Only for the <4 μm fraction for sediment at the thick Carnegie site during the LGM is the $xs^{230}Th$ concentration lower than that in the 4 – 20μm size fraction (Figure 2-3E), and this is likely because of the significant authigenic U concentration in the finest fraction (see below).

Figure 2-2
Side-by-side comparison of Cocos Ridge grain size data for Holocene and LGM time slices of thin site (4JC; light red and light blue) and thick site (8JC; dark red and dark blue). The light red hashed bars for Holocene sample 4JC are estimates and likely represent the distribution of the <4 μm and 4-20 μm size fraction due to loss of those fraction during separation and analysis. **A)** Weight % of each grain size fraction. **B)** Total activity (dpm g^{-1}) of ^{232}Th in each grain size fraction. Holocene thin site (4JC) <20-μm fraction was calculated assuming 100% sample recovery of the fine fraction. **C)** $xs^{230}Th$ % in each grain size fraction. **D)** Authigenic U % in each grain size fraction. **E)** Measured activity (dpm g^{-1}) of $xs^{230}Th$ which has been corrected for detrital and authigenic fractions. **F)** Measured activity (dpm g^{-1}) of authigenic U in each grain size fraction.

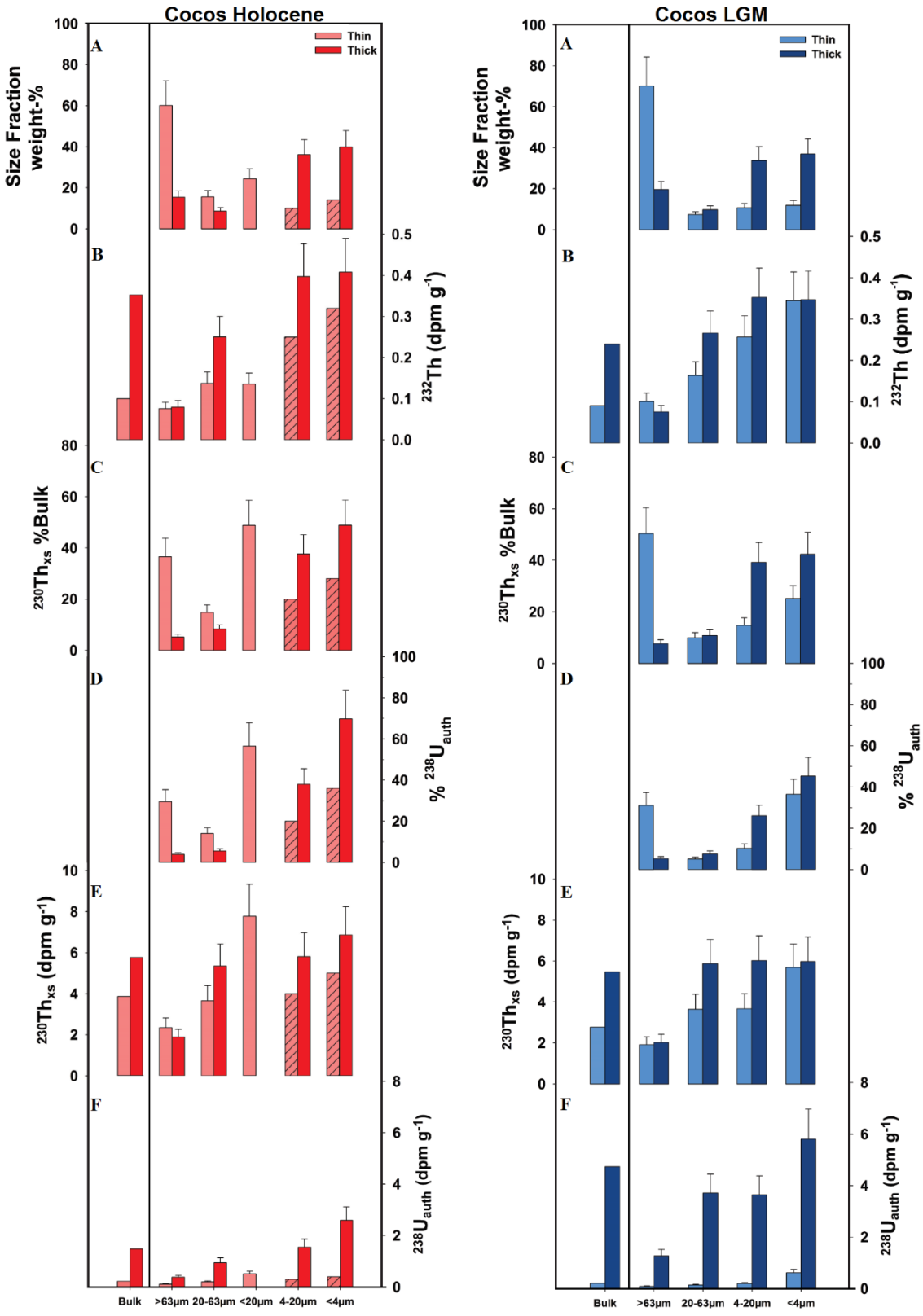
Cocos Holocene
Cocos LGM
Thin
Thick
A
B
C
D
E
F
Size Fraction weight-%
^{232}Th (dpm g^{-1})
^{230}Th$_{xs}$ %Bulk
% ^{238}U$_{auth}$
^{230}Th$_{xs}$ (dpm g^{-1})
^{238}U$_{auth}$ (dpm g^{-1})
Bulk
>63µm
20-63µm
<20µm
4-20µm
<4µm

Time Stage	Core ID	Bulk U_{auth} (dpm g^{-1})	Bulk $xs^{230}Th$ (dpm g^{-1})	Size Fraction	Size Fraction wt%	^{230}Th (dpm g^{-1})	^{232}Th (dpm g^{-1})	$xs^{230}Th$ (dpm g^{-1})	$xs^{230}Th_{(o)}$ (dpm g^{-1})	Bulk % $xs^{230}Th$	^{238}U (dpm g^{-1})	U_{auth} (dpm g^{-1})	$\%U_{auth}$	% Bulk U_{auth}
Holocene	**MV1014-01 04JC**	0.22	3.46	>63 µm	60	2.17	0.08	2.10	2.35	37	0.16	0.11	67	29
	13-15 cm			20-63 µm	16	3.39	0.14	3.27	3.66	15	0.29	0.20	67	14
				<20 µm	24	7.11	0.14	6.95	7.78	49	0.61	0.51	84	57
	MV1014-01 8JC	1.48	5.26	>63 µm	15	1.82	0.08	1.72	1.89	5	0.44	0.38	87	4
	30-32 cm			20-63 µm	9	5.15	0.25	4.88	5.35	8	1.12	0.94	84	5
				4-20 µm	36	5.73	0.40	5.30	5.81	38	1.83	1.55	85	38
				<4 µm	40	6.80	0.41	6.26	6.86	49	2.88	2.59	90	70
	MV1014-02 11JC	1.99	3.19	>63 µm	39	1.55	0.05	1.43	1.60	16	0.74	0.71	96	14
	30-32 cm			20-63 µm	11	3.19	0.21	2.86	3.20	9	1.66	1.51	91	9
				4-20 µm	27	5.16	0.23	4.68	5.23	36	2.84	2.68	94	36
				<4 µm	23	6.58	0.18	5.78	6.46	38	5.71	5.58	98	63
	MV1014-02 17JC	3.25	4.68	>63 µm	28	1.88	0.04	1.72	1.88	13	1.39	1.36	98	12
	120-122 cm			20-63 µm	12	3.76	0.11	3.37	3.68	10	3.19	3.11	97	11
				4-20 µm	29	4.55	0.15	4.02	4.40	31	4.28	4.17	98	37
				<4 µm	31	6.32	0.17	5.44	5.94	45	7.78	7.66	98	73
LGM	**MV1014-01 04JC**	0.2	2.32	>63 µm	70	1.68	0.10	1.60	1.91	50	0.16	0.09	56	31
	19-21 cm			20-63 µm	7	3.18	0.16	3.04	3.64	10	0.25	0.14	55	5
				4-20 µm	11	3.28	0.26	3.07	3.67	15	0.37	0.19	52	10
				<4 µm	12	5.11	0.34	4.75	5.69	25	0.86	0.62	72	36
	MV1014-01 8JC	4.73	4.46	>63 µm	20	1.97	0.08	1.65	2.02	8	1.32	1.27	96	5
	90-92 cm			20-63 µm	10	5.76	0.27	4.79	5.87	11	3.89	3.70	95	8
				4-20 µm	34	5.93	0.35	4.92	6.03	39	3.89	3.64	94	26
				<4 µm	37	6.34	0.35	4.88	5.98	42	6.05	5.81	96	45
	MV1014-02 11JC	3.32	1.78	>63 µm	68	2.03	0.06	1.57	1.92	60	2.00	1.96	98	40
	70-72 cm			20-63 µm	10	3.56	0.14	2.63	3.21	14	4.08	3.98	98	12
				4-20 µm	13	3.75	0.17	2.58	3.15	19	5.13	5.01	98	20
				<4 µm	9	4.14	0.17	1.21	1.48	6	13.50	13.38	99	37
	MV1014-02 17JC	8.16	3.77	>63 µm	23	2.37	0.06	1.92	2.31	12	2.22	2.18	98	6
	280-282 cm			20-63 µm	14	4.67	0.13	3.79	4.58	14	4.23	4.14	98	7
				4-20 µm	38	6.20	0.24	4.73	5.71	48	7.03	6.86	98	32
				<4 µm	26	6.84	0.19	3.76	4.54	26	15.60	15.46	**99**	**48**

Table 2-5
Uranium and thorium activities in various grain size fractions of Panama Basin sediment samples.

Distribution of Authigenic U in Various Grain Sizes

At the Cocos Ridge thin and thick sites, minor amounts of detrital ^{238}U are found in our samples. The majority of the U found at both thin and thick Cocos sites is authigenic (Figure 2-2D, Table 2-6). Thin and thick authigenic U ranges between 52-96% in each size fraction during the Holocene and 67-90% during the LGM. At both thin and thick sites during the Holocene and LGM, the finest fraction contains the majority (36-70%) of the total authigenic U found in the samples (Figure 2-2D).

At the Carnegie Ridge thin and thick sites, the detrital ^{238}U signal is nearly nonexistent. The majority of the U found at both thin and thick Holocene and LGM samples is authigenic (91-99%). The majority of authigenic U resides in the finest fraction, ranging between 37-73% of the bulk sample (Figure 2-3D). However, during the LGM, the activity of authigenic U in the <4 μm size fraction is roughly 2-2.5 times greater than that during the Holocene at both thin and thick sites, and adds significant ingrown $xs^{230}Th$ to the sediment sample (see $xs^{230}Th$ results above).

At both thin/thick Carnegie and Cocos sites, authigenic U is 1.5-3 times greater in the LGM than that in the Holocene (Figure 2-2F and Figure 2-3F) when excluding the thin Cocos site, which has virtually no authigenic U likely due to the large degree of sediment winnowing at 4JC. Authigenic U concentrations are highest in the finest fraction (<4 μm) of the glacial samples from both the thin (11JC) and thick (17JC) sites at the Carnegie Ridge (13.4 dpm g^{-1} and 15.5 dpm g^{-1}, respectively; Figure 2-3F; Table 2-6). One likely explanation for the anonymously anomalously high authigenic U found throughout the Panama Basin is focusing of fine-grained organic rich material.

Figure 2-3
Side-by-side comparison of Carnegie Ridge grain size data for Holocene and LGM time slices of thin site (11JC; light red and light blue) and thick site (17JC; dark red and dark blue). **A)** Weight-% of each grain size fraction. **B)** Total activity (dpm g^{-1}) of ^{232}Th in each grain size fraction. **C)** $xs^{230}Th$ % in each grain size fraction. **D)** Authigenic U % in each various size fraction. **E)** Measured activity (dpm g^{-1}) of $xs^{230}Th$ which has been corrected for detrital and authigenic fractions **F)** Measured activity (dpm g^{-1}) of authigenic U in each grain size fraction.

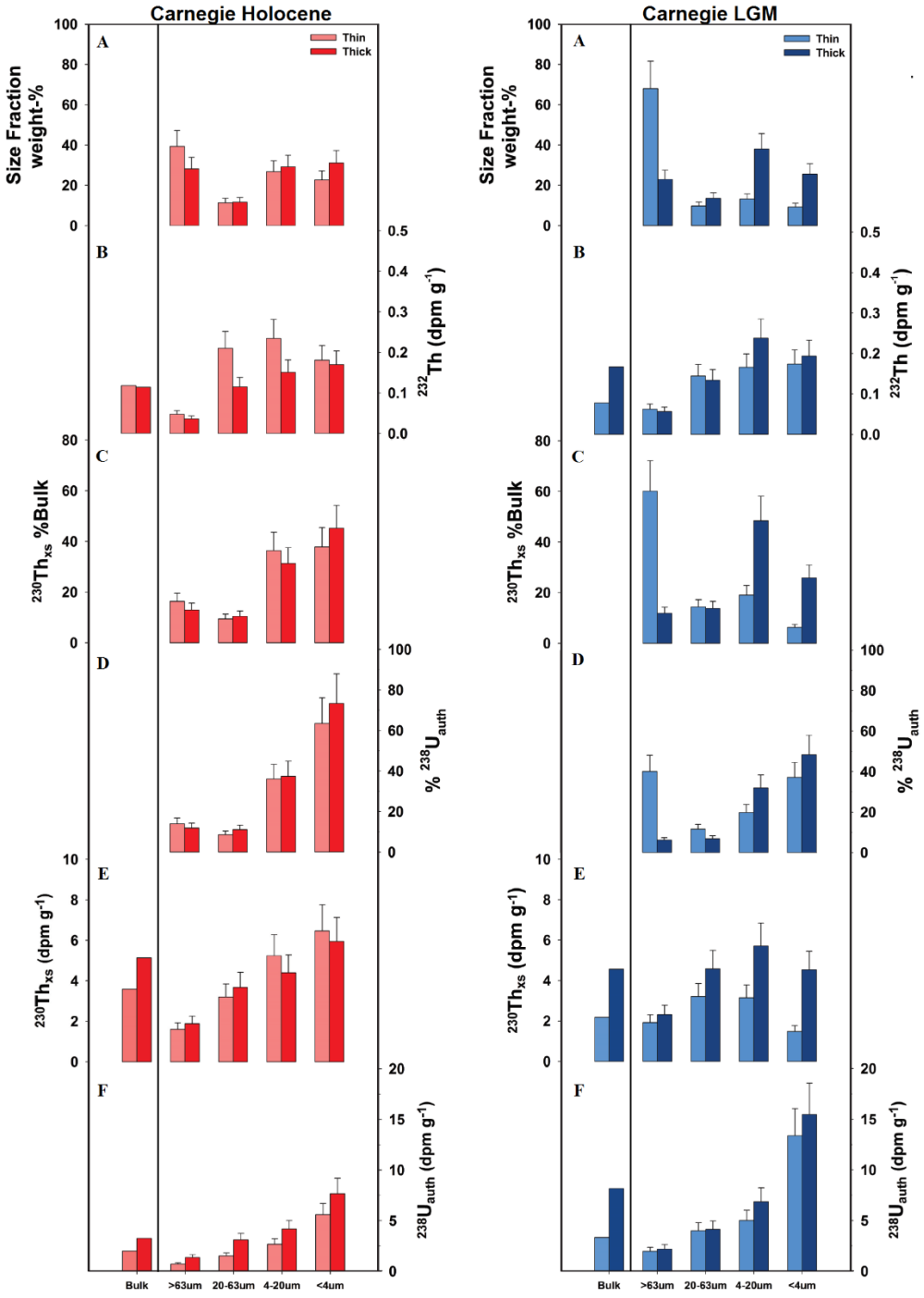
Carnegie Holocene
Carnegie LGM
Thin
Thick
Size Fraction weight-%
A
B
C
D
E
F
^{232}Th (dpm g^{-1})
^{230}Th$_{xs}$ %Bulk
% ^{238}U$_{auth}$
^{230}Th$_{xs}$ (dpm g^{-1})
^{238}U$_{auth}$ (dpm g^{-1})
Bulk
>63um
20-63um
4-20um
<4um

Discussion

Sediment Focusing Factors

In the most recent study of sediment focusing in the Panama Basin, Marcantonio et al. (2014) examined four multicores of late Holocene age from the Cocos and Carnegie Ridges. By investigating paired piston cores (Cocos, 4JC and 8JC; Carnegie, 11JC and 17JC) from the same sites, we expand upon the study conducted by Marcantonio et al. (2014) by comparing early Holocene and LGM time slices at the same seismically-identified thin and thick sites in the Panama Basin. First, we discuss the bulk thorium data, including an analysis of the ^{230}Th-derived sediment focusing factors.

At both Cocos and Carnegie Ridge paired thin and thick sites, ^{230}Th-derived focusing factors (Ψ) for sediment deposited during the Holocene (Table 2-5) are nearly identical to those factors determined for the paired multicores in Marcantonio et al. (2014). Specifically, during the Holocene at the Cocos Ridge, thin site piston core 4JC has a Ψ of 0.4 (Table 2-5), while its paired multicore 1MC has a Ψ of 0.3 (Marcantonio et al., 2014). The thick site piston core 8JC has a Ψ of 2.3 (Table 2-5), while its paired multicore 7MC has a Ψ of 2.0 (Marcantonio et al., 2014). During the Holocene at the Carnegie Ridge, thin site piston core 11JC has a Ψ of 1.6 (Table 2-5), while its paired multicore 9MC has a Ψ of 1.5 (Marcantonio et al., 2014). The thick site piston core 17JC has a Ψ of 4.0 (Table 2-5), while its paired multicore 16MC has a Ψ of 4.0 (Marcantonio et al., 2014). The near identical values suggest the ^{230}Th technique for calculating sediment focusing factors is reproducible, and that these factors have not

changed significantly throughout the entire Holocene (i.e., from early to late Holocene). Furthermore, this sediment focusing analysis corroborates the idea that ^{230}Th-derived focusing factors are reliable indicators of sediment redistribution, which has been identified by seismically-determined thin versus thick sediment piles.

We add to the study conducted by Marcantonio et al. (2014) by examining sediment focusing factors determined for the thin and thick sites sampled at the Cocos and Carnegie Ridges during the LGM. At the Cocos Ridge, both thin and thick sites display nearly a 2-fold change in sediment focusing factors (Table 2-5) from the Holocene to LGM. The thin site (4JC) experienced enhanced winnowing (Ψ= 0.2) during the LGM as well as lower sedimentation rates, while the thick site (8JC) during the LGM had focusing (Ψ= 4.1) and an increase of sedimentation rates from 4.5 cm kyr^{-1} in the Holocene to 7.5 cm kyr^{-1} for the LGM. During the LGM at the Carnegie Ridge, thin and thick sites demonstrate similar sediment focusing factor relationships as those determined for sediments of the Cocos Ridge. Although the thin site (11JC) did not show evidence for winnowing during the Holocene (Ψ= 1.6), there is evidence for enhanced winnowing (Ψ= 0.8) for sediment deposited during the LGM. Congruently, there was a subsequent increase in the sediment focusing factor at the thick site (17JC) during the LGM, even though the increase was not as large as that determined for the Cocos Ridge thick site. Overall, the difference between thick and thin sites is not unexpected given that the thin sites sit closer to ridge crests where the effects of sediment winnowing are greater, due to high tidal activity transporting finer grained sediment to the basin where sediments will accumulate at the thick sites. The greater

divergence in the bulk ^{230}Th-derived focusing factors during the LGM between the paired sites at both the Cocos and the Carnegie Ridges suggests more pronounced sediment redistribution from the ridges during this time.

Time Stage	ρ	% >63 µm	Ave. Age Model-derived MAR	Sample Age Model-derived >63 µm MAR	Sample ^{230}Th-derived MAR	Sample ^{232}Th MAR	Ψ
Holocene							
4JC	0.62	60	0.5	0.3	1.2	4.9	0.4
8JC	0.53	15	1.8	0.3	0.9	13.4	2.3
11JC	0.56	39	2.9	1.2	1.9	9.0	1.6
17JC	0.45	28	6.0	1.7	1.5	7.0	4.0
LGM							
4JC	0.63	70	0.4	0.3	1.7	6.1	0.2
8JC	0.45	20	2.5	0.5	1.0	9.5	4.1
11JC	0.62	68	2.3	1.6	2.9	9.4	0.8
17JC	0.45	23	6.1	1.7	1.7	11.3	5.1

Table 2-6
Cocos and Carnegie Ridge Holocene and LGM time slice age-model-derived coarse MARs (g cm^{-2} kyr^{-1}), ^{230}Th-normalized sediment MARs (g cm^{-2} kyr^{-1}), ^{230}Th-normalized-^{232}Th MARs (µg m^{-2} kyr^{-1}) and ^{230}Th-derived focusing factors.

xs^{230}Th-Derived MARs and Age-Model-Derived Coarse Fraction (>63 μm) MARs

Studying core top sediments at the same paired sites investigated here showed that there was little difference between ^{230}Th-derived MARs calculated for the Carnegie and Cocos sites (Marcantonio et al., 2014). This was an unexpected result given the higher productivity at the equatorial Carnegie Ridge site compared to that at the Cocos site. It was expected that the ^{230}Th-derived MARs (which are assumed to represent vertical rain rates) would have been higher at the Carnegie compared with those at the Cocos Ridge due to its position directly under the zone of higher equatorial upwelling. On the other hand, the age-model-derived coarse fraction (>63 μm) MAR at the Carnegie Ridge was 2.5 times greater than that at the Cocos Ridge site, in line with expectations that productivity is significantly higher closer to the equator.

The contrast between the ^{230}Th-derived and age-model -derived coarse fraction MARs led Marcantonio et al. (2014) to conclude that sediment redistribution processes by weak bottom currents potentially bias ^{230}Th-derived MARs. Strong bottom currents (20-25 cm s^{-1}), which have not been measured in this region, would be needed to redistribute the >63 μm fraction, so the rate at which this mostly biogenic fraction accumulates is likely proportional to the rain rate. Dissolution does not appear to have significantly affected the biogenic carbonate sediment at these sites (Hertzberg et al., 2016), which are located well above the lysocline. Marcantonio et al. (2016) suggested there was a biasing of ^{230}Th-derived MARs at sites that experienced significant sediment focusing or winnowing due to enhanced deposition or redistribution of fine particles

enriched in ^{230}Th. We address this possibility further and increase the temporal resolution of the initial study by Marcantonio et al. (2014).

At the Carnegie Ridge site, the two most important features observed are that the age-model-derived coarse fraction (>63 μm) MARs are 1) similar at both the thin (11JC) and thick (17JC) sites during the same time intervals (i.e., Holocene—45% difference and LGM—9% difference; Figure 2-4A), and 2) are slightly (~1.3 times) higher during the LGM than during the Holocene (Figure 2-4A). The similar coarse content accumulation rates (i.e., rain rates) measured at each site during the same time period are to be expected given the proximity (~54 km) of 11JC and 17JC (Figure 2-4A). More importantly, however, the vertical rain rates are not indicative of significantly greater primary production during the LGM in this region of the EEP (average of ^{230}Th rain rates from 11 and 17JC), indicating only a modest change in productivity for the time slices in this paper. The same is actually true for the age-based model as well.

Figure 2-4
Side-by-side comparison of Cocos and Carnegie Ridge sediment fluxes and focusing factors for Holocene and LGM time slices of thin sites (4JC, 11JC; light red and light blue) and thick sites (8JC, 17JC; dark red and dark blue) **A)** Age-model-derived coarse (i.e., 63 μm) sediment MARs (g cm^{-2} kyr^{-1}) **B)** Bulk sample ^{230}Th-normalized MARs (g cm^{-2} kyr^{-1}) **C)** ^{230}Th-normalized sediment MARs corrected using the grain size correction model of Kretschmer et al., (2010). The correction model uses the <20 μm size fraction to calculate the corrections on ^{230}Th-normalized MARs. The hashed gray bar for Carnegie Ridge Holocene thick site (17JC) uses the finest fraction (<4 μm) correction. **D)** ^{230}Th-normalized ^{232}Th MARs (μg cm^{-2} kyr^{-1}). **E)** Bulk sediment ^{230}Th-derived focusing factors (Ψ).

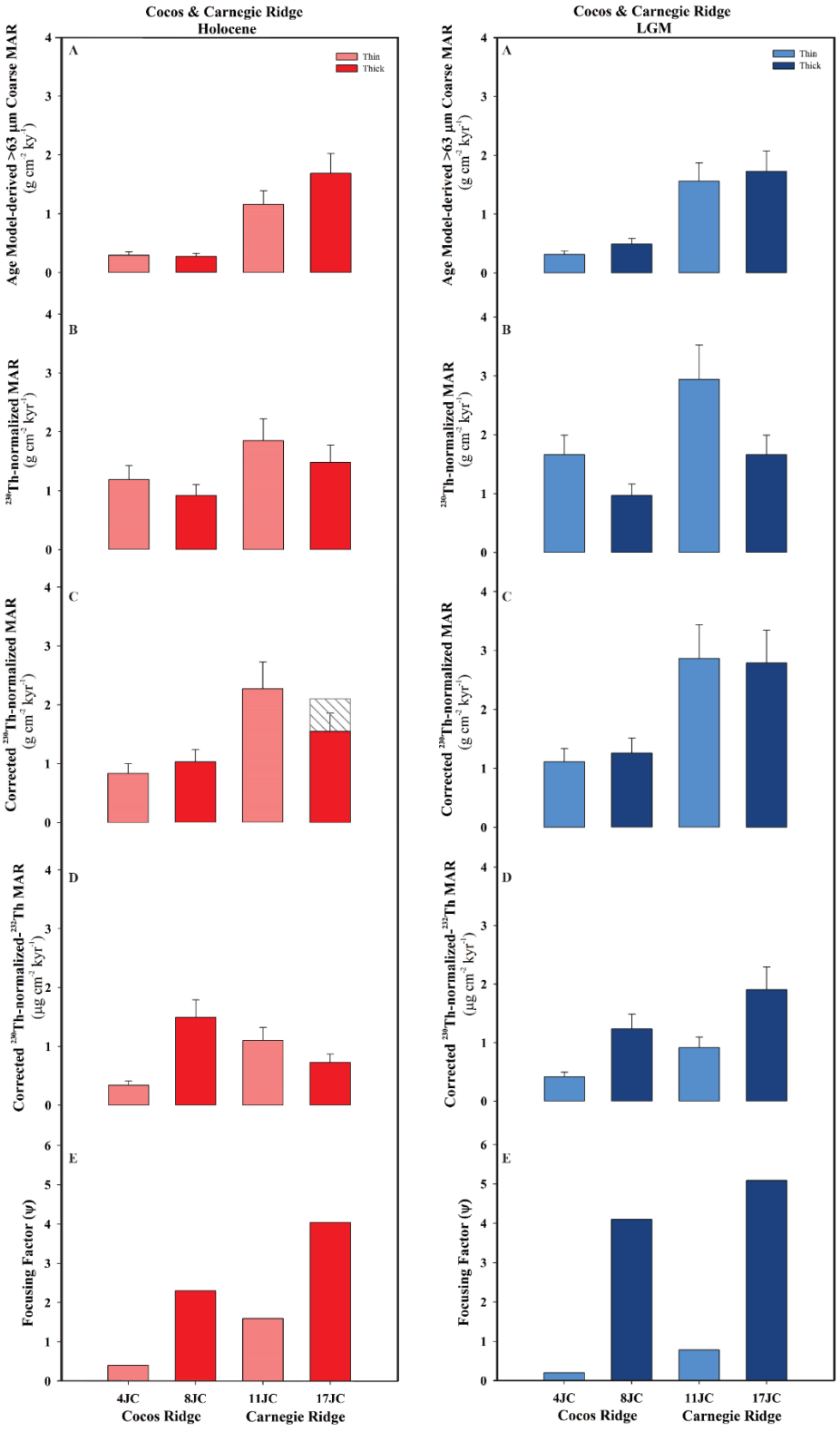
Cocos & Carnegie Ridge
Holocene
Cocos & Carnegie Ridge
LGM
Thin
Thick
A
B
C
D
E
Age Model-derived >63 µm Coarse MAR (g cm-2 ky-1)
230Th-normalized MAR (g cm-2 kyr-1)
Corrected 230Th-normalized MAR (g cm-2 kyr-1)
Corrected 230Th-normalized-232Th MAR (µg cm-2 kyr-1)
Focusing Factor (ψ)
4JC
8JC
11JC
17JC
Cocos Ridge
Carnegie Ridge

While some EEP studies based on age-model-derived MARs suggest there were greater fluxes during glacial events (Lyle et al., 2002; Paytan et al., 2004), others show minor glacial to interglacial variations in sediment fluxes (Marcantonio et al., 2001; Higgins et al., 2002; Loubere et al., 2004). Notably, the ^{230}Th-derived MARs (Figure 2-4B), which are thought to reflect vertical rain rates, have some semblance to the patterns observed in age-model-derived coarse MARs (Figure 2-4A). For example, at both 17JC and 11JC during the Holocene, similar ^{230}Th-derived MARs are observed (Table 2-5), despite a focusing factors that is 2.5 times greater at 17JC than that at 11JC. At 11JC, the average ^{230}Th-derived MAR during the LGM is ~ 1.5 times higher than that derived during the Holocene (Table 2-5, Figure 2-4B). From the Holocene to LGM, the increase in the age-model-derived coarse MAR at 11JC is similar to that in the ^{230}Th-derived MAR. At 17JC, there is little difference between the ^{230}Th-derived MARs measured during the Holocene and LGM, and the same can be said for the age-model-derived >63 μm coarse MARs (Table 2-5, Figure 2-4A). However, unlike the age-model-derived coarse MARs, the Holocene and LGM average ^{230}Th-derived MARs for 17JC are significantly lower than those measured during the same time period for 11JC. Given the proximity of the two sites, this is an unexpected result if ^{230}Th-derived MARs are representing true vertical rain rates. Apparently, the likelihood of size fractionation effects on ^{230}Th-derived MARs are most likely in regions that have undergone the greatest degree of sediment redistribution (compare Ψ between 11JC and 17JC in Figure 2-4E).

At the Cocos Ridge, the age-model-derived coarse MARs are similar at both thin (4JC) and thick (8JC) sites during the Holocene (Figure 2-4A). However, during the LGM, 8JC has coarse accumulation rates that are ~1.5 times greater than those of 4JC. At both Cocos Ridge sites, age-model-derived coarse fraction MARs are not significantly greater during the LGM compared to the Holocene. This is true for the average ^{230}Th-normalized MARs as well (Figure 2-4B). Note that these systematics hold up even though there is a 6-fold difference in focusing factor between 4JC and 8JC during the Holocene, and a 20-fold difference during the LGM. However, ^{230}Th-derived MARs are significantly greater than the age-model-derived coarse MARs at 4JC (thin site) during the Holocene (~5 times) and LGM (~4 times). One expects the ^{230}Th-derived MARs to be greater than the age-model-derived coarse fraction MARs, because they represent the bulk, rather than fractional, sediment MAR. But, the coarse fraction at 4JC makes up the bulk (60-70%) of the sediment, suggesting that the ^{230}Th-normalized MARs are being affected during extreme winnowing of the fine-grained material. At the Cocos Ridge thin site, the winnowing seems to bias our results such that the ^{230}Th MARs are being overestimated during the Holocene and LGM.

At both winnowed and focused Carnegie Ridge sites during both time periods, age model-derived >63 μm coarse MARs suggest significantly greater vertical rain rates (~5 times) than those at Cocos Ridge sites (Figure 2-4A), similar to the findings of Marcantonio et al. (2014) for the late Holocene. On the other hand, the ^{230}Th-derived MARs at the Carnegie Ridge are either similar to or slightly higher than (less than a factor of 2) than those at the Cocos Ridge. Furthermore, at both the Carnegie and Cocos

locations, the more focused sites (identified both seismically and geochemically) have ^{230}Th-derived MARs that are lower than their paired winnowed sites. We believe that the disconnect between the coarse fraction accumulation rates and the ^{230}Th-derived MARs is likely an artifact of winnowing and focusing, such that there may be an overestimation of ^{230}Th-derived MARs at winnowed sites and an underestimation at focused sites. We further investigate the effects of sediment redistribution and grain size fractionation on ^{230}Th-derived MARs below.

Effects of Grain Size on ^{230}Th Normalization Method

Due to the particle-reactive nature of ^{230}Th, fine-grained particles with greater surface area to volume ratios have higher concentrations of ^{230}Th than coarse-grained particles (Thomson et al., 1993; Kretschmer et al., 2010; McGee et al., 2010). One would expect, therefore, if there were to be a biasing of grain sizes due to sediment redistribution processes, it is likely that ^{230}Th would also be biased to some extent, with the possibility of affecting the ^{230}Th-derived MARs. Indeed, Kretschmer et al. (2010) tested the robustness of ^{230}Th-normalized sediment fluxes at focused sites in the Atlantic Ocean and created a model to make corrections based on measured ^{230}Th concentrations in fine-grained fractions of the sediment. They found that ^{230}Th-derived MARs and focusing factors were biased by sediment redistribution, but the biasing was not significant at their sites that had focusing factors that ranged from 1.8 – 5.9. Here we test the robustness of the grain size correction model in Kretschmer et al. (2010) by

investigating our Equatorial Pacific sites that have evidence for focusing *and* winnowing during the Holocene *and* LGM.

The model created by Kretschmer et al. (2010) to correct for the effects of fine-fraction redistribution on focusing factor and ^{230}Th-derived MARs makes a few key assumptions, the first of which is the assertion that both the vertical and lateral fluxes share the same ^{230}Th activity. Such an assumption maximizes the lateral flux, since the lateral flux should be preferentially finer than the vertical flux.

Furthermore, since the flux of neither the vertical or lateral component is known, the model makes the key assumption that 100% of the lateral flux is controlled by the preferential transport of the fine fraction. This simplifies the model such that the concentration of the ^{230}Th in the fine fraction is the main control of xs^{230}Th MARs. In our study, elevated concentrations of ^{230}Th were found not only in the <4 μm size fraction, but in the 4-20 μm as well (Figures 2-2E and 2-3E). We apply the model using the entire <20 μm fine fraction ^{230}Th concentration, which is obtained by summing the proportional concentration of ^{230}Th in each fine fraction (i.e., <4 μm + 4-20 μm). We find that the model produces a 12-27% reduction of the focusing factors at Cocos thick sites during the Holocene and LGM and a 5-68% reduction at Carnegie thick sites during the Holocene and LGM (Table 2-7). During the Holocene at the focused (thick) Cocos and Carnegie sites, the focusing factor dropped from 2.3 and 4.0 to 2.1 and 3.9, respectively. During the LGM at the thick sites, focusing factors dropped from 4.1 and 5.1 to 3.2 and 3.0, respectively. In conjunction with focusing factors that are overestimated, there should be an identical magnitude in the underestimation of the

^{230}Th-derived MARs (Table 2-7). The most significant change in MARs was at the focused Carnegie Ridge site (17JC) during the LGM where MARs increased from 1.7 to 2.8 g cm^{-2} kyr^{-1}. Only in this one case, for which the focusing factor was so high (5.1), was there such a significant biasing of ^{230}Th-derived MARs. Even with focusing factors as high as 4.1 did the correction amount to no more than 21%, which agrees with the general conclusion of Kretschmer et al. (2010). The boundary at which sediment focusing can play a significant role in biasing ^{230}Th-derived MARs, at least in this study, lies somewhere between focusing factors of 4.1 to 5.1.

We can also compare ^{230}Th-derived focusing factors at the Cocos Ridge to those derived from estimating average sediment deposition within the locality by seismic reflection surveys (Liao and Lyle, 2014). They compare favorably to average focusing factors estimated from the distribution of sediments since the Pliocene. Liao and Lyle (2014) estimated that the average deposition from the crest of the Cocos Ridge to the seamounts bounding the base of the ridge to be about 1 g cm^{-2} kyr^{-1}. The sediment has been redistributed from the crest of Cocos Ridge around the thin site (4JC) to sediment basins where the thick site (8JC) was cored. The Holocene MAR versus the site average 'seismic' mass accumulation rate gives an expected focusing factor of 1.8 for the thick Cocos Site, and 0.5 for the thin one, as compared to the corrected focusing factors of 2.1 for the thick site and 0.6 for the thin one.

For the first time, we have been able to observe and document the grain size effect on ^{230}Th systematics in cases where redistribution processes have preferentially removed the fine-grained sediments (i.e., winnowing). In general, we find on average a

30% correction (increase) in focusing factors at both Cocos and Carnegie thin sites during both the Holocene and LGM (Table 2-7). After applying the Kretschmer et al. (2010) correction at the Cocos thin site, 4JC, we see an increase in focusing factor from 0.4 to 0.6 during the Holocene, and from 0.2 to 0.3 during the LGM. Similarly, at the Cocos thin site, 4JC, Holocene ^{230}Th-derived MARs dropped from 1.2 to 0.8 g cm^{-2} kyr^{-1}, while the estimates dropped from 1.7 to 1.1 g cm^{-2} kyr^{-1} during the LGM. The model supports our hypothesis that at sites where fine grained sediments have been preferentially removed there is an overestimation ^{230}Th-derived MARs, with a corresponding underestimation of focusing factors, albeit relatively small.

In Figure 2-4C, we plot the corrected ^{230}Th-derived MARs. The result of the correction is clear—from the LGM to the Holocene the ^{230}Th-derived MARs have the same pattern of change as the age-model-derived accumulation rates of the >63 μm fractions for focused and winnowed sites at both the Cocos and Carnegie Ridges. Our measurements offer strong support for the model of Kretschmer et al. (2010). Understanding the grain size distribution in sediments that have been affected by deep-sea redistribution processes is a robust way, in conjunction with modeling, to deconvolve preferential sorting effects on ^{230}Th-derived MARs at sites that are both focused and winnowed spatially and temporally. The impact on ^{230}Th-MARs is such that, even in cases of significant redistribution (from winnowing factors as low as 0.2, and factors as high as 4.1) the corrections amount to less than 30%. Only in cases of extreme focusing (i.e., 5.1 at 17JC) are the corrections significant (68%). Thus, when using the ^{230}Th-normalization method as a paleoceanographic tool to provide flux

approximations in regions that have undergone significant sediment redistribution, an understanding of the grain-size distribution of the ^{230}Th contents is advised.

	(Ψ) potential corrections using different size fractions				MARs (g cm^{-2} kyr^{-1}) potential corrections using different size fractions			
MIS 1	**Uncorrected**	**<20 µm**	**4-20 µm**	**<4 µm**	**Uncorrected**	**<20 µm**	**4-20 µm**	**<4 µm**
MV1014-01 04JC	0.4	0.6	–	–	1.2	0.8	–	–
MV1014-01 08JC	2.3	2.1	2.3	1.9	0.9	1.0	0.9	1.1
MV1014-02 11JC	1.6	1.3	1.3	1.3	1.9	2.3	2.2	2.3
MV1014-02 17JC	4.0	3.9	8.1	2.8	1.5	1.5	0.7	2.1
MIS 2								
MV1014-01 04JC	0.2	0.3	0.2	0.3	1.7	1.1	1.3	1.0
MV1014-01 08JC	4.1	3.2	3.2	3.3	1.0	1.3	1.3	1.2
MV1014-02 11JC	0.8	0.8	0.8	0.7	2.9	2.9	2.7	3.2
MV1014-02 17JC	5.1	3.0	2.8	5.3	1.7	2.8	3.0	1.6

Table 2-7
Grain size corrected focusing factors (Ψ) and ^{230}Th-normalized sediment MARs using Kretschmer et al., (2010) grain size correction model. Three estimations of corrections on Ψ and ^{230}Th-normalized MARs (each correction calculated using either the <4 µm, 4-20 µm, or total fine fraction <20 µm).

^{232}Th Distribution in Various Grain Sizes and Uses as a Detrital Flux Proxy

The detrital fraction in marine sediments consists of continentally-derived material that can provide vital information needed to reconstruct paleoclimatic conditions. In the open ocean, far from the influence of continental margins (i.e. ~300 km; Singh et al. 2011), the detrital fraction consists mainly of wind-blown particles. Closer to the margin the detrital fraction consists of both wind-blown and fluvially-derived (hemipelagic) material. The accumulation rates of wind-blown dust particles in the open ocean provides crucial information about past wind circulation patterns and

how changes in these patterns relate to climate. ^{232}Th has been used as a tracer for dust flux because of its relatively constant concentration (~11 ppm; McGee et al., 2007) in continental material delivered to the ocean. In conjunction with ^{230}Th-normalized MARs, and with an understanding of how focusing has affected these estimates (here and Marcantonio et al., 2014), we can attempt to reconstruct past detrital fluxes to our paired Panama Basin sites. As hypothesized by Marcantonio et al. (2014), we find that both focusing and winnowing have had little effect on ^{230}Th-derived detrital accumulation rates, such that model corrections were minimal on the patterns of change spatially and temporally.

We compare grain size corrected ^{230}Th-normalized ^{232}Th MARs at Carnegie Ridge thin and thick paired sites, which are approximately 600 km from the continental margin. We find similar MARs (~40% difference) at the two sites during the Holocene (11JC= 1.10 μg cm^{-2} kyr^{-1}, 17JC= 0.73 μg cm^{-2} kyr^{-1}), but significantly different MARs (~70% difference) during the LGM (11JC= 0.91 μg cm^{-2} kyr^{-1}, 17JC= 1.91 μg cm^{-2} kyr^{-1}). This result is surprising because of the proximity of the sites within a basin which should receive the same detrital flux. The apparent difference in detrital flux between the two sites during the LGM is likely due to the differences in ages of the LGM time slices. As noted above, the LGM sample for 11JC is closer to the start of the deglacial than is the LGM sample for 17JC. There very well may be a difference in detrital flux at the two sites because of the slight temporal offset. Concentrating on 17JC, which has better age control, we find a ~2.6-fold higher detrital flux during the LGM compared to that in the Holocene. This is in agreement with other studies of sediments throughout

the equatorial Pacific Ocean that show ^{230}Th-derived detrital fluxes (representative of dust fluxes) during the LGM that are at least double those in the Holocene (Anderson et al., 2006; Bista, 2015; McGee et al., 2007, Winckler et al., 2008, 2016; Costa et al., 2016; Jacobel et al., 2016, 2017).

Comparing Cocos Ridge thin and thick paired sites (~350 km from the continental margin), grain size corrected ^{230}Th-normalized ^{232}Th detrital MARs are 3-4.5 times greater at the focused site (8JC) than those at the winnowed site (4JC) during both the Holocene and LGM (Table 2-5, Figure 2-4D). This result is surprising because it is expected that the total detrital flux at the Cocos Ridge sites during each time period would be similar due to the sites' proximity to each other. Also of note, is that the focused site (8JC) has a detrital flux that is ~1.5 times greater during the Holocene than at the LGM. We have two hypotheses to explain these data. First, the patterns of variability in detrital flux at the Cocos sites could be related to a pronounced fluvial (hemipelagic) component from central America, which is closer to the continental margin by 150 km than are the Carnegie sites. If this were true, then the cause of the greater detrital fluxes during the Holocene may be higher riverine discharge that supplies more detrital particles to sediments close to the continental margin. Indeed, several terrigenous records from Central America point to a wetter Holocene (Mollier-Vogel et al., 2013, Pahnke et al., 2007, Rincón-Martínez et al., 2010, Seillès et al., 2015), which could lead to greater riverine discharge, and potentially higher and more variable detrital fluxes during the Holocene at the Cocos Ridge. Alternatively, the Holocene increase in detrital flux may be representative of dust flux and relate to movement of the ITCZ. In

the Holocene, the Cocos Ridge locality is beneath the average modern ITCZ position. In contrast, there is evidence (Koutavas and Lyngch-Stieglitz 2014) that the ITCZ may have been located in a more southerly position during the LGM, which would decrease the dust rainout then.

Conclusion

In the Panama Basin, during both the Holocene and LGM at both winnowed and focused sites, the finest grain size fractions contain the majority of $xs^{230}Th$, ^{232}Th, and authigenic U. At focused sites, the bulk inventory (i.e. >70%) of $xs^{230}Th$ is found in the <20 μm size fraction. At winnowed sites, even due to the partial removal of the fine fraction, ~40% of the bulk inventory of $xs^{230}Th$ is found in the <20 μm size fraction. Detrital ^{232}Th is also mainly found in the finest fraction. Using the model constructed by Kretschmer et al. (2010), we compare grain-size-corrected ^{230}Th-derived MARs to the age-model derived MARs of the >63-μm fraction and find that the patterns of change are in agreement both spatially and temporally at our Panama Basin sites. This provides strong support for the use of a grain-size correction model (Kretshcmer et al, 2010). At sites with ^{230}Th-derived sediment focusing factors less than ~4, ^{230}Th-derived MARs are underestimated by less than ~20%, with focusing factors overestimated by the same amount. For sites that have experienced winnowing, ^{230}Th-derived MARs are overestimated by less than ~50%, with focusing factors underestimated by the same amount. A ^{230}Th-derived focusing factor of ~5 observed at one site requires a greater correction (~70%), which can significantly alter interpretations if left uncorrected.

^{230}Th-normalization remains an important paleoceanographic tool for reconstructing sediment fluxes in regions of the ocean that have undergone significant sediment focusing, provided there is an understanding of the distribution of ^{230}Th in the fine-grained size fractions.

Patterns of changing ^{230}Th-normalized detrital ^{232}Th fluxes are significantly less affected by sediment redistribution processes for sites that have focusing factors less than ~4. Detrital fluxes are dominated by hemipelagic inputs at the Cocos Ridge sites that are within ~ 350 km of the continental margin. At the Carnegie Ridge site 17JC, which is greater than 600 km of the margin, the detrital flux is dominated by the eolian component.

CHAPTER III

AUTHIGENIC URANIUM IN EASTERN EQUATORIAL PACIFIC SEDIMENTS

Introduction

Marine sediments contain trace elements that may be used as proxies to reconstruct past oceanographic processes that are influenced by global climate. Trace elements can reach the seafloor by incorporation into organisms or by being scavenged onto organic and inorganic particle surfaces. Their abundance in the water column can also be affected by redox-driven chemical reactions. At or near the sediment-water interface the removal of trace elements can occur through biologically-mediated remineralization processes as trace elements diffuse across the sediment-water interface. For example, the removal of redox sensitive metals out of solution, such as U, Cd, and Mo, has been linked to changes in surface ocean productivity (Chase et al., 2001, Pailler et al., 2002, Clavert and Pedersen 1993). In addition, after authigenic deposition, the preservation of redox-sensitive metals in the sediment pile may be modified by sediment-porewater redox reactions. Other redox sensitive elements (e.g. Re, Se, V, Mo, Mn, U) have been used to infer prevailing redox conditions of the overlying water column and sediment depositional environment (Calvert and Pedersen 1993, Graybeal and Heath 1984, Nameroff et al., 2002, Thomson et al., 1996).

Although in most major ocean basins today bottom waters are well oxygenated, sub-oxic to anoxic sedimentary environments are possible when the rate of oxygen

consumption in the sediments is surpassed by the burial of particulate organic matter. In the sediment column, the biogeochemical change from oxic to sub-oxic to anoxic by the oxidation of organic matter follows a well-defined redox ladder (Froelich et al., 1978), which follows a natural progression of oxidants available in sediment pore waters. Oxidants available are O_2, NO_3^-, MnO_2, $Fe(OH)_3$, and SO_4^{2-}. At some variable depth below the sediment-water interface, organic matter will be oxidized by the first available oxidant (Figure 3-2) that yields the largest free energy, which in most cases is O_2. After utilization of oxygen, redox potential drops to the next most efficient oxidant, NO_3^-, and so on. The physical identification of the transition from oxic to more reducing conditions is noted by the brown-green color transition in pelagic sediments (e.g., in eastern equatorial Pacific (EEP) sediments, Lyle 1983). Depending on their chemistry, trace elements follow these redox fronts in marine sediments.

Authigenic uranium enrichment in pelagic sediments may either be a function of enhanced organic carbon deposition (Anderson 1982, Anderson et al., 1998, 2002, Kumar et al., 1995, Chase et al., 2001 Francois et al., 1993, McManus et al., 2005), or changes in bottom water oxygenation level (Thomson et al., 1990, Zheng et al., 2002, Calvert and Pedersen 1993, Francois et al., 1997). Differentiating between these two scenarios is important, as the former is tied to the use of authigenic U as a paleoproductivity proxy, while the latter may be a function of changes in deep-ocean circulation. In either case, the authigenic uranium proxy may be obscured by diagenesis which may alter the original pattern of deposition. Indeed, uranium shares a redox potential similar to that for iron (Figure 3-2). Where iron is reduced from Fe(III)-Fe(II),

at or near the brown-green color transition in sediment, uranium is reduced from U(VI), as the soluble $UO_2(CO_3)_3^{4-}$ complex, to U(IV), which precipitates out of solution as the insoluble uranium oxide (Barnes and Cochran 1990). Hence, if the depth at which sediments become reoxygenated deepens to an interval within the sediments where authigenic U was enriched, uranium could be lost to the overlying water column or it may migrate vertically through the sediment until reducing conditions are met (McManus et al., 2005).

In the highly productive Panama Basin of the EEP, we attempt to understand in more detail peak authigenic U signals that are preserved in sediment deposited under varying environmental conditions. We selected in total 4 jumbo piston cores retrieved from the Panama Basin in the EEP along the ridge crest and flank of the Cocos and Carnegie Ridges (Figure 3-1). At the Carnegie Ridge, cores MV1014-02-11JC (or, simply, 11JC) and MV1014-02-17JC (or, simply, 17JC) are positioned along the equator in the EEP high productivity zone (Figure 3-1). Carnegie Ridge marine sediment cores 11JC and 17JC have been both seismically and geochemically interpreted to have undergone extremes in sediment redistribution. Sediment core 11JC has been identified as a site of potential sediment removal (i.e. winnowing) whereas 17JC is a site of enhanced sediment accumulation (i.e. focusing). At the Cocos Ridge, where productivity is lower, cores MV1014-01-04JC (or, simply, 4JC) and MV1014-01-08JC (or, simply, 8JC) were similarly chosen (i.e. winnowed (4JC) and focused (8JC) sites) (Figure 3-1). In each environment, we attempt to understand the extent to which increased authigenic U concentrations, that are likely temporally linked with climate

(and track productivity or bottom water oxygenation), are altered by early sediment diagenesis.

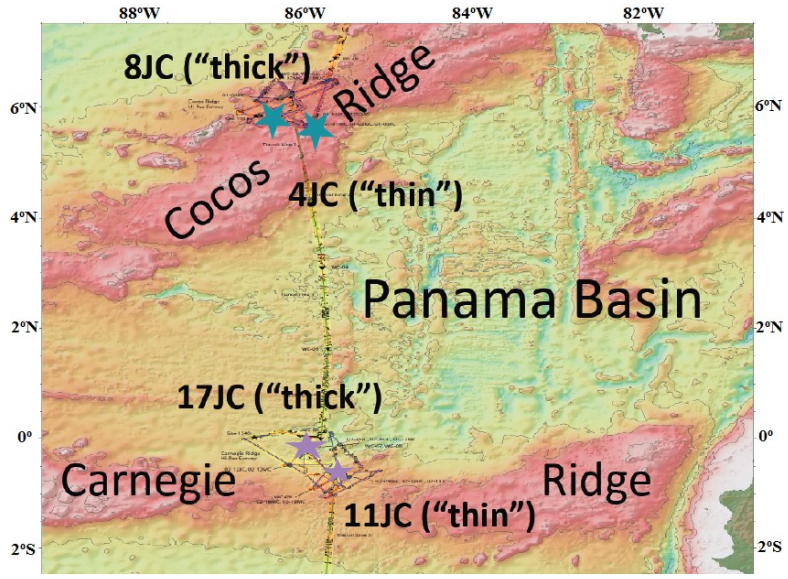

Figure 3-1
Jumbo piston sediment core locations from seismically-identified thin and thick Cocos (blue stars) and Carnegie (purple stars) Ridge sites in the Panama Basin of the EEP.

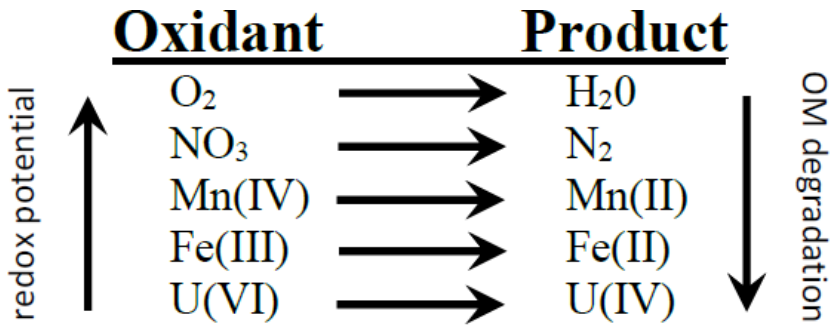

Figure 3-2
The redox ladder for the progressive oxidation of sedimentary organic matter based on Froelich et al. (1978).

Methodology

Seismic Survey

Research cruise MV1014 (R/V Melville, Oct. 2010) conducted seismic surveys along two ridges that bound the Panama Basin to identify sites of potential sediment redistribution, i.e. winnowing and focusing. To the south, the Carnegie Ridge (11JC at 0° 41.6'S 85° 20.0' W, 2452 m depth; 17JC at 0° 10.8'S 85° 52.0' W, 2846 m depth) sits at the equator in a zone of high primary productivity and upwelling (Figure 3-1). To the north, the Cocos Ridge, (4JC at 5° 44.7'N 85° 45.5' W, 1730 m depth; 8JC at 6° 14.0'N 86° 2.6' W, 1993 m depth) sits further from the equator, ~6°N, where primary productivity and upwelling is lower (Figure 3-1). Paired sites at each ridge were cored based on seismic data indicating areas of thin and pinched-out sediment drapes, i.e. winnowing, near the ridge crests, and thick sediment drapes, i.e. focusing, along the ridge flanks deeper in the basin. The retrieved winnowed "thin" cores are 4JC (Cocos) and 11JC (Carnegie), while focused "thick" cores are 8JC (Cocos) and 17JC (Carnegie). Multicores 1MC, 7MC, 9MC, and 16MC, taken at each of the "thin" and "thick" sites (Marcantonio et al., 2014), are paired with each piston core 4JC, 8JC, 11JC and 17JC, respectively. Throughout this work, we prefer the use of "thin" and "thick" to refer to the core site sediment thicknesses, rather than winnowed or focused, as they refer only to observations and not interpretations. Furthermore references to "thin versus thick sites," are short-hand notation for "core site at which there is a thinner (and potentially winnowed) sediment pile" versus "core site at which there is a thicker (and potentially focused) sediment pile."

Chronology

The age models constructed for piston cores 4JC, 8JC, 11JC, and 17JC are presented in Loveley et al. (2017) and age models for multicores 1MC, 7MC, 9MC, and 16MC are presented in Marcantonio et al. (2014). Independent age models were constructed using monospecific $\delta^{18}O$ biostratigraphy and radiocarbon age dating of the planktonic foraminifer, *Neogloboquadrina dutertrei*. For oxygen isotope analyses, *~10* N. *dutertrei* (~150 µg) were picked and analyzed in the laboratory of Dr. Jean Lynch-Stieglitz at the Georgia Institute of Technology.

Radiocarbon analyses were performed at the NOSAMS facility at the Woods Hole Oceanographic Institute. Approximately 4-6 mg of N. *dutertrei* were picked from the >250 µm size fraction for radiocarbon analysis, following the same cleaning procedures for oxygen isotope analysis. Radiocarbon ages were converted to calendar ages using Calib 7.0 (Stuiver et al., 2006) with a marine reservoir age correction of 400 years.

%$CaCO_3$

Dry bulk density of Carnegie Ridge sites, 11JC and 17JC, was estimated from % $CaCO_3$ data using the known relationship between dry bulk density (DBD) and % $CaCO_3$, where (DBD) = 1/(3.6-0.0279 x % $CaCO_3$) (Snoeckx and Rea 1994). %$CaCO_3$ was measured by CO_2 released by acidification with 10% phosphoric acid on an Automate acidification module, and subsequent measurement on a UIC 5012 coulometer. We assumed similar dry bulk densities for both thin and thick sites for

Cocos Ridge samples because of the similarity in sediment composition between both Carnegie and Cocos Ridge sites. In-house 'Midway' standard was used to check the precision and accuracy for both organic carbon and total carbon of the analyzed samples. Samples were run at Texas A&M University.

U-Th Geochemistry

Sediments spanning the past 25 kyr at both Cocos (thin and thick) and Carnegie (thin and thick) sites were analyzed for uranium and thorium isotopes. For bulk U-Th analysis, a dried, approximate 2-gram aliquot of sediment was gently homogenized using a mortar and pestle. For bulk sediment analysis, between 0.3 and 0.4 g of material was spiked with ^{229}Th and ^{236}U. Following dissolution with a mixture of $HClO_4$, HNO_3 and HF, and co-precipitation with Fe oxyhydroxides, the samples were purified for uranium and thorium by anion exchange chromatography (see Singh et al., 2011 for analytical details on uranium-thorium analyses). Uranium and thorium isotope ratios were measured on an *Element XR* magnetic sector ICP-MS at Texas A&M University.

Fe-Mn Geochemistry

For Fe and Mn analysis, approximately 50 mg of dried homogenized sediment sample was dissolved in a mixture of $HClO_4$, HNO_3 and HF. An internal 10 ppb indium standard, along with appropriate dilution standards, were used for Fe and Mn elemental analysis on an Element XR ICP-MS at Texas A&M University.

Results

Age Model Derived >63 μm Coarse MARs

At the Cocos Ridge thin and thick sites, age-model-derived >63 μm coarse MARs are ~1.5-2 times greater during MIS 2 than during the Holocene (Figure 3-3, 3-4). At the Carnegie Ridge, thin and thick sites have age-model-derived >63μm coarse MARs that are ~1.5 times greater during MIS 2 than during the Holocene (Figure 3-5, 3-6). Overall, however, age-model-derived >63 μm coarse MARs at the Carnegie Ridge are ~4-6 times greater than those at the Cocos Ridge, which is likely due to the difference in proximity to the equatorial upwelling zone. Comparatively, average ^{230}Th-normalized MARs not corrected for grain size (Table 3-1, 3-2) record a similar trend of higher sediment fluxes during MIS 2 than during the Holocene at both thin and thick Cocos and Carnegie Ridge sites, albeit with a smaller MIS 2-Holocene difference.

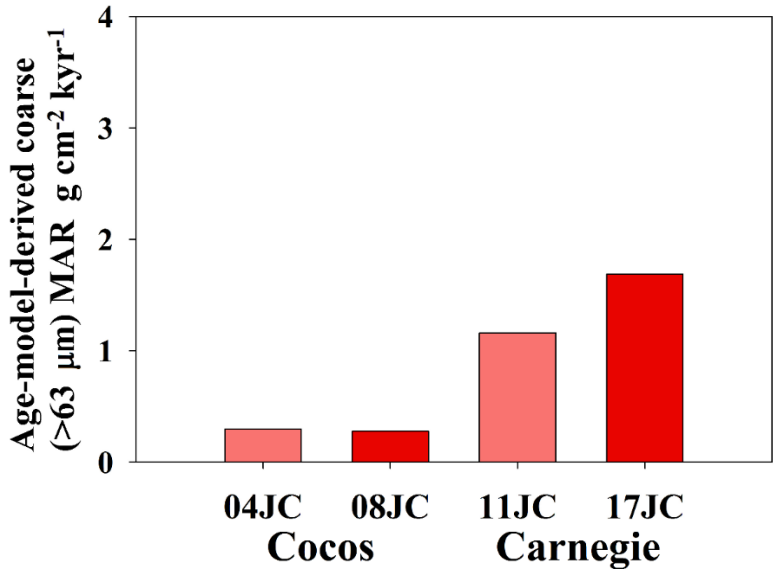

Figure 3-3
Average Holocene age-model-derived coarse-grained fraction (>63 μm) MARs at paired thin and thick Cocos Ridge (4JC; light red and 8JC; red) and Carnegie Ridge (11JC; light red and 17JC; red) sites.

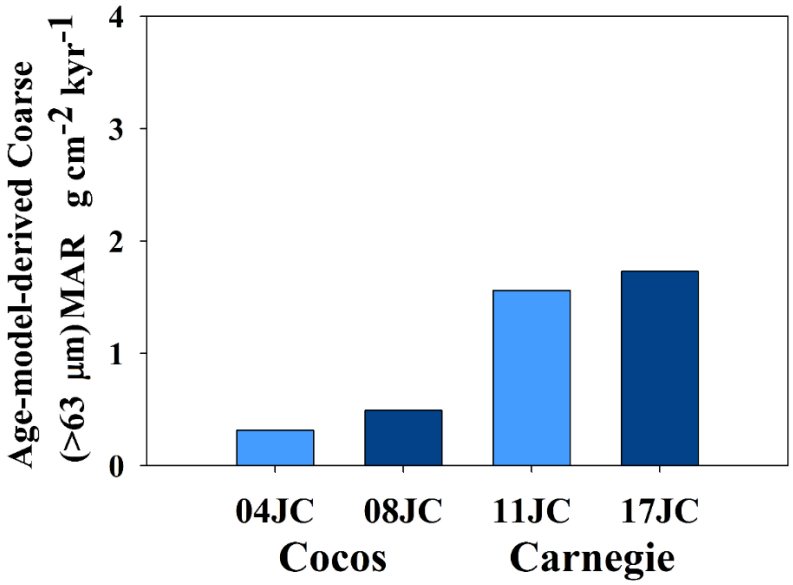

Figure 3-4
Average MIS 2 age-model-derived coarse-grained fraction (>63 μm) MARs at paired thin and thick Cocos Ridge (4JC; light blue and 8JC; dark blue) and Carnegie Ridge (11JC; light blue and 17JC; dark blue) sites.

Core ID	Age (yrs)	Depth (cm)	$\delta^{18}O$ (VPDB)	U_{auth} (ppm)	^{230}Th MAR (g cm^{-2} kyr^{-1})
4JC	8454*	11	0.24	0.26	1.05
	12225	14	0.53	0.29	1.19
	15995	17	0.68	0.27	1.37
	19766*	20	0.88	0.27	1.66
	24921	23	0.82	0.42	1.69
	30075	26	0.68	1.03	1.69
	35230	29	0.23	1.46	1.65
	40384*	32	0.44	3.22	2.12
	42381	35	0.14	2.91	2.28
	44378	38	0.30	2.51	2.41
	46375	41	0.13	2.11	2.62
	48372	44	0.44	1.25	2.07
	50368	47	0.64	1.00	2.53
	52365	50	0.45	0.97	2.82
	54362	53	0.41	1.47	2.04
	56359	56	0.51	2.18	1.67
	58356	59	0.44	2.20	1.71
	59687	61	0.38	1.92	1.80
	66344	71	0.34	1.49	2.88
	73000	81	0.44	2.33	2.27
	79656	91	0.06	2.11	2.55
	86313	101	-0.02	2.03	2.31
8JC	1132*	1	-0.11	0.35	0.85
	1504*	6	-0.46	0.34	0.76
	3217	11	-0.32	0.37	0.77
	4930	16	-0.09	0.30	0.84
	6644	21	0.12	0.27	0.88
	8357	26	-0.04	0.38	0.92
	10070*	31	0.09	1.99	0.92
	11492	36	0.48	3.23	0.93
	12913*	41	0.71	6.27	1.10
	14004	46	0.12	6.87	1.10
	15096	51	0.67	6.78	0.96
	16187	56	0.70	6.53	0.95
	17278*	61	0.96	12.16	1.02
	18141	66	0.79	9.49	0.95
	19003	71	1.08	9.70	1.00
	19866	76	0.84	8.67	0.99
	20728*	81	0.73	6.41	0.97
	21472	86	0.89	5.83	1.00
	22215	91	1.01	6.34	0.97
	22959	96	1.00	5.72	1.01
	23702*	101	1.17	6.77	0.96

Table 3-1
Cocos Ridge thin (4JC) and thick (8JC) age model, $\delta^{18}O$, and bulk sediment U concentration and ^{230}Th-derived sediment MAR

Core ID	Age (yrs)	Depth (cm)	$\delta^{18}O$ (VPDB)	U_{auth} (ppm)	^{230}Th MAR ($g\ cm^{-2}\ kyr^{-1}$)
11JC	5049	1	0.24	0.37	1.50
	6987	11	0.45	1.10	1.39
	8858	21	0.58	3.22	1.54
	10729	31	0.66	2.67	1.83
	12600	41	0.65	3.21	2.18
	14471	51	0.89	2.78	2.58
	16302	61	0.78	3.67	2.49
	18132	71	1.56	4.45	3.02
	19962	81	1.34	4.44	3.06
	21793	91	1.52	3.56	2.20

Table 3-2
Carnegie Ridge thin (11JC) age model, $\delta^{18}O$, and bulk sediment U concentration and ^{230}Th-derived sediment MAR. Thick site (17JC) data is presented in (Loveley et al., 2017)

Mn, Fe, and U

At Cocos Ridge sites, peak Mn levels occur within the first 6 cm of the core at both thin (4JC ~0.2%) and thick (8JC ~1.2%) sites (Figure 3-5 and 3-6; Table 3-3). Peak Fe levels also occur within the first 6 cm at both thin (4JC ~4%) and thick (8JC ~12%) sites (Figure 3-5 and 3-6; Table 3-3). The brown-green color transition zone at the Cocos Ridge thin site (4JC) is located at ~28 cm depth. Based on our paired multicore (1MC), it is likely that the upper 10 cm of 4JC was lost during core retrieval. At the Cocos Ridge thick site (8JC), the brown-green color transition zone is located at ~12 cm depth. At both thin and thick Cocos sites, Fe and Mn concentrations peak higher in the core than at the brown-green color transition zone. Additionally, increases in authigenic U occur deeper in both sediment cores (4 JC ~25-30 cm, 8JC ~26-36 cm). At

thin site 4JC, the increase in authigenic U is consistent with the depth of the brown-green color transition zone where U occurs in its reduced state and is, therefore, immobilized in the sediment. This is not the case at site 8JC, where other processes are likely controlling the distribution of authigenic U concentrations, which peak at depths greater than that for the brown-green transition.

Core ID	Depth (cm)	Fe %	Mn %
4JC	0.5	3.75	0.17
	1.5	3.37	0.16
	2.5	3.59	0.17
	3.5	3.73	0.19
	4.5	3.50	0.10
	5.5	3.22	5.9E-02
	12.5	0.77	4.6E-02
	17.5	0.53	7.0E-03
	22.5	0.50	4.0E-03
	27.5	0.49	4.6E-03
	30.5	0.53	3.2E-03
	32.5	0.67	6.3E-03
	37.5	0.50	5.6E-03
	42.5	0.53	8.0E-03
	47.5	0.64	7.2E-03
	70.5	0.56	4.9E-03
8JC	0.25	9.06	0.62
	0.75	9.54	0.84
	1.75	10.75	0.93
	2.25	11.69	1.29
	3.25	11.02	0.75
	4	1.36	0.30
	10	1.56	0.17
	14	1.50	0.19
	19	1.30	0.02
	24	1.77	0.02
	29	1.86	0.02
	32	1.58	0.02
	32.5	1.44	0.05
	39	1.80	0.03
	44	1.23	0.02
	49	1.77	0.03
	54	1.18	0.02
	59	1.52	0.02
	64	1.53	0.03
	68	1.17	0.02
	74	1.43	0.02
	79	1.34	0.02
	84	1.29	0.02
	89	1.37	0.02
	94	1.21	0.02
	99	1.25	0.02
	102.5	1.23	0.02

Table 3-3
Cocos Ridge thin (4JC and paired 1MC) and thick (8JC and paired 7MC) bulk sediment %Fe and %Mn.

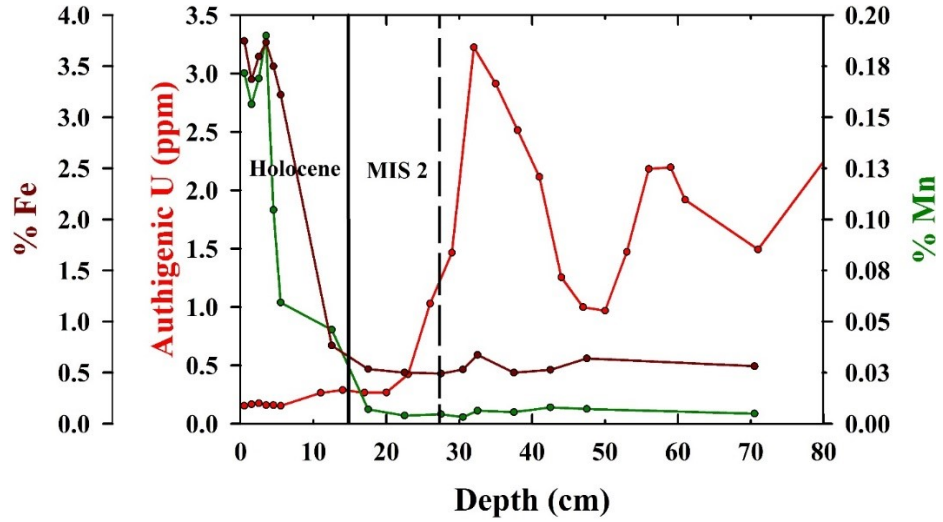

Figure 3-5
Down core profile of Fe % (dark red), Mn % (dark green), and authigenic U (red) of Cocos Ridge thin site 4JC. Authigenic U concentrations of the upper 6 cm are based on sister multicore 1MC (Marcantonio et al., 2014). The dashed line marks the physical identification of the brown-green transition zone. Solid line marks the MIS1-MIS2 boundary based on $\delta^{18}O$ stratigraphy.

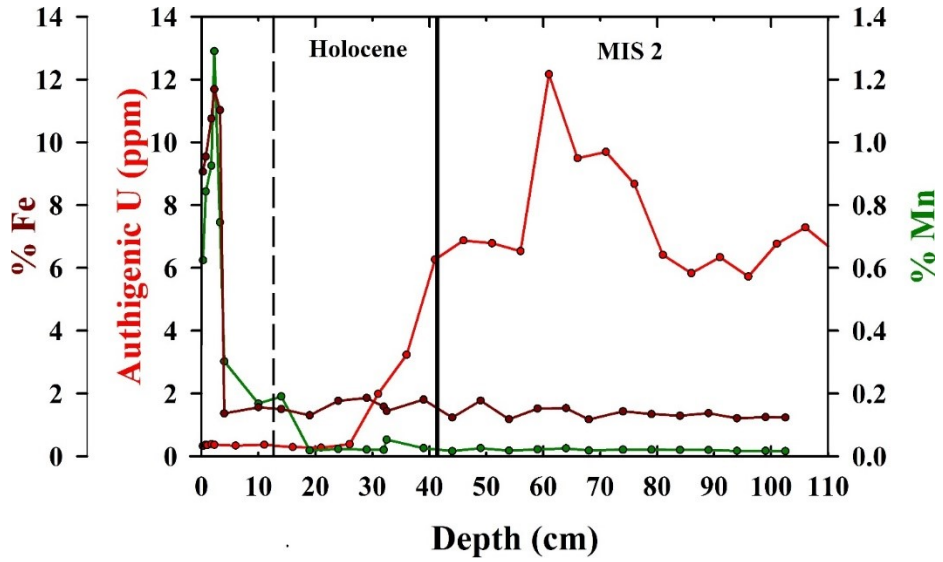

Figure 3-6
Down core profile of %Fe (dark red), %Mn (dark green), and authigenic U (red) at Cocos Ridge thick site 8JC. Authigenic U concentrations of the upper 3 cm are based on sister multicore 7MC (Marcantonio et al., 2014). The dashed line marks the physical identification of the brown-green transition zone. Solid line marks the MIS1-MIS2 boundary based on $\delta^{18}O$ stratigraphy.

At Carnegie Ridge sites, peak Mn levels occur within the first 3 cm at both thin (11JC) and thick (17JC) sites (Figure 3-7 and 3-8; Table 3-4). At thick site 17JC, peak Fe levels (4.8%) occur between 13 and 17 cm (Figure 3-7 and 3-8; Table 3-4). However, at thin site 11JC Fe levels are <1% (Figure 3-7) and show no distinct down core trend at or near the brown-green transition zone (at ~3 cm in 11JC and ~8 cm in 17JC). At thin site 11JC authigenic U remains low (<0.5 ppm) until just after the brown-green transition zone where concentrations peak (~3 ppm, 11 cm). At thick site 17JC, authigenic U remains below 1 ppm until the brown-green transition zone (Figure 3-8). However, there is no distinct peak in authigenic U concentrations, which continue to rise steadily until ~65 cm depth down core before stabilizing (Figure 3-8).

Core ID	Depth (cm)	Fe %	Mn %
11JC	0.25	0.84	0.63
	0.75	0.70	0.69
	1.25	0.99	0.84
	1.75	0.74	0.80
	2.5	0.93	1.14
	3.5	0.72	0.66
	4.5	0.91	0.44
	6	0.92	0.27
	8	0.83	0.08
	10	0.99	0.06
	12	0.92	0.05
	14	0.85	0.04
	18	0.85	0.04
17JC	0.25	0.24	1.92
	0.75	0.61	2.69
	1.25	0.65	3.66
	1.75	0.29	3.78
	2.25	0.61	4.68
	2.75	0.62	3.74
	3.25	1.12	1.72
	3.75	1.14	2.04
	4.25	1.14	2.07
	4.75	1.10	1.51
	5.5	1.16	1.77
	6.5		1.26
	8.5	1.12	1.61
	10.5	1.11	1.34
	13	1.26	0.25
	17	4.79	0.14
	21		
	23	3.68	0.15

Table 3-4
Carnegie Ridge thin (11JC and paired 9MC) and thick (17JC and paired 16MC) bulk sediment %Fe and %Mn.

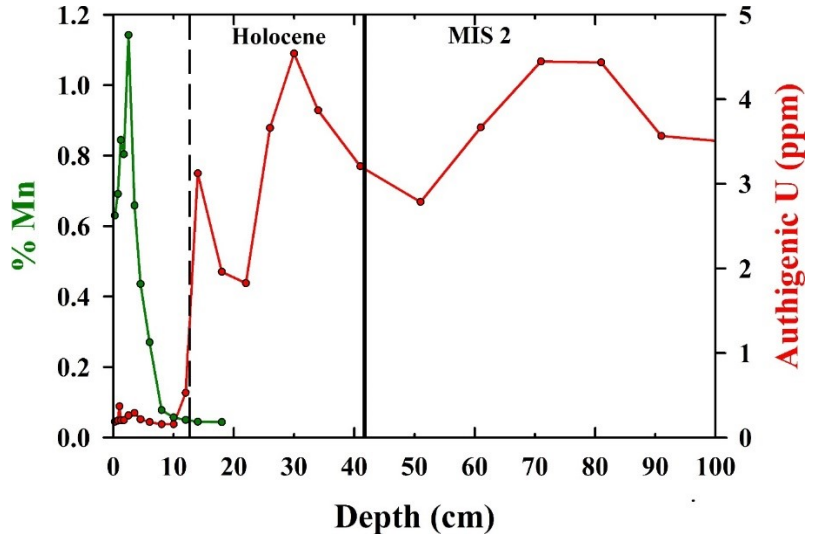

Figure 3-7
Down core profile of %Mn (dark green) and authigenic U (red) of Carnegie Ridge thin site 11JC. Authigenic U concentrations of the upper 10 cm are based on sister multicore 9MC (Marcantonio et al., 2014). The dashed line marks the physical identification of the brown-green transition zone. Solid line marks the Holocene-MIS2 boundary based on $\delta^{18}O$ stratigraphy.

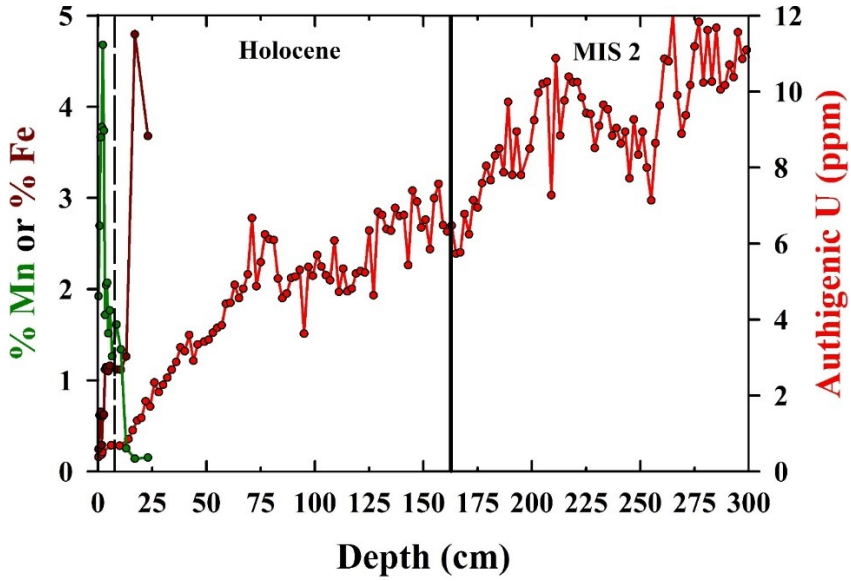

Figure 3-8
Down core profile of %Fe (dark red), %Mn (dark green), and authigenic U (red) of Carnegie Ridge thick site 17JC. Authigenic U concentrations of the upper 7 cm are based on sister multicore 16MC (Marcantonio et al., 2014). The dashed line marks the physical identification of the brown-green transition zone. Solid line marks the Holocene-MIS2 boundary based on $\delta^{18}O$ stratigraphy.

Discussion

Vertical Fluxes and Productivity Signals in the Panama Basin

The Panama Basin has been one of the most highly studied areas in the EEP given that some of the highest recorded fluxes of biologic productivity in the world occur here (Chavez and Barber 1987; Murray et al., 1994; Pennington et al., 2006; Thomas et al., 2000). Hence, reconstructing primary productivity on climate-related timescales is crucial to our understanding of carbon cycling on a global scale. Within the EEP, changes in the fluxes of barium (Dean et al., 1997; Francois et al., 1995; Marcantonio et al., 2001; Paytan et al., 1997; Loveley et al., 2017), opal (Bradtmiller et al., 2009; Dubois et al., 2010; Hays et al., 2011; Kienast et al., 2006, 2007; Marcantonio et al., 2014), calcium carbonate (Anderson et al., 2008; Loubere et al., 2004; Loubere and Richaud, 2007; Lyle et al., 2002; Mekik et al., 2012), and authigenic U (Loveley et al., 2017; Chase et al., 2001) have been used as geochemical proxies of export production in the Panama Basin.

The Panama Basin has also been well studied with respect to the degree of sediment redistribution that has occurred over the past 25 kyr. Both within and on the boundaries of the basin on the Cocos and Carnegie Ridges, significant amounts of winnowing and focusing by lateral deep-sea currents is known to have occurred (e.g., Singh et al., 2011, Marcantonio et al., 2014, Loveley et al., 2017). The ^{230}Th methodology for determining accumulation rates of sedimentary components is assumed to normalize beyond the sediment focusing process. There have been some issues with the normalization procedure of the accumulation rates of the coarse-grained (>63 μm)

fraction in regions that have been heavily winnowed or focused (Marcantonio et al., 2014). Although the issues can be corrected for (Loveley et al., 2017), we can determine changes in the pattern of vertical fluxes outside the context of the ^{230}Th methodology by simply determining age-model-derived accumulation rates of the coarse-grained fraction.

In the Panama Basin, marine sediments consist mainly of opaline silica (i.e. radiolarians and diatoms), foraminifera, and some volcanic ash (Heath et al., 1974; Kowsmann 1973; Moore et al., 1973; Van Andel 1973). Dissolution of carbonate does not play a significant role as the cores lie above the lysocline (Marcantonio el al., 2014). The coarse fraction accumulation rates should reflect changing patterns of vertical flux because even though there has been sediment redistribution by deep sea currents, the coarse fraction is unlikely affected. Although bottom currents are able to resuspend and transport the fine silt and clay, they likely lack the velocity to resuspend and transport the coarse fraction (Lyle et al., 2014; Marcantonio et al., 2014). Hence, the age-model-derived accumulation rates of the coarse-grained fraction at the paired sites at both ridges should record nearly the same values due to proximity of the paired cores to each other (Cocos Ridge cores 4JC, 8JC within 60 km; Carnegie Ridge cores 11JC, 17JC within 80 km). Indeed, this is the observation at thin and thick sites for both locations at which nearly the same vertical fluxes are recorded (Figure 3-3 and 3-4). Coarse MARs are greater at the Carnegie Ridge site than those at the Cocos Ridge site likely because the Cocos site sits at the northern extent of the high productivity zone. Furthermore, both sites record greater vertical fluxes (and, potentially, greater productivity) during MIS 2 than during the Holocene; although this difference is smaller at the Cocos site

compared to the Carnegie site. Importantly, at the same paired sites, grain size corrected Holocene and MIS 2 ^{230}Th-normalized MARs (4JC (0.8 g cm^{-2} kyr^{-1}, 1.1 g cm^{-2} kyr^{-1}), 8JC (1.0 g cm^{-2} kyr^{-1}, 1.3 g cm^{-2} kyr^{-1}); 11JC (2.3 g cm^{-2} kyr^{-1}, 2.9 g cm^{-2} kyr^{-1}) 17JC (1.5 g cm^{-2} kyr^{-1}, 2.8 g cm^{-2} kyr^{-1})), using the correction model of Kretschmer et al. (2011), record the same pattern as the age model-derived coarse accumulation rates both spatially and temporally (Loveley et al., 2017). We should point out that because sediment focusing has affected our sites, we cannot use age-model-derived bulk sediment accumulation rates as a vertical flux indicator since significant sediment has been brought in or taken away laterally at the seafloor.

We attempt to use our knowledge about the sediment accumulation rates and vertical fluxes at our Panama Basin sites, to address the behavior of authigenic U in diverse and well-characterized environments. Does the authigenic U signal reliably record the climate signal spatially and temporally? How is the signal affected by sediment diagenesis and oxidation fronts through organic matter burn down in the Panama Basin?

Mn-Fe-U Sediment Redox Profiles

The depth at which metals either remain in solution or are removed in sediment pore waters is highly variable from a few centimeters to meters down core. The depth at which reducing conditions are met is based on the rate at which organic matter consumes oxidants within the sediments (Figure 3-2). More specifically, the relationship between Mn-Fe-U and their relative emplacement within the sediment column is sensitive to

early sediment diagenesis, redox potential, and the mobility of each metal within sediment pore waters either through diffusion, advection, or irrigation through bioturbation. The depth of reduction is controlled also in part by sediment MARs and the amount of organic matter deposited spatially and temporally (e.g., Bonatti et al., 1971, Froelich et al., 1979, Wilson et al., 1985, Schulz et al., 1994, McManus et al., 2005). The preservation of the authigenic U signal within the sediment column is, therefore, dependent on the vagaries of sediment redox chemistry and potential diagenetic disturbances.

One of the most distinctive redox transition zones in pelagic sediments is the brown-green color transition zone. This zone marks the reduction zone of Fe(III)-Fe(II). This zone is seen in all of our studied cores at varying depths (Figures 3-5 to 3-8). Uranium shares a redox potential that is similar or slightly lower than that for Fe, such that in reducing sediments uranium should peak near or below the brown-green (post-oxic) color transition zone if sediment trace element profiles are driven wholly by redox fronts. At both Cocos and Carnegie Ridge thin sites (4JC and 11JC) it appears that the Mn-Fe-U profiles resemble a classic redox profile driven by the progressive consumption of oxidants through organic matter degradation (Figures 3-5 and 3-7). With the progressive oxidation of organic matter, oxygen levels within the sediment pore waters reach a minimum level where Mn remains in a solid state. Mn in both thin cores (4JC and 11JC), show clear and distinct peaks (0.19%, 4JC; 1.14%) at ~3 cm (Figures 3-5 and 3-7). The next available oxidant available for microbial degradation of organic matter after Mn is Fe as pore water oxygen levels are negligible. Of the two thin sites,

only the Cocos Ridge thin site (4JC) shows a clear profile where Fe remains high (3.5 %) until a depth of ~ 6 cm and decreases to values of about 0.5% below this. At this point in the redox ladder, there should be a distinct color change within the sediments (i.e. brown-green color transition zone), after which U likely becomes immobilized. This seems to be the case at the Cocos thin site where the brown-green transition (4JC, ~ 28 cm core depth; Figure 3-5) occurs just before the peak in authigenic U (3.2 ppm) at ~32 cm depth. Similarly, at the Carnegie Ridge thin site (11JC) authigenic U concentrations peak (~3 ppm; Figure 3-7) at about a depth of 14 cm slightly after the brown-green color transition at a depth of about 8-10 cm. In both instances, the Mn-Fe-U profiles likely represent redox-driven profiles driven by organic matter remineralization.

At the Cocos and Carnegie Ridge thick sites (8JC and 17JC), where sediment MARs and focusing factors (i.e., sediment redistribution; Loveley et al., 2017) are much higher, Mn peaks within the first 2 cm in both sediment cores at 1.3% (8JC, Figure 3-6) and 4.7% (17JC, Figure 3-8). At the Cocos Ridge thick site (8JC) Fe is high (11%) from 0 - 3 cm and drops to < 2% at depths greater than 3 cm. At the Carnegie Ridge thick site (17JC) Fe remains low (< 1%) from 0 - 13 cm and then increases to 4.8% at 17 cm. The brown-green color transition zone is located at 12 cm and 8 cm depth at the Cocos (8JC) and Carnegie (17JC) thick sites, respectively (Figure 3-6 and 3-8). At the thick Cocos Ridge site (8JC) authigenic U concentrations remain low well past the brown-green transition zone (< 0.4 ppm) until ~32 cm depth, at which point authigenic U concentrations increase to ~6 ppm (Figure 3-6). At the Carnegie Ridge thick site (17JC)

authigenic U concentrations remain low (<0.8 ppm) until 10 cm, which is slightly past the brown-green color transition zone (Figure 3-8). After that point, however, authigenic U concentrations gradually increase so that by a depth of 69 cm they reach a value of ~6 ppm. It appears that at both thick sites the upper 25 cm of the sediment core, the sediment Mn and Fe concentration profiles reflect redox-driven processes. Although the uranium concentration profiles at the thick sites have a similar pattern to those at the thin sites there are two significant differences: peak authigenic uranium concentration occur further below the brown-green transition with a gradual rise to peak contents, and peak concentrations down core are 2-3 times higher. In addition the redox transitions in 4JC appear to occur during MIS2, whereas in the other 3 cores, the transition occurs in the Holocene.

Given the potential for redox remobilization of uranium with the sediment at our four sites, we can attempt to constrain the reliability of authigenic U concentrations as a productivity proxy or bottom water oxygen proxy. By comparing the authigenic uranium profiles to the vertical fluxes, which we believe to be proxies for the likely changes in patterns of productivity at the Cocos and Carnegie Ridges, we can assess the extent of authigenic uranium mobilization. At the Cocos Ridge thin site (4JC), the Holocene/MIS 2 boundary sits at approximately 15 cm depth. Authigenic U consistently remains below 0.5 ppm until 23 cm core depth and begins to rise, then peak (3.2 ppm), at 32 cm depth. Based on the authigenic U data one could interpret the data as no change in productivity from the MIS2 to the Holocene, with substantially increased productivity during MIS3. Indeed, the brown-green transition (28 cm) happens just after peak

authigenic uranium during MIS3. If authigenic uranium were recording productivity changes there should be similar patterns at 4JC and 8JC. This is not the case. The Holocene/MIS 2 boundary at 8JC is at about 41 cm and authigenic U concentrations are highest below this depth and gradually decrease into the Holocene, until the lowest values are reached at depths lower than the brown-green transition (12 cm). Rather than responding to climate (the MIS2/Holocene boundary), the authigenic uranium signal is more likely responding to redox conditions (i.e., brown-green transition). Apparently at the Cocos Ridge, given the evidence from the two sites in close proximity, the ability of the authigenic U signal to be used as a productivity proxy has been compromised.

At the Carnegie Ridge, at both thin (11JC) and thick (17JC) sites, similar authigenic U trends are observed (i.e. authigenic U <0.5 ppm within the upper 10 cm of the core). At 11JC, the Holocene/MIS 2 boundary is located at 41 cm depth. At 17JC, the Holocene/MIS 2 boundary is located at 165 cm depth. Compared to the Cocos sites, the Carnegie sites both show authigenic uranium values that are, on average, higher during MIS2 than during the Holocene (Figures 3-7, 3-8), which is consistent with the pattern of changing vertical fluxes (Figure 3-3). And in both cases, it is only during the late Holocene in the oxic portion of the record that authigenic uranium concentrations are likely being mobilized. In this context, most of the authigenic uranium signal has been preserved, and the difference in concentrations between MIS2 and early Holocene is likely related to climate. The reason for the better preservation of a potential climate signal at the Carnegie Ridge is high sedimentation rate. At the Carnegie Ridge, average sedimentation rates at thin site 11JC are high and similar during both the Holocene (~5.3

cm kyr^{-1}) and MIS 2 (~5.4 cm kyr^{-1}). On the other hand, sediments from thick site 17JC have been deposited at significantly higher rates with average sedimentation rates during MIS2 that are nearly double (25 cm kyr^{-1}) those during the Holocene (~12 cm kyr^{-1}). Also, at both thin (11JC) and thick (17JC) sites, the brown-green color transition zone is at a much shallower depth (11JC, 14 cm; 17JC, 8 cm) within the sediment cores than the depth for the same zone in the Cocos Ridge cores. Organic matter burn down rates at the Carnegie Ridge cannot keep up with the high rates of sediment deposition so that primary authigenic uranium signals have been preserved and likely reflect changes in climate-related processes. Fundamentally, therefore, to accurately interpret the authigenic U signal, knowledge of the depth at which organic matter remineralization (i.e. organic matter burn down) becomes negligible is essential.

Modeling Organic Matter Burn Down Depths

Organic carbon burn down in pelagic sediments is a function of dry bulk density (porosity), flux of organic carbon, and sedimentation rates (Mangini et al., 2001). Modeled burn down depths (Jung et al., 1997) emphasize the sensitivity for the preservation of the authigenic U signal if it is to be used as a proxy for paleoproductivity or bottom water oxygen changes. Sediments with a lower supply of organic carbon combined with lower sedimentation rates can have burn down depths exceeding 20 cm (Mangini et al., 2001). Average bulk sedimentation rates at Carnegie Ridge thick site 17JC were much lower during the Holocene (~12 cm kyr^{-1}) than during MIS 2 (25 cm kyr^{-1}). However, there was minimal change from MIS 2 to the Holocene at thin site

11JC. We apply a model constructed by Francois et al. (1993) to look more closely at the effects of organic carbon burn down on authigenic U emplacement within the sediments at our high accumulation (i.e. highest potential for a preserved authigenic U signal) sites at the Carnegie Ridge (11JC and 17JC). We did not apply the model to our low accumulation sites at the Cocos Ridge (4JC and 8JC), as it is apparent the authigenic U signals there best match redox profiles driven by organic matter burn down.

The model employed by Francois et al. (1993) to reconstruct the depth below the sediment-water interface where authigenic U becomes immobilized (i.e. depth of authigenic U reduction) requires several variables, including: dry bulk density (ρ; estimated by % $CaCO_3$, 0.5 g cm^{-3}), sediment MARs (S; average age-model-derived MARs, cm s^{-1}), U diffusion coefficient (D; $3x10^{-6}$ cm^2 s^{-1}), and the seawater U concentration (C_i; $1.3x10^{-11}$ mol cm^{-3}). At 11JC, during the early Holocene, the modeled burn down depth (i.e. depth at which U remains immobilized in the sediments) ranges between 27-31 cm below the sediment-water interface. At this depth range, any authigenic U previously preserved above 31 cm core depth would be lost to the overlying water column by the reinvigoration (i.e. relaxation of oxygen-depleted sediment porewaters) of organic matter burn down. This result can be corroborated by our data. Authigenic U concentrations remain < 1 ppm until the current brown-green color transition zone located at 14 cm. However, there is a second authigenic uranium peak at 30 cm depth down core (Figure 3-7). During the latest Holocene, the modeled depth of authigenic U immobilization reached ~80 cm below the sediment-water interface. At this calculated depth, previously preserved authigenic U during early-

middle MIS 2 (i.e. during a time of slightly faster sedimentation and organic matter preservation) was likely deep enough to have remobilized authigenic U back into solution. It is likely organic matter began to remineralize, release authigenic U back into solution, which slowly diffused upwards through the sediment column. It is possible that at the Carnegie Ridge thin site (11JC) there is a secondary enrichment of authigenic U through the burn down of organic carbon, which overprinted the original authigenic U signal produced by either high biologic productivity or low bottom water oxygen content. Thus, we see two distinct peaks in authigenic U that match modeled burn down depths of ~30 cm and ~80 cm below the sediment water interface. If authigenic U is recording bottom water oxygen levels, it is clear that bottom waters have likely been well oxygenated at least through MIS 2 for the continued burn down and migration of authigenic U within the sediment pore waters of our thin site.

The Carnegie thick site (17JC) seems to have preserved most of its original authigenic U signal, which we have interpreted as recording primary productivity. Sedimentation rates are significantly higher during both the Holocene (~2.5 times greater) and MIS 2 (~ 4.5 times greater) at 17JC compared to those at 11JC. We again apply the model proposed by Francois et al. (1993) to estimate the depth below the sediment-water interface at which authigenic U would remain in its reduced form. The MIS 2 zone of U reduction was essentially held near the sediment-water interface (i.e. 2-3 cm below the sediment-water interface) during this time of rapid sediment accumulation. On the other hand, during the Holocene, the zone of U immobilization ranged between 10-15 cm below the sediment-water interface. It is likely, therefore, that

the authigenic U signal during the latest Holocene has been affected by organic matter burn down. Therefore of the four cores studied here, only in the case of 17JC, where sediment accumulation rates are the highest, was the original authigenic U signal preserved without significant organic carbon burn down effects. It is likely that the rapid sediment MARs (i.e. high biologic productivity) confined the authigenic U to a shallow zone of reduction throughout most of the core. Again, as at nearby thin site 11 JC, we can surmise that the overlying bottom waters were oxygenated at thick site 17JC at least through MIS 2.

It is likely that the main control on the preservation of authigenic U at our thickest site (17JC) is the supply of organic carbon and the rapid sediment accumulation is forcing suboxic conditions within sediment pore waters. Thus, we can make the assertion, at least at our Panama Basin thin and thick Cocos and Carnegie Ridge sites, authigenic U can be used as a proxy for primary productivity if specific conditions are met (i.e. remain relatively unaffected by early sediment diagenesis as indicated by the position of the brown-green color transition).

Conclusion

The use of authigenic U as a paleoceanographic tool for primary productivity or bottom water oxygen was tested at our paired thin and thick sites in the Panama Basin. The decrease in sediment MAR (and, likely, productivity) between MIS 2 and the Holocene has most likely driven the syndiagenetic enrichment of U at thin sites 4 and 11JC and thick site 8JC by the diffusion of bottom water U to slightly beyond the

oxic/post-oxic boundary as indicated by the brown-green transition zone. Modeled authigenic U sediment-water reduction boundaries lend credence to the idea that only the Carnegie Ridge thick site (17JC) has a well-preserved authigenic U profile recording changes in biologic productivity. At our thickest site, the supply of organic carbon and fast sedimentation rates were significant enough to constrain the zone of authigenic U immobilization at or near the sediment water interface. Once diagenesis can be ruled out, as it has been for the most part at site 17JC, to further elucidate the use of authigenic U as a proxy for either bottom water oxygen or primary productivity a multi-proxy approach is required.

CHAPTER IV

MILLENNIAL-SCALE IRON FERTILIZATION OF THE EASTERN EQUATORIAL PACIFIC OVER THE LAST 100 KYR

Introduction

The equatorial Pacific Ocean is one of three main high-nutrient, low-chlorophyll (HNLC) zones of the global ocean. Within these zones, utilization of macronutrients phosphate and nitrate during phytoplankton growth is likely to be limited by the micronutrient iron (Meyer, S. R., 2.007; Martin J.H. 1990). Given the equatorial Pacific's prominent role in biogeochemical cycling of carbon(Pennington et al., 2006), the variability of the iron supply to the equatorial Pacific can contribute significantly to the drawdown of atmospheric CO_2 (Ziegler et al., 2013) and, therefore, influence global climate change. Although it is well established that the supply of iron, through the dissolution of mineral aerosols (dust), to the equatorial Pacific is greater during glacial periods(Anderson et al., 2006; Winckler et al., 2008) on Milankovitch timescales, arguments both for(Murray et al., 2012) and against fertilization (Winckler et al., 2016) of the EP have been made. On millennial timescales in the eastern equatorial Pacific (EEP), changes in surface productivity seem to be consistent with the timing of North Atlantic Heinrich Stadial (HS) events or Antarctic Warm Periods, and are thought to be related to changes in nutrient delivery caused by variations in the ventilation of Southern Ocean intermediate waters (Dubois et al., 2011; Kienast et al., 2006; Kienast et al., 2013). For the first time, we show that increased delivery of dust to the EEP is coeval

with virtually all HS events (HS 1-7) during the last glacial period (MIS 2-4). Furthermore, we present evidence that there are episodes of significantly increased biological productivity during each pulse of increased dust flux, suggesting an atmospheric role for the connection between the low latitude EEP and cold North Atlantic HS events.

Methods

Analytical Methods

Radiocarbon analyses were performed at the NOSAMS facility at the Woods Hole Oceanographic Institute on the planktonic foraminifer, *N. dutertrei* (>250 μm), in samples between 0 and 500 cm in core MV1014-02-17JC. Radiocarbon ages were calibrated to calendar year using Calib 7.0 Marine13[31, 32] with a 400-yr reservoir age correction.

Stable isotopic analyses of oxygen in *N. dutertrei* specimens (>250 μm) were performed using a Thermo Electron Kiel IV automated carbonate preparation device connected to a Thermo MAT 253 stable isotope ratio monitoring mass spectrometer, equipped with a dual inlet system, housed in the Stable Isotope Geoscience Facilities (SIGF) at Texas A&M University. Isotope values are reported (Figure 4-1) in delta notation relative to the Vienna Pee Dee Belemnite (VPDB) isotopic standard. The long-term average precision of the isotopic reference material NBS19 measured within sample runs to monitor instrumental precision is 0.06‰ for $\delta^{18}O$ ($\pm 1\sigma$) for the SIGF Kiel IV and MAT 253.

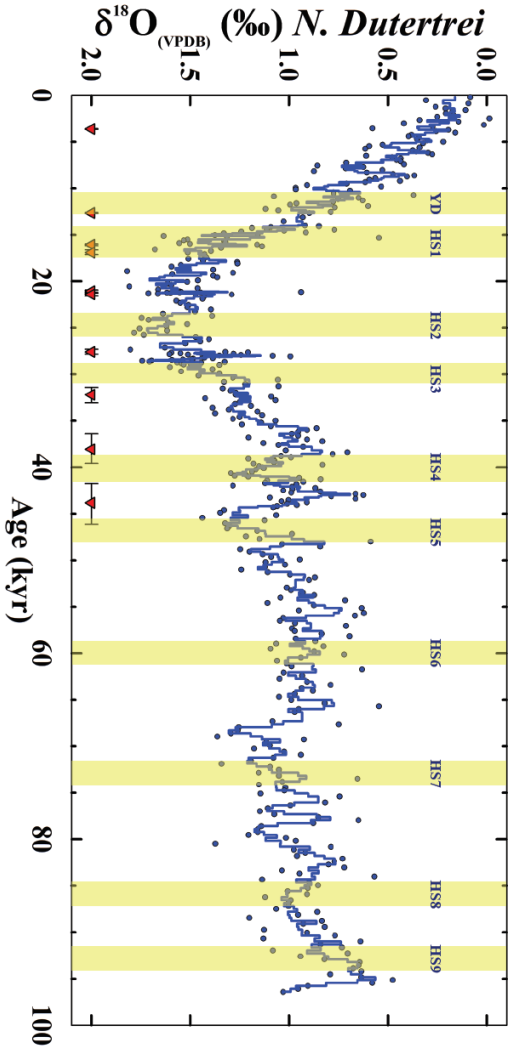

Figure 4-1
$\delta^{18}O$ record of *N. dutertrei* (filled blue dots) of marine sediment core MV1014-02-17JC with a 3-pt running mean (blue line). Solid black lines mark the interpreted boundaries between oxygen isotope stages. Yellow bars for the Younger Dryas (YD) and Heinrich Stadial (HS) Events 1 through 9 are from (Wang et al., 2001; Rasmussen et al., 2004).

Sediments for MV1014-02-17JC were sampled approximately every 2 cm and analyzed for uranium (^{234}U, ^{235}U, ^{238}U), thorium (^{230}Th, ^{232}Th) and barium (^{135}Ba, ^{137}Ba) by ICP-MS on a magnetic sector *Element XR* at Texas A&M University. Approximately

0.3-0.4 grams of sample were spiked with ^{229}Th and ^{236}U and then digested in a cocktail of HNO_3, $HClO_4$, and HF. After complete digestion, a small aliquot was removed, diluted, and spiked with ^{135}Ba separately. U-Th samples were further processed with Fe-oxyhydroxide co-precipitation and passed through anion exchange chromatography. To correct for instrumental mass bias the National Institute of Standards and Technology Uranium 500 Standard (NIST U500) was measured several times within each batch of 12 analyses of Th and U. We assumed a similar mass fractionation between uranium and thorium. For the barium analyses, we used the NIST sediment standard (NIST 2901) to ascertain our accuracy (better than 3%, on average). Average procedural blanks contributed <1% of the total measured activities for both uranium, thorium, and barium. Samples were replicated (n = 20) and reproducible within <6% for uranium and thorium isotopes and <7% for barium.

Age Models

We constructed a preliminary age model (see Figure 4-1) using 10 radiocarbon dates on *N. dutertrei* between 0-500 cm depth in core, $\delta^{18}O$ tie points at oxygen-isotope stage (MIS) boundaries (1 through 5; Figure 4-1), and the Los Chocoyos ash (84 kyr; Rose et al., 1999) at 853 cm core depth. The stage boundaries between MIS 3 and 4, and MIS 4 and 5 were the most difficult to discern, given the millennial structure in the oxygen isotope data. Ages were linearly interpolated between all radiocarbon, oxygen isotope, and the Los Chocoyos ash tie-points by assuming a constant sedimentation rate between each tie point. Our preferred age model (Figure 4-2) is identical to the first,

except that it has been refined between 35 and 70 kyr (beyond the reach of robust radiocarbon analyses and prior to the Los Chocoyos Ash) by matching maxima in the ^{230}Th-normalized-^{232}Th flux (proxy for dust flux; see below) to minima in the Hulu Cave speleothem δ^{18}O record, that are accurately dated using U-Th chronology and are thought to be representative of HS events (Wang et al., 2001) during the last glacial (i.e., MIS 2-4). There is no change in the age model between 0 to 35 or 84 to 100 kyr. Within the time period correlated between the 17JC dust and Hulu Cave oxygen records, ages were linearly interpolated between the HS 4 through HS 7 tie-points by assuming a constant sedimentation rate between each tie point.

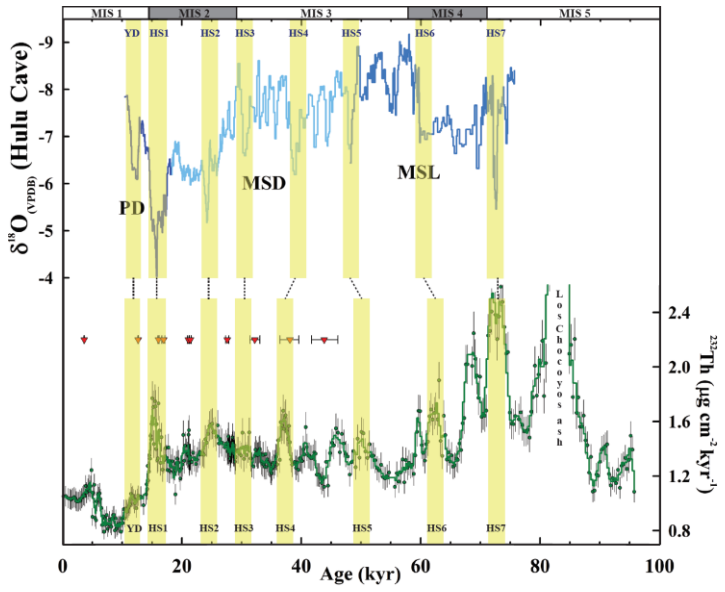

Figure 4-2
Age model tuning of MV1014-02-17JC (dark green line) of peak ^{230}Th-normalized-^{232}Th "dust" flux to peak lows in δ^{18}O from the Hulu Cave speleothem record (blue lines) between HS4-7 (dashed lines).

^{230}Th Normalization

^{230}Th is produced in the water column by the radioactive decay of dissolved ^{234}U in seawater. The ^{230}Th technique is based upon the differing geochemical behavior of dissolved ^{230}Th (particle reactive, rapidly scavenged out of seawater, oceanic residence time of decades; Bacon & Anderson 1982) compared to that of ^{234}U (well dissolved, ubiquitously distributed, oceanic residence time of 200-400 kyr; Henderson G. M. 2002). Assuming that the flux of this "excess" ^{230}Th (xs^{230}Th) reaching the seafloor is equal to its production rate in the overlying water column makes it possible to estimate sediment mass accumulation rates (MARs). Such estimations require corrections for the detrital and authigenic ^{230}Th fractions.

Detrital ^{230}Th is assumed to be in secular equilibrium with detrital ^{238}U which is estimated by the activity of the sediment sample's ^{232}Th, and assuming a detrital U/Th ratio of 0.7(Henderson & Anderson 2003). Authigenic uranium, estimated by subtracting the detrital uranium from the total uranium, is used to calculate the portion of ingrown authigenic ^{230}Th. This correction amounts to between on average 8% in the latest part of the record versus about 48% in the earliest part. Finally, since ^{230}Th is radioactive, the xs^{230}Th activity needs to be corrected for the amount of time since deposition of the sediment layer. The amount of xs^{230}Th is inversely proportional to the sediment MARs, such that MAR = β*z/[xs^{230}Th], where β is the production rate of ^{230}Th in the water column (0.0267 dpm m^{-3} yr^{-1}), z is the water column depth in m, and [xs^{230}Th] is the initial corrected xs^{230}Th in the sediment sample. Although it has been assumed that the ^{230}Th-normalization technique can differentiate between vertically

deposited and laterally advected sediment (via the calculation of ^{230}Th-derived focusing factors (Ψ); Suman & Bacon 1989), there has been some controversy over this assumption, and, specifically, the effects of grain size fractionation on the ^{230}Th methodology during sediment redistribution.

Within the Panama Basin, our previous studies (Marcantonio et al., 2014; Loveley et al., 2017) show that there is no more than a 30% biasing of ^{230}Th normalized MARs when Ψ is less than about (4; Loveley et al., 207). Average focusing factors for the interval of sediment deposited within each oxygen isotope stage (MIS 1 through 4) are consistently less than 4. Indeed, the highest average focusing factor is 3.9 for MIS 2. In addition, xs^{230}Th-normalized accumulation rates of proxies that are contained predominantly in the fine-grained fraction of the sediment (such as those proxies used here such as ^{232}Th, xsBa, and authigenic U) are not significantly sensitive to the ^{230}Th fractionation observed during sediment redistribution processes, which seems to affect coarse-grained component accumulation rates to a greater extent (Marcantonio et al., 2014; Loveley et al., 2017). This is likely due to the ^{230}Th being most heavily concentrated in the fine-grained component of the sediment (Loveley et al., 2017). Accumulation rates for proxies that are virtually entirely contained within the fine-grained component of the sediment can be approximated by multiplying the concentration of the proxy with the ^{230}Th-derived MAR.

^{232}Th Fluxes

Windblown dust supplied to ocean sediments is derived from continental material with an average ^{232}Th crustal concentration of ~11 ppm (Taylor & McLennan 1985). Even higher concentrations of ^{232}Th are found in the finer fractions of continental dust that travel long distances (<4 μm, ~14 ppm; McGee et al., 2016). Although Panama Basin sediments are subject to volcanic inputs, the ^{232}Th signal derived from the volcanic material has significantly lower ^{232}Th concentrations (~0.2 ppm; Olivarez et al., 1991; McGee et al., 2007). Hence, many researchers have used ^{232}Th as a tracer of windblown continental dust delivered to deep-ocean sediments (e.g., Winckler et al., 2008; Kienast et al., 2013; Marcantonio et al., 2014; Anderson et al., 2009; McGee et al., 2007; Jacobel et al., 2017; Costa et al., 2016; Singh et al., 2011). We have researched the ^{232}Th signal in core 17JC in great detail and have shown it to be concentrated in the finest-grain fraction (<20 um), and to be virtually entirely derived from windblown dust (Marcantonio et al., 2014; Loveley et al., 2017). Our ^{232}Th fluxes are estimated by normalizing the sediment ^{232}Th content to ^{230}Th-derived sediment MARs.

xsBa Fluxes

The accumulation of barium in marine sediments is tightly linked to organic matter export (Dymond et al., 1992; Paytan et al., 1996; Francois et al., 1995). Barite, the sedimentary phase containing the barium, is controlled by microbial recycling of organic matter as it is exported from the surface to the ocean floor. Due to the relatively insoluble nature of barite, the accumulation of biogenically-associated barium (or excess

Ba, xsBa) in marine sediments is used as an indicator of primary productivity. As a paleoceanographic tool ^{230}Th-normalized barium fluxes (xsBa) have been used extensively to reconstruct primary productivity on glacial-interglaical time scales (Winckler et al., 2005), as well as, much shorter time scales (Costa et al., 2016). The calculation of xsBa content requires the removal of the detrital (or lithogenic) barium component, which is estimated by multiplying the average upper crustal Ba/Th ratio (Taylor & Mclennan 1985) of 51.4 by the detrital Th, and then subtracting this term from the total the measured barium. Barite is contained in the sedimentary fine-grained fraction (< 5 um; Griffith & Paytan 2012) such that ^{230}Th-derived xsBa fluxes are likely not significantly biased during sediment redistribution processes (Marcantonio et al., 2014; Loveley et al., 2017).

Authigenic U Fluxes

Uranium in seawater behaves as a conservative trace element with a long residence time (~400 kyr; Henderson 2002) which makes it well mixed in the global oceans today. Uranium is supplied to the sediments by diffusion across the sediment-water interface, deposition of organic matter, and pore water redox reactions (Anderson 1982; Barnes & Cochran 1990; Colley et al., 1984; Zheng et al., 2002; Thomson et al., 1993). U(VI) exists as a highly soluble uranyl carbonate species in oxic marine sediment porewaters. However, under suboxic conditions, U(VI) is reduced to U(IV) and forms a more insoluble solid uranium oxide. The two controls on the redox state of sediment uranium are, therefore, export of organic carbon from the surface to the seafloor (which

depletes oxygen as it decomposes) and bottom water oxygen content. Given that opal and xsBa fluxes are proxies for surface productivity, and that changes in both are associated with changes in authigenic U fluxes, it can be inferred that the change in oxidation state of U is most likely due to changes in organic carbon rain rates. Our authigenic U fluxes are estimated by normalizing the sediment authigenic U component to ^{230}Th-derived sediment MARs (e.g., Kumar et al., 1995).

Study Site and Core Descriptions

Here we present new proxy data of dust (^{230}Th-derived-^{232}Th flux, see Methods) and biological productivity (excess Ba (xsBa) and authigenic U fluxes, see Methods) in a marine sediment record that covers the past four marine oxygen isotope stages (MIS 1-4, and the latest part of MIS 5) at sub-millennial resolution. Deep-sea sediment core MV1014-02-17JC (hereafter 17JC) was retrieved from slightly south of the Carnegie Ridge in the Panama Basin (00° 10.8297′ S, 85° 52.0042′ W; Figure 4-3). Low rates of carbonate dissolution at the depth of core collection (2846 m) allow for preservation of foraminiferal tests and construction of a radiocarbon-based age model (Figure 4-1). Further constraints on the age model were placed using tie-points from oxygen isotope stratigraphy (Figure 4-1), and identification of the Los Chocoyos ash (84 kyr; Rose et al., 1999) at 853 cm in the core (see Methods). The sedimentation rate at site 17JC ranges from 6 - 16 cm kyr^{-1} corresponding to an age resolution between ~100 - 300 years for our sampling resolution of 2 cm.

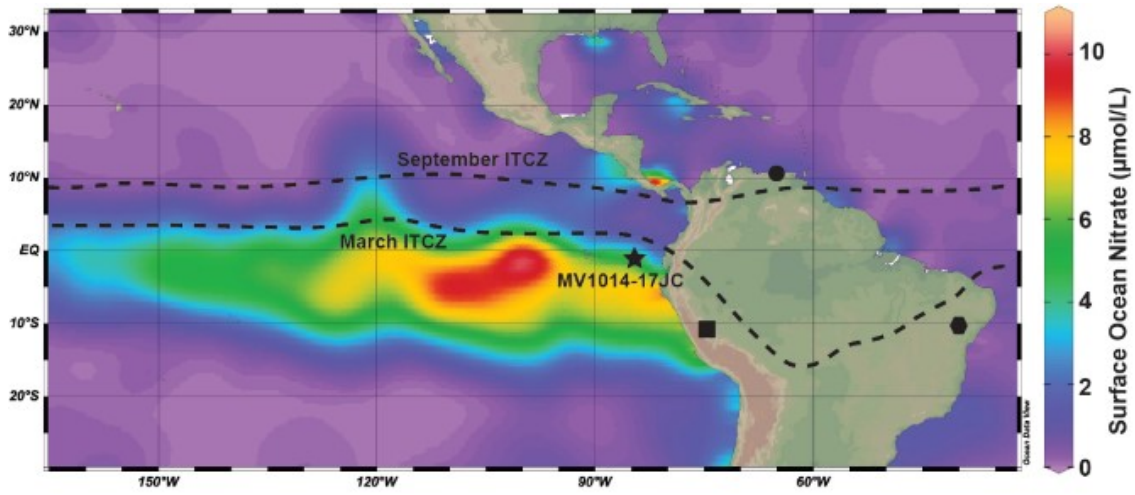

Figure 4-3
Location of the R/V Melville piston core MV1014-02-17JC (star) overlain with ocean surface nitrate concentration along with the maximum (September) and minimum (March) mean seasonal positions of the ITCZ (dashed lines). The location of South America's Peruvian (square; Kanner et al., 2012) and Brazilian (hexagon; Wang et al., 2004) speleothem records, along with the Cariaco Basin (circle; Peterson et al., 2000), are shown to provide a context for potential average global shifts of the ITCZ during HS events.

Discussion

Millennial Scale Dust Fluxes and Productivity Signals

With no tuning of the age model (other than MIS boundary tie-points), dust fluxes (^{232}Th fluxes) are highest during times consistent with the timing of HS events 1, 2, 6, 7, and 9 (Figure 4-4B). There is no discernible dust peak during HS3, but there are dust peaks, within radiocarbon age model error of two radiocarbon dated intervals, that are consistent with the timing of HS4 and HS5 (Figure 4-4B). Note that HS8 is obscured by its proximity in the record to the Los Chocoyos ash interval (Figure 4-4B). Dust fluxes during HS events are 50-100% higher than those fluxes in adjacent ambient

sediment intervals during the glacial (MIS 2-4). Assuming an average ^{232}Th concentration in dust of about 14 ppm (McGee et al., 2016), and given the average late Holocene ^{232}Th flux of about 1 μg cm^{-2} kyr^{-1}, EEP dust fluxes in the late Holocene are likely about 70 mg cm^{-2} kyr^{-1}. This value is in agreement with global dust flux models (Albani et al., 2016; Mahowald et al., 1999) which estimate modern-day dust fluxes of about 70-100 mg cm^{-2} kyr^{-1} to the EEP. Our ^{232}Th fluxes during HS events therefore correspond to dust fluxes that are roughly twice those of today, ranging from about 100 – 170 mg cm^{-2} kyr^{-1}.

Furthermore, our ^{232}Th dust fluxes are corroborated by independent measurements of bulk sediment $^{234}U/^{238}U$ activity ratios. For the first time, we use this ratio as a means to qualitatively estimate changes in the dust contribution to the total sediment uranium inventory, which is a mixture of a detrital and authigenic components. The latter component is derived from seawater, which has a uranium activity ratio of 1.146 (Henderson & Anderson 2003), while the former component (which consists of eolian detrital particles) has values of about 1 (Anderson 1982). Most of the uranium in these sediments is authigenic in origin (Marcantonio et al., 2014), so that deviations from the seawater uranium activity ratio suggests an increased eolian component being delivered to our site. The pattern of change in the $^{234}U/^{238}U$ activity ratio is anticorrelated with that of the ^{232}Th dust flux, with lows in the $^{234}U/^{238}U$ activity ratio coincident with peaks in ^{232}Th dust flux, except for HS7 which occurs at the MIS 4/5 boundary (Figure 4-4C).

Additionally, the millennial peaks in xsBa fluxes, which has been consistently used as a proxy for primary productivity, are consistent with the timing of ^{230}Th-normalized ^{232}Th dust flux peaks during or near HS 1, 2, 5, 6 and 7 (Figure 4-4D). Similarly, fluxes of authigenic uranium show peak values that are coincident with the timing of peak dust fluxes during or near HS 1, 2, 5, 6, and 7 (Figure 4-4E). It appears that authigenic uranium fluxes are 3-4 times higher during glacial MIS 2-4 than during interglacial MIS 1 and 5 (Figure 4-4E). This again suggests that primary productivity was greater during the last glacial compared to the interglacial MIS 1 and 5 which again may be driven by the overall increase of dust delivered to the EEP.

Figure 4-4
A) $\delta^{18}O$ ice core record (blue line) of North Greenland Ice Core Project (NGRIP).

B) ^{230}Th-normalized-^{232}Th flux (green-filled circles) measured as a proxy for dust flux in EEP marine sediment core MV1014-02-17JC (00° 10.8297′ S, 85° 52.0042′ W). Line joining data represents a 3-point running mean. Note that the thorium record is affected by the proximity to Los Chocoyos ash layer.

C) $^{234}U/^{238}U$ activity ratios (red-filled circles) of bulk sediment in core 17JC. Line joining data represents a 3-point running mean. $^{234}U/^{238}U$ activity ratios in marine sediments should record seawater U activity ratios of 1.146 if sediments are purely authigenic. Negative excursions of the bulk sediment U activity ratio from the seawater ratio are indicative of increased input of lithogenic material supplied to the uranium budget of the sediment. This lithogenic uranium fraction is likely derived from aeolian material due to the general anticorrelation between our ^{232}Th dust flux proxy and bulk sediment $^{234}U/^{238}U$ activity ratios records.

D) ^{230}Th-normalized-xsBarium flux (teal-filled circles) record (17JC). Line joining data represents a 3-point running mean. Excess barium (xsBa) was calculated by subtracting the lithogenic Ba from the total Ba concentration using a (Ba/Th) ratio of 51.4 for the continental crust (Taylor & McLennan 1985). Fluxes of xsBa were calculated by normalizing to $xs^{230}Th$-derived mass accumulation rates. Peaks in xsBa fluxes are associated with the peaks in dust fluxes that are consistent with the timing of HS 1, 2, 5, 6, and 7.

E) ^{230}Th-normalized-authigenic U flux (purple-filled circles) record (17JC). Line joining data represents a 3-point running mean. Authigenic U was calculated by subtracting the lithogenic U from the total U concentration using a (U/Th) activity ratio of 0.7 for detrital material delivered to the Pacific Ocean (Henderson & Anderson 2003). Fluxes of authigenic U were calculated by normalizing to $xs^{230}Th$-derived mass accumulation rates. Peaks in authigenic U fluxes are associated with the peaks in dust fluxes that are consistent with the timing of HS 1, 2, 5, 6, and 7.

Age model based on marine oxygen isotope stage boundaries ($\delta^{18}O$ data on thermocline dweller, *N. dutertrei*, in Figure 1), ten radiocarbon tie-points (red triangles), and the Los Chocoyos ash at 84 kyr (Rose et al., 1999) Yellow bars for the Younger Dryas (YD) and Heinrich Stadial (HS) Events 1 through 9 are from (Wang et a., 2001; Rasmussen & Thomsen 2004). Note that the timing of the HS events 1-3 and 7-9 in our age model are coincident with the minima in $\delta^{18}O$ of the NGRIP record. Only for HS events 4-6 is this not the case. We interpret the offset during this time (between 35 and 70 kyr) as due to uncertainties in our age model.

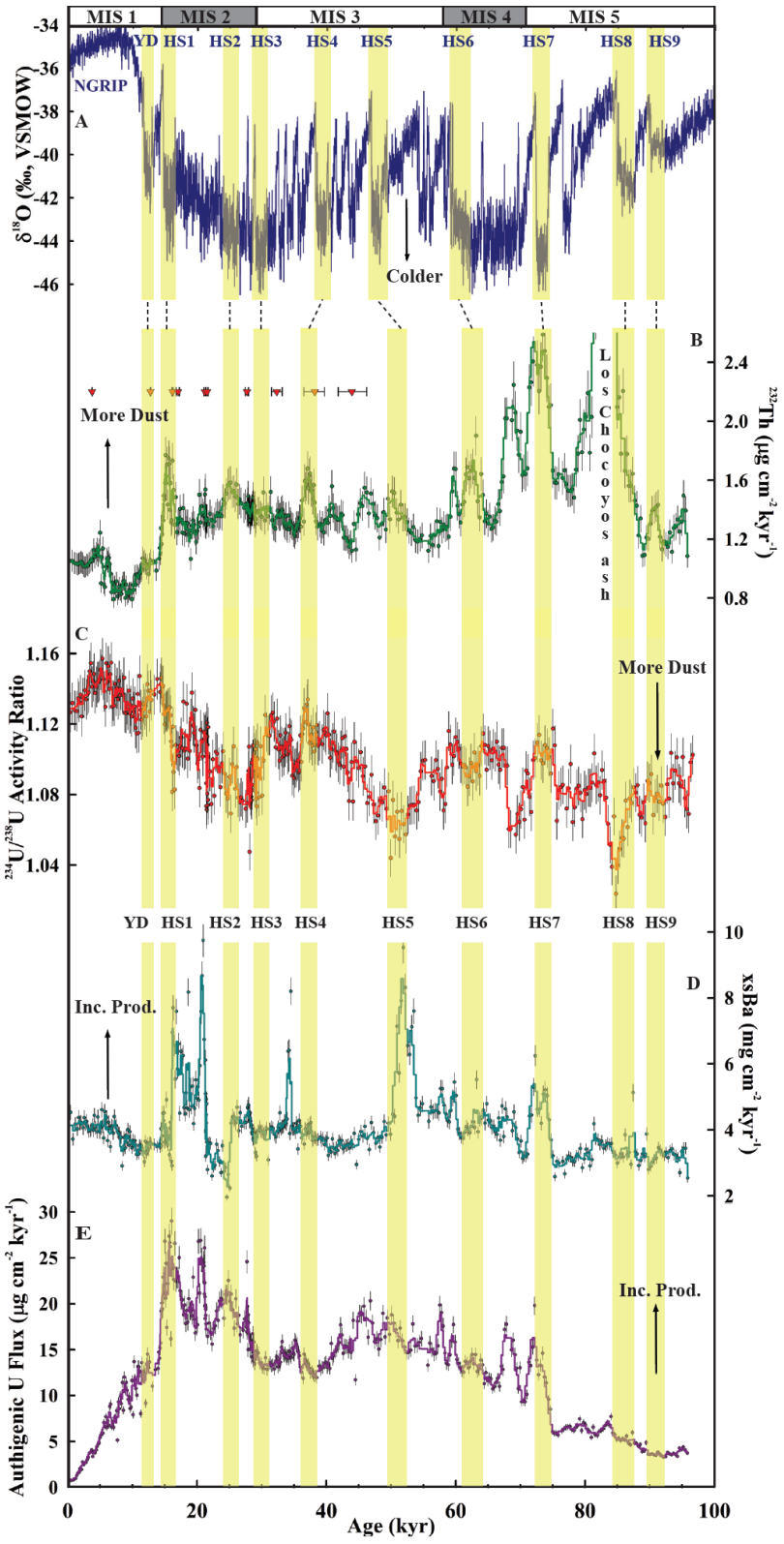
MIS 1
MIS 2
MIS 3
MIS 4
MIS 5
YD
HS1
HS2
HS3
HS4
HS5
HS6
HS7
HS8
HS9
NGRIP
A
δ18O (‰, VSMOW)
Colder
B
More Dust
Los Chocoyos ash
232Th (μg cm-2 kyr-1)
C
234U/238U Activity Ratio
More Dust
D
Inc. Prod.
xsBa (mg cm-2 kyr-1)
E
Authigenic U Flux (μg cm-2 kyr-1)
Inc. Prod.
Age (kyr)

Beyond the period of robust radiocarbon analysis after 40 kyr and the ash layer tie point at 84 kyr, our age model has the largest errors (±500-1,500 yrs). Nevertheless, within this time period, each peak in productivity and dust flux is well within error of HS 4-7, as dated accurately in the U-Th dated Hulu Cave record (Figure 4-2), providing compelling evidence that the peaks in ^{232}Th and productivity fluxes are consistent with the timing of HS Events (Wang et al., 2001). Hence, we feel justified in tuning HS 4 -7 in our record to the Hulu Cave record over this time period (see Methods), and this modification is reflected in the age model presented in Figure 4-5.

Organic carbon and opal concentrations of sediments in nearby core ME0005A-24JC (00° 1.30′ N, 86° 27.79′ W at 2941 m water depth), interpreted to reflect records of productivity and upwelling (Dubois et al., 2011) are also generally higher during HS events (filtered opal record (Dubois et a., 2011) shown in Figure 4-5C), and support our xsBa and authigenic U findings. Increased upwelling in the region during HS events, as suggested by the close tie between the opal and our dust proxy records, seem to be coincident with decreased *Globigerinoides ruber* Mg/Ca sea-surface temperatures (SST) at nearby ODP 1240 (00°1.31’ N, 86°27.76’ W at 2921 m water depth (ref. 20); Figure 4-5E). Given that *G. ruber* is a warm tropical species, its record of SSTs is likely biased to warm seasons, especially during the glacial period, and therefore, reflect minimal cooling, suggesting that colder temperatures may have prevailed. Although colder SSTs may be reflective of either atmospheric cooling or upwelling, we argue that the latter interpretation is more likely given the correlation between upwelling (opal, Figure 4-5C) and low SSTs (Figure 4-5E). For the first time, multiple proxy records from three

nearby sites along the equator in the EEP suggest increases in productivity are correlated with increases in both upwelling and an increased supply of iron through the dissolution of dust. The timing of each of these increases is tightly linked to HS events, suggesting a low-latitude connection to northern hemisphere ocean-atmosphere dynamics. This connection is also borne out in the Holocene part of the record where a correlation between the highest recorded SSTs (Figure 5 3E) and the lowest dust fluxes (Figure 4-5B) between 11 and 5.5 kyr matches the timing of increases in high-latitude northern hemisphere solar insolation and the African Humid Period (deMenocal et al., 2000).

Figure 4-5
A) $\delta^{18}O$ ice core record (blue line) of North Greenland Ice Core Project (NGRIP)

B) ^{230}Th-normalized-^{232}Th flux (green-filled circles) measured as a proxy for dust flux in EEP marine sediment core MV1014-02-17JC (00° 10.8297′ S, 85° 52.0042′ W). Line joining data represents a 3-point running mean. Our adjusted age model between of 40 and 84 kyr is based on the agreement between the absolutely dated (U-Th) Hulu Cave speleothem $\delta^{18}O$ record, the timing of GISP2 temperature changes ref (19), and peaks in ^{232}Th fluxes, i.e., we interpret the peaks in dust fluxes to be consistent with the timing of nearly all HS events with the exception of HS 3. Note that HS 8 is obscured by the proximity to Los Chocoyos ash layer.

C) Opal record (light blue line) of ME0005A-24JC (00° 1.30′ N, 86° 27.79′ W) normalized by filtering the >10-kyr periodicity (Dubois et al., 2011). Opal content (a measure of the presence of siliceous organisms) is used as a proxy for upwelling and productivity. Peaks in opal (i.e. more upwelling) are coincident with the timing of HS events 1, 3, 4, 5, 6, and 8, using an age model (Dubois et al., 2011) that is wholly independent of that for 17JC.

D) ^{230}Th-normalized-authigenic U flux (purple-filled circles) record (17JC, see Figure 4-4 for details). Peaks in authigenic U fluxes are associated with the peaks in dust fluxes and upwelling that are consistent with the timing of nearly all HS events (except HS 3, 8, 9). This suggests a relaxation of iron limitation in the EEP through increased dust delivery and upwelling of nutrient rich deep waters. See caption 4-4B) for age model description.

E) Mg/Ca SST (green line) reconstruction (data based on surface dweller *G. ruber*) for sediment from ODP site (1240 00°1.31’ N, 86°27.76’ W; (Pena et al., 2008). The lowest SSTs are consistent with the timing of nearly all HS events (except HS 6, 8), and may be reflective of atmospheric cooling or increased upwelling. Note, again, that the age model for ODP site 1240 is wholly independent of that for 17JC (here) and 24JC (Dubois et al., 2011).

Yellow bars for the Younger Dryas (YD) and Heinrich Stadial (HS) Events 1 through 9 are from ref (Wang et al., 2001; Rasmussen & Thomsen 2004).

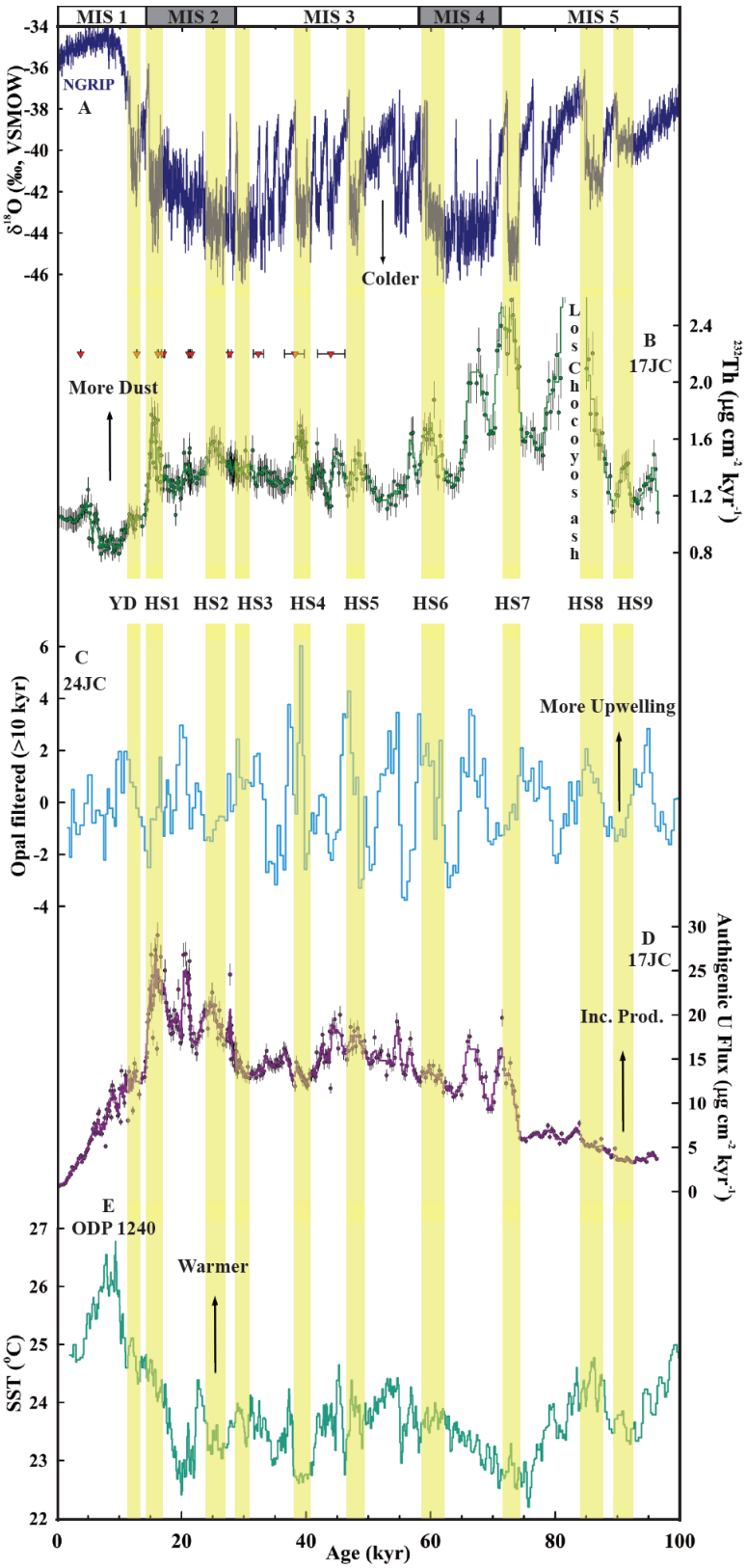
MIS 1
MIS 2
MIS 3
MIS 4
MIS 5
NGRIP
A
$\delta^{18}O$ (‰, VSMOW)
Colder
B
17JC
More Dust
Los Chocoyos ash
^{232}Th (μg cm^{-2} kyr^{-1})
YD HS1 HS2 HS3 HS4 HS5 HS6 HS7 HS8 HS9
C
24JC
Opal filtered (>10 kyr)
More Upwelling
D
17JC
Inc. Prod.
Authigenic U Flux (μg cm^{-2} kyr^{-1})
E
ODP 1240
Warmer
SST (^{o}C)
Age (kyr)

ITCZ Movement and Global Climate Signals

Increased dust flux to the EEP during HS events is consistent with the timing of decreased North Atlantic meridional overturning circulation (McManus et al., 2004) and related shifts in atmospheric circulation, wherein the Indian and Asian Monsoon weaken (Wang et al., 2001; Burns et al., 2003), and the Intertropical Convergence Zone (ITCZ) and westerlies of both hemispheres shifted southward (Peterson et al., 2000). The increased dust flux at the equator in the EEP is likely due to increased aridity and increased dust transport within a strengthened northeasterly trade wind system, suggesting the influence of northern hemisphere climate fluctuations on our equatorial Pacific record. A southward shift of the ITCZ is consistent with decreased runoff recorded in Cariaco Basin sediments during HS events (Peterson et al., 2000). The current average position of the ITCZ in the EEP is at approximately 7°N (Donohoe et a., 2013) so that, today, our site is under the influence of the southeasterly trades during most of the year. Our increased dust flux record at the equator, therefore, suggests a southerly displacement of the ITCZ of at least 7 degrees during HS events (Figure 4-3). In the southern hemisphere, synchronous with the southerly displacement of the ITCZ, are increases in the intensity of the South American summer monsoon and associated wet periods recorded in U-Th dated Peruvian(Kanner et al., 2012) and Brazilian (Wang et al., 2004) speleothems. As previously interpreted, these speleothem records together with the Cariaco and our records suggest an anti-phased relationship between dry versus wet tropical conditions north and south of the equator during HS events, i.e., north of the ITCZ conditions are drier (Cariaco, our site in the EEP) while south of the ITCZ

conditions are wetter (Peru and Brazil). Such a displacement of the ITCZ in the EEP is at odds with an understanding of the modern ITCZ position, using coupled ocean-atmosphere GCMs, which limits its migration due to the orogenic effects of the Andes mountain belt on atmospheric processes (Takahashi & Battisti 2007). Dust provenance studies would help to elucidate the extent of ITCZ shifts in the EEP during abrupt millennial climate change events.

Conclusion

In the Southern Ocean, poleward shifting of the southern hemisphere westerlies is thought to increase upwelling and release CO_2 to the atmosphere during HS climate events (Anderson et al., 2009; Denton et al., 2010) and during the deglaciation. Along the equator in the EP, strengthened NE trade winds, coincident with the southward shift of the ITCZ during HS events can have competing influences on atmospheric CO_2. Strengthened trades increase upwelling and may leak additional advected Southern Ocean intermediate waters rich in nutrients. However, at the same time, these strengthened trades may increase the efficiency of the biological pump by relaxing the limitation of iron in these nutrient-rich upwelled waters through an increase in the supply of continental dust. We suggest that the increased efficiency of the biological pump in the EEP during HS events behaves as a negative feedback to the CO_2 cycle, which may dampen, but does not negate, the global CO_2 rise during HS events.

CHAPTER V

CONCLUSIONS

The grain size study conducted in the EEP on paired thin and thick Panama Basin sites shows that there is indeed biasing of ^{230}Th-normalized sediment MARs and focusing factors (Ψ). For the first time, we were able to clearly document the grain size effect at sites that have undergone a preferential removal of the fine grained sediment fraction (i.e. winnowed sites), as well as sites where preferential deposition of the fine fraction (i.e. focused sites) has occurred. However, we conclude that the bias created is likely no more than 30% for both winnowed and focused sites. We surmise that at sites with $\Psi > 4.1$ there are more significant corrections required (i.e. ~70%). Overall, the ^{230}Th-normalization method remains as a robust paleoceanographic tool for reconstructing sediment fluxes to the deep ocean that have undergone extremes in sediment redistribution. However, an understanding of the grain size distribution of ^{230}Th would be advised when utilizing the ^{230}Th-normalization method.

Borne out of our grain size study, we found anonymously high concentrations of authigenic U in the fine fraction of our studied LGM samples. Since authigenic U emplacement in the sediments is a redox driven process it has been used as either a proxy for biologic productivity or bottom water oxygen. We investigated the down core authigenic U profiles of both our paired Panama Basin thin (4JC, 11JC) and thick (8JC,17JC) Cocos and Carnegie Ridge sites. It appears that our paired thin (4JC) Cocos and Carnegie Ridge (11JC) sites have been affected by early sediment diagenesis by

organic matter burn down through a relaxation of pore water oxygen during the latest Holocene. A model of the burn down depths (i.e. the depth at which authigenic U is immobilized) corroborates our findings of early sediment diagenesis at our thin (4JC, 11JC) sites. The Cocos Ridge thick (8JC) site has undergone partial burn down of organic matter. At our high accumulation Carnegie Ridge (17JC) site, the authigenic U profile remains relatively unaffected by diagenetic processes and is likely reflecting a true down core profile that tracks changes in productivity.

With our investigations into understanding the potential biasing of U-Th derived paleoceanographic tools complete, we reconstructed a full 10-m (100-kyr) deep sea sediment core multi-proxy record from the Carnegie Ridge (17JC). Specifically, using our own generated records of U-Th and Ba, along with previously published records of opal and sea-surface temperature from nearby cores, we investigated the iron fertilization hypothesis in the EEP. Coincident with abrupt cold Northern Hemisphere Heinrich stadial events, there are increased dust fluxes (i.e. increased iron deposition) that correlate with increased productivity. It is likely that the relaxation of iron limitation (i.e. through increased dust flux and upwelling of nutrient-rich deep waters) drove a more efficient biologic pump during Heinrich events. However, the impact of increased rates of primary production acted more as negative feedback on global CO_2 levels which are thought to have been rising at the same time due to ventilation of deep Southern Ocean waters. In addition, we postulate that there is potentially large-scale (e.g. a minimum of 7°) southward shift in the ITCZ during Heinrich stadial events. However, further investigations and verification into the possible magnitude of the ITCZ

movement is needed. Our hypothesis that iron fertilization took place through increased dust deposition suggests an atmospheric role for the teleconnection between the low latitude EEP and cold North Atlantic Heinrich stadial events on millennial timescales.

REFERENCES

Albani, S., Mahowald, N. M., Murphy, L. N., Raiswell, R., Moore, J. K., Anderson, R. F., McGee, D., Bradtmiller, L.I., Delmonte, B., Hesse, P.P. and Mayewski, P.A., (2016) Paleodust variability since the Last Glacial Maximum and implications for iron inputs to the ocean. *Geophysical Research Letters*, *43*(8), 3944-3954

Anderson, R. F. (1982). Concentration, vertical flux, and remineralization of particulate uranium in seawater. *Geochimica et Cosmochimica Acta*, *46*(7), 1293-1299.

Anderson, R. F., Kumar, N., Mortlock, R. A., Froelich, P. N., Kubik, P., Dittrich-Hannen, B., & Suter, M. (1998). Late-Quaternary changes in productivity of the Southern Ocean. *Journal of Marine Systems*, *17*(1), 497-514

Anderson, R. F., Chase, Z., Fleisher, M. Q., & Sachs, J. (2002). The Southern Ocean's biological pump during the last glacial maximum. *Deep Sea Research Part II: Topical Studies in Oceanography*, *49*(9), 1909-1938.

Anderson, R. F., Fleisher, M. Q., & Lao, Y. (2006). Glacial–interglacial variability in the delivery of dust to the central equatorial Pacific Ocean.*Earth and Planetary Science Letters*, *242*(3), 406-414

Anderson, R. F., Fleisher, M. Q., Lao, Y., & Winckler, G. (2008). Modern CaCO3 preservation in equatorial Pacific sediments in the context of late-Pleistocene glacial cycles. *Marine Chemistry*, *111*(1), 30-46.

Anderson, R. F., Ali, S., Bradtmiller, L. I., Nielsen, S. H. H., Fleisher, M. Q., Anderson, B. E., & Burckle, L. H. (2009). Wind-driven upwelling in the Southern Ocean and the deglacial rise in atmospheric CO2. *science*, *323*(5920), 1443-1448.

Bacon, M.P., and Anderson R. F. (1982), Distribution of Thorium isotopes between dissolved and particulate forms in the deep sea, Geophysical Research Lett., 87, 2045-2056

Barnes, C. E., & Cochran, J. K. (1990). Uranium removal in oceanic sediments and the oceanic U balance. *Earth and Planetary Science Letters*, *97*(1), 94-101.

Bonatti, E., Fisher, D. E., Joensuu, O., & Rydell, H. S. (1971). Postdepositional mobility of some transition elements, phosphorus, uranium and thorium in deep sea sediments. *Geochimica et cosmochimica acta*, *35*(2), 189-201

Bista, D. (2015). Reconstructing Dust Fluxes and Sediment Focusing in the Equatorial Pacific Over Glacial and Interglacial Time-scales Using Grain Size Analysis, Dalhousie University Master's thesis

Bradtmiller, L. I., Anderson, R. F., Fleisher, M. Q., & Burckle, L. H. (2006). Diatom productivity in the equatorial Pacific Ocean from the last glacial period to the present: A test of the silicic acid leakage hypothesis.*Paleoceanography*, *21*(4

Bradtmiller, L. I., Anderson, R. F., Fleisher, M. Q., & Burckle, L. H. (2009). Comparing glacial and Holocene opal fluxes in the Pacific sector of the Southern Ocean. *Paleoceanography*, *24*

Burns, S. J., Fleitmann, D., Matter, A., Kramers, J., & Al-Subbary, A. A. (2003). Indian Ocean climate and an absolute chronology over Dansgaard/Oeschger events 9 to 13. *Science*, *301*(5638), 1365-1367.

Cai, W. J., & Sayles, F. L. (1996). Oxygen penetration depths and fluxes in marine sediments. *Marine Chemistry*, *52*(2), 123-131.

Calvert, S. E., & Pedersen, T. F. (1993). Geochemistry of recent oxic and anoxic marine sediments: implications for the geological record. *Marine geology*, *113*(1), 67-88.

Chase, Z., Anderson, R. F., & Fleisher, M. Q. (2001). Evidence from authigenic uranium for increased productivity of the glacial Subantarctic Ocean. *Paleoceanography*, *16*(5), 468-478.

Chavez, F. P., & Barber, R. T. (1987). An estimate of new production in the equatorial Pacific. *Deep Sea Research Part A. Oceanographic Research Papers*, *34*(7), 1229-1243.

Colley, S., Thomson, J., Wilson, T. R. S., & Higgs, N. C. (1984). Post-depositional migration of elements during diagenesis in brown clay and turbidite sequences in the North East Atlantic. *Geochimica et Cosmochimica Acta*, *48*(6), 1223-1235.

Costa, K. M., McManus, J. F., Anderson, R. F., Ren, H., Sigman, D. M., Winckler, Fleisher M. Q., Marcantonio, F., Ravelo, A. C. (2016). No iron fertilization in the equatorial Pacific Ocean during the last ice age. *Nature*, *529*(7587), 519-522

deMenocal, P.B, Ortiz, J., Guilderson, T., Adkins, J., Sarnthein, M., Baker, L., and Yarusinski, M. (2000). Abrupt onset and termination of the African Humid Period: rapid climate responses to gradual insolation forcing. *Quaternary science reviews*, *19*(1), 347-361.

Denton, G. H., Anderson, R. F., Toggweiler, J. R., Edwards, R. L., Schaefer, J. M., & Putnam, A. E. (2010). The last glacial termination. *Science*, *328*(5986), 1652-1656.

Donnadieu, Y., Lecroart, P., Anschutz, P., & Bertrand, P. (2002). Bias in the paleoceanographic time series: Tests with a numerical model of U, Corg, and Al burial. *Paleoceanography*, *17*(3), 6-1.

Donohoe, A., Marshall, J., Ferreira, D., & Mcgee, D. (2013). The relationship between ITCZ location and cross-equatorial atmospheric heat transport: From the seasonal cycle to the Last Glacial Maximum. *Journal of Climate*, *26*(11), 3597-3618.

Dean, W. E., Gardner, J. V., & Piper, D. Z. (1997). Inorganic geochemical indicators of glacial-interglacial changes in productivity and anoxia on the California continental margin. *Geochimica et Cosmochimica Acta*, *61*(21), 4507-4518

Dubois, N., Kienast, M., Kienast, S., Calvert, S. E., François, R., & Anderson, R. F. (2010). Sedimentary opal records in the eastern equatorial Pacific: It is not all about leakage. *Global Biogeochemical Cycles*, *24*(4)

Dubois, N., Kienast, M., Kienast, S., Normandeau, C., Calvert, S. E., Herbert, T. D., & Mix, A. (2011). Millennial-scale variations in hydrography and biogeochemistry in the Eastern Equatorial Pacific over the last 100 kyr. *Quaternary Science Reviews*, *30*(1), 210-223.

Dymond, J., Suess, E., & Lyle, M. (1992). Barium in deep-sea sediment: A geochemical proxy for paleoproductivity. *Paleoceanography*, *7*(2), 163-181.

Francois, R., Bacon, M. P., Altabet, M. A., & Labeyrie, L. D. (1993). Glacial/interglacial changes in sediment rain rate in the SW Indian sector of Subantarctic waters as recorded by 230Th, 231Pa, U, and δ15N.*Paleoceanography*, *8*(5), 611-629

Francois, R., Honjo, S., Manganini, S. J., & Ravizza, G. E. (1995). Biogenic barium fluxes to the deep sea: Implications for paleoproductivity reconstruction. *Global Biogeochemical Cycles*, *9*(2), 289-303

Francois, R., Bacon, M. P., Altabet, M. A., & Labeyrie, L. D. (1993). Glacial/interglacial changes in sediment rain rate in the SW Indian sector of Subantarctic waters as recorded by 230Th, 231Pa, U, and δ15N *Paleoceanography*, *8*(5), 611-629.

Franois, R., Altabet, M.A., Yu, E.F., Sigman, D.M., Bacon, M.P., Frank, M., Bohrmann, G., Bareille, G. and Labeyrie, L.D., (1997). Contribution of Southern Ocean surface-water stratification to low atmospheric CO2 concentrations during the last glacial period. *Nature*, *389*(6654), pp.929-935.

Francois, R., Frank, M., Rutgers van der Loeff, M. M., & Bacon, M. P. (2004). 230Th normalization: An essential tool for interpreting sedimentary fluxes during the late Quaternary. *Paleoceanography*, *19*(1)

Fiedler, P. C., & Talley, L. D. (2006). Hydrography of the eastern tropical Pacific: A review. *Progress in Oceanography*, *69*(2), 143-180.

Froelich, P., Klinkhammer, G. P., Bender, M. A. A., Luedtke, N. A., Heath, G. R., Cullen, D., & Maynard, V. (1979). Early oxidation of organic matter in pelagic sediments of the eastern equatorial Atlantic: suboxic diagenesis. *Geochimica et Cosmochimica Acta*, *43*(7), 1075-1090.

Geibert, W., and R. Usbeck (2004), Adsorption of thorium and protactinium onto different particle types: Experimental findings, Geochim. Cosmochim.Acta, 68, 1489–1501.

Gibbs, R. J., Matthews, M. D., & Link, D. A. (1971). The relationship between sphere size and settling velocity. *Journal of Sedimentary Research*, *41*(1), 7-18.

Graybeal, A. L., & Heath, G. R. (1984). Remobilization of transition metals in surficial pelagic sediments from the eastern Pacific. *Geochimica et Cosmochimica Acta*, *48*(5), 965-975.

Griffith, E. M., & Paytan, A. (2012). Barite in the ocean–occurrence, geochemistry and palaeoceanographic applications. *Sedimentology*, *59*(6), 1817-1835.

Hayes, C. T., Anderson, R. F., & Fleisher, M. Q. (2011). Opal accumulation rates in the equatorial Pacific and mechanisms of deglaciation.*Paleoceanography*, *26*(1)

Heath, G. R., Moore Jr, T. C., & Roberts, G. L. (1974). Mineralogy of surface sediments from the Panama Basin, eastern equatorial Pacific. *The Journal of Geology*, *82*(2), 145-160.

Henderson, G.M. (2002), Seawater (234U/238U) during the last 800 thousand years, Earth and Planetary Sci. Let., 199, 97-110

Henderson, G.M., Anderson, R.F., (2003), The U-series toolbox for paleoceanography. Reviews of Mineralology and Geochemistry 52, 493–531.

Hertzberg, J. E., Schmidt, M. W., Bianchi, T. S., Smith, R. W., Shields, M. R., & Marcantonio, F. (2016). Comparison of eastern tropical Pacific TEX 86 and Globigerinoides ruber Mg/Ca derived sea surface temperatures: Insights from the Holocene and Last Glacial Maximum. *Earth and Planetary Science Letters*, *434*, 320-332

Jacobel, A. W., McManus, J. F., Anderson, R. F., & Winckler, G. (2016). Large deglacial shifts of the Pacific Intertropical Convergence Zone. *Nature communications*, *7*.

Jacobel, A. W., McManus, J. F., Anderson, R. F., & Winckler, G. (2017). Climate-related response of dust flux to the central equatorial Pacific over the past 150 kyr. *Earth and Planetary Science Letters*, *457*, 160-172.

Jung, M., Ilmberger, J., Mangini, A., & Emeis, K. C. (1997). Why some Mediterranean sapropels survived burn-down (and others did not). *Marine Geology*, *141*(1), 51-60.

Kanner, L. C., Burns, S. J., Cheng, H., & Edwards, R. L. (2012). High-latitude forcing of the South American summer monsoon during the last glacial. *Science*, *335*(6068), 570-573.

Kienast, S. S., Kienast, M., Jaccard, S., Calvert, S. E., & François, R. (2006). Testing the silica leakage hypothesis with sedimentary opal records from the eastern equatorial Pacific over the last 150 kyrs. *Geophysical Research Letters*, *33*(15)

Kienast, M., Kienast, S. S., Calvert, S. E., Eglinton, T. I., Mollenhauer, G., François, R., & Mix, A. C. (2006). Eastern Pacific cooling and Atlantic overturning circulation during the last deglaciation. *Nature*, *443*(7113), 846-849

Kienast, S. S., Kienast, M., Mix, A. C., Calvert, S. E., & Francois, R. (2007). Thorium-230 normalized particle flux and sediment focusing in the Panama Basin region during the last 30,000 years. *Paleoceanography*, *22*(2)

Kienast, S. S., Friedrich, T., Dubois, N., Hill, P. S., Timmermann, A., Mix, A. C., & Kienast, M. (2013). Near collapse of the meridional SST gradient in the eastern equatorial Pacific during Heinrich Stadial 1. *Paleoceanography*,*28*(4), 663-674

Komar, P. D., & Reimers, C. E. (1978). Grain shape effects on settling rates. *The Journal of Geology*, 193-209

Klinkhammer, G. P., & Palmer, M. R. (1991). Uranium in the oceans: where it goes and why. *Geochimica et Cosmochimica Acta*, *55*(7), 1799-1806.

Klinkhammer, G. P. (1980). Early diagenesis in sediments from the eastern equatorial Pacific, II. Pore water metal results. *Earth and Planetary Science Letters*, *49*(1), 81-101.

Koutavas, A., & Lynch-Stieglitz, J. (2004). Variability of the marine ITCZ over the eastern Pacific during the past 30,000 years. In *The Hadley Circulation: Present, Past and Future* (pp. 347-369). Springer Netherlands.

Kowsmann, R. O. (1973). Coarse components in surface sediments of the Panama Basin, eastern equatorial Pacific. *The Journal of Geology*, *81*(4), 473-494

Kretschmer, S., Geibert, W., van der Loeff, M. M. R., Mollenhauer, G. (2010) Grains size effects on ^{230}Thxs inventories in opal-rich and carbonate-rich marine sediments, *Earth and Planetary Science Letters,* 294, 131-142.

Kumar, N., Anderson, R. F., Mortlock, R. A., Froelich, P. N., Kubik, P., Dittrich-Hannen, B., & Suter, M. (1995). Increased biological productivity and export production in the glacial Southern Ocean. *Nature*, *378*(6558), 675-680

Loubere, P., Mekik, F., Francois, R., & Pichat, S. (2004). Export fluxes of calcite in the eastern equatorial Pacific from the Last Glacial Maximum to present. *Paleoceanography*, *19*(2

Loubere, P., & Richaud, M. (2007). Some reconciliation of glacial-interglacial calcite flux reconstructions for the eastern equatorial Pacific. *Geochemistry, Geophysics, Geosystems*, *8*(3)

Loveley, M. R., Marcantonio, F., Ibrahim, R., Hertzberg, J., Schmidt, M. W., (2017) Sediment redistribution and grain size effects on 230Th-normalized focusing factors and mass accumulation rates in the Panama Basin. *Earth and Planetary Science Letters* (In-Reivew)

Lyle, A. O., & Lyle, M. W. (2002). Determination of biogenic opal in pelagic marine sediments: a simple method revisited. In *Proceedings of the Ocean Drilling Program, Initial Reports* (Vol. 199, pp. 1-21).

Lyle, M., Mix, A., & Pisias, N. (2002). Patterns of CaCO3 deposition in the eastern tropical Pacific Ocean for the last 150 kyr: Evidence for a southeast Pacific depositional spike during marine isotope stage (MIS) 2.*Paleoceanography*, *17*(2)

Lyle, M., A. Mix, A. C. Ravelo, D. Andreasen, L. Heusser, and A. Olivarez (2000), Millennial-scale CaCO3 and Corg events along the northern and central California margin: Stratigraphy and origins, Proc. Ocean Drill. Program Sci. Results, 167, 163–182, doi:10.2973/odp.proc.sr.167.214.2000

Lyle, M. (1983). The brown-green color transition in marine sediments: A marker of the Fe (III)-Fe (II) redox boundary1. *Limnology and Oceanography*, *28*(5), 1026-1033.

Lyle, M., Marcantonio, F., Moore, W.S., Murray, R.W., Huh, C.-A., Finney, B.P., Murray, D.W., Mix, A.C., (2014). Sediment size fractionation and sediment focusing in the equatorial Pacific: effect on ^{230}Th normalization and paleoflux measurements. Paleoceanography 29 (7), 747-763

Mahowald, N., Kohfeld, K., Hansson, M., Balkanski, Y., Harrison, S. P., Prentice, I.C., Schulz, M. and Rodhe, H., (1999). Dust sources and deposition during the last glacial maximum and current climate: A comparison of model results with paleodata from ice cores and marine sediments. *Journal of Geophysical Research: Atmospheres*, *104*(D13), 15895-15916.

Mangini, A., Jung, M., & Laukenmann, S. (2001). What do we learn from peaks of uranium and of manganese in deep sea sediments?. *Marine Geology*, *177*(1), 63-78

Marcantonio, F., Anderson, R. F., Higgins, S., Stute, M., Schlosser, P., & Kubik, P. (2001). Sediment focusing in the central equatorial Pacific Ocean. *Paleoceanography*, *16*(3), 260-267

Marcantonio, F., Lyle, M., & Ibrahim, R. (2014). Particle sorting during sediment redistribution processes and the effect on 230Th-normalized mass accumulation rates. *Geophysical Research Letters*, *41*(15), 5547-5554.

Martin, J. H. (1990). Glacial-interglacial CO2 change: The iron hypothesis. *Paleoceanography*, *5*(1), 1-13.

Mekik, F. A., Anderson, R. F., Loubere, P., François, R., & Richaud, M. (2012). The mystery of the missing deglacial carbonate preservation maximum. *Quaternary Science Reviews*, *39*, 60-72

Meyers, S. R. (2007). Production and preservation of organic matter: The significance of iron. *Paleoceanography*, *22*(4).

McCave, I. N., & Hall, I. R. (2006). Size sorting in marine muds: Processes, pitfalls, and prospects for paleoflow-speed proxies. *Geochemistry, Geophysics, Geosystems*, *7*(10).

McGee, D., Winckler, G., Borunda, A., Serno, S., Anderson, R. F., Recasens, C., Bory, A., Gaiero, D., Jaccard, S.L., Kaplan, M. & McManus, J. F. (2016). Tracking eolian dust with helium and thorium: impacts of grain size and provenance. *Geochimica et Cosmochimica Acta*, *175*, 47-67.

McGee, D., F.Marcantonio, J. F.McManus, and G. Winckler (2010), The response of excess ^{230}Th and extraterrestrial ^{3}He to sediment redistribution at the Blake Ridge, western North Atlantic, Earth Planet. Sci. Lett., 299, 138–149.

McGee, D., Marcantonio, F., & Lynch-Stieglitz, J. (2007). Deglacial changes in dust flux in the eastern equatorial Pacific. *Earth and Planetary Science Letters*, *257*(1), 215-230

McManus, J., Berelson, W. M., Klinkhammer, G. P., Hammond, D. E., & Holm, C. (2005). Authigenic uranium: relationship to oxygen penetration depth and organic carbon rain. *Geochimica et Cosmochimica Acta*, *69*(1), 95-108.

McManus, J. F., Francois, R., Gherardi, J. M., Keigwin, L. D., & Brown-Leger, S. (2004). Collapse and rapid resumption of Atlantic meridional circulation linked to deglacial climate changes. *Nature*, *428*(6985), 834-837

Mollier-Vogel, E., Leduc, G., Böschen, T., Martinez, P., & Schneider, R. R. (2013). Rainfall response to orbital and millennial forcing in northern Peru over the last 18 ka. *Quaternary Science Reviews*, *76*, 29-38.

Moore Jr, T. C., Heath, G. R., & Kowsmann, R. O. (1973). Biogenic sediments of the Panama Basin. *The Journal of Geology*, *81*(4), 458-472.

Murray, J. W., Barber, R. T., Roman, M. R., Bacon, M. P., & Feely, R. A. (1994). Physical and biological controls on carbon cycling in the equatorial Pacific. *Science*, *266*(5182), 58-65

Murray, R. W., Leinen, M., & Knowlton, C. W. (2012). Links between iron input and opal deposition in the Pleistocene equatorial Pacific Ocean. *Nature Geoscience*, *5*(4), 270-274.

Nameroff, T. J., Balistrieri, L. S., & Murray, J. W. (2002). Suboxic trace metal geochemistry in the eastern tropical North Pacific. *Geochimica et Cosmochimica Acta*, *66*(7), 1139-1158.

Nozaki, Y., Horibe, Y., Tsubota, H., (1981) The water column distributions of thorium isotopes in the Western North Pacific, Earth and Planetary Sci. Lett. 54 (2), 203–216.

Olivarez A.M., R.M. Owen, D.K. Rea, Geochemistry of eolian dust in pacific pelagic sediments implications for paleoclimatic interpretations, Geochim. Cosmochim. Acta 55 (1991)

Pahnke, K., Sachs, J. P., Keigwin, L., Timmermann, A., & Xie, S. P. (2007). Eastern tropical Pacific hydrologic changes during the past 27,000 years from D/H ratios in alkenones. *Paleoceanography*, *22*(4).

Paillard, D., Labeyrie, L., & Yiou, P. (1996). Macintosh program performs time-series analysis. *Eos, Transactions American Geophysical Union*,*77*(39), 379-379

Pailler, D., Bard, E., Rostek, F., Zheng, Y., Mortlock, R., & van Geen, A. (2002). Burial of redox-sensitive metals and organic matter in the equatorial Indian Ocean linked to precession. *Geochimica et Cosmochimica Acta*,*66*(5), 849-865.

Paytan, A., Kastner, M., & Chavez, F. P. (1997). Glacial to interglacial fluctuations in productivity in the Equatorial Pacific as indicated by marine barite. *Oceanographic Literature Review*, *5*(44), 460

Pena, L. D., Cacho, I., Ferretti, P., & Hall, M. A. (2008). El Niño–Southern Oscillation–like variability during glacial terminations and interlatitudinal teleconnections. *Paleoceanography*, *23*(3).

Pennington, J. T., Mahoney, K. L., Kuwahara, V. S., Kolber, D. D., Calienes, R., & Chavez, F. P. (2006). Primary production in the eastern tropical Pacific: A review. *Progress in Oceanography*, *69*(2), 285-317

Peterson, L. C., Haug, G. H., Hughen, K. A., & Röhl, U. (2000). Rapid changes in the hydrologic cycle of the tropical Atlantic during the last glacial. *Science*, *290*(5498), 1947-1951.

Rasmussen, T. L., & Thomsen, E. (2004). The role of the North Atlantic Drift in the millennial timescale glacial climate fluctuations. *Palaeogeography, Palaeoclimatology, Palaeoecology*, *210*(1), 101-116.

Reimer, P. J., Bard, E., Bayliss, A., Beck, J. W., Blackwell, P. G., Bronk Ramsey, C., Buck, C.E., Cheng, H., Edwards, R.L., Friedrich,& Grootes, P. M. (2013). IntCal13 and Marine13 radiocarbon age calibration curves 0-50,000 years cal BP.

Rincón-Martínez, D., Lamy, F., Contreras, S., Leduc, G., Bard, E., Saukel, C.,& Tiedemann, R. (2010). More humid interglacials in Ecuador during the past 500 kyr linked to latitudinal shifts of the equatorial front and the Intertropical Convergence Zone in the eastern tropical Pacific. *Paleoceanography*, *25*(2).

Rose, W. I., Conway, F. M., Pullinger, C. R., Deino, A., & McIntosh, W. C. (1999). An improved age framework for late Quaternary silicic eruptions in northern Central America. *Bulletin of Volcanology*, *61*(1-2), 106-120.

Scholten, J.C., et al., (2005) Radionuclide fluxes in the Arabian Sea: the role of particle composition. Earth and Planetary Science Letters, 230, 319–337.

Schulz, H. D., Dahmke, A., Schinzel, U., Wallmann, K., & Zabel, M. (1994). Early diagenetic processes, fluxes, and reaction rates in sediments of the South Atlantic. *Geochimica et Cosmochimica Acta*, *58*(9), 2041-2060.

Seillès, B., Goñi, M. F. S., Ledru, M. P., Urrego, D. H., Martinez, P., Hanquiez, V., & Schneider, R. (2015). Holocene land–sea climatic links on the equatorial Pacific coast (Bay of Guayaquil, Ecuador). *The Holocene*

Siddall, M., Anderson, R.F., Winckler, G., Henderson, G.M., Bradtmiller, L.I., McGee, D., Franzese, A.,

Stocker, T.F., Muller, S.A., (2008) Modeling the particle flux effect on distribution of 230Th in the equatorial Pacific. Paleoceanography 23, PA2208

Singh, A. K., F. Marcantonio, and M. Lyle (2011), Sediment focusing in the Panama Basin, eastern equatorial Pacific Ocean, Earth Planet. Sci. Lett., 309, 33–44.

Snoeckx, H., & Rea, D. K. (1994). Dry bulk density and CaCO3 relationships in upper Quaternary sediments of the eastern equatorial Pacific. *Marine Geology*, *120*(3-4), 327-333

Stuiver, M., Reimer, P. J., & Reimer, R. (2006). CALIB radiocarbon calibration. *Execute version*, *5*.0.2html

Suman D.O., Bacon M.P (1989) Variations in Holocene sedimentation in the North American Basin determined by ^{230}Th measurements Deep-Sea Res., 36, 869–878

S.R. Taylor, S.M. McLennan, The Continental Crust: Its Composition and Evolution, Blackwell Scientific, Oxford, 1985

Stuiver, M., & Reimer, P. J. (1993). Extended 14 C data base and revised CALIB 3.0 14 C age calibration program. *Radiocarbon*, *35*(01), 215-230.

Takahashi, K., & Battisti, D. S. (2007). Processes controlling the mean tropical Pacific precipitation pattern. Part I: The Andes and the eastern Pacific ITCZ. *Journal of Climate*, *20*(14), 3434-3451.

Thomas, E., Turekian, K. K., & Wei, K. Y. (2000). Productivity control of fine particle transport to equatorial Pacific sediment. *Global Biogeochemical Cycles*, *14*(3), 945-955

Thomson, J., Wilson, T. R. S., Culkin, F., & Hydes, D. J. (1984). Non-steady state diagenetic record in eastern equatorial Atlantic sediments. *Earth and planetary science letters*, *71*(1), 23-30.

Thomson, J., Wallace, H. E., Colley, S., & Toole, J. (1990). Authigenic uranium in Atlantic sediments of the last glacial stage—a diagenetic phenomenon. *Earth and Planetary Science Letters*, *98*(2), 222-232

Thomson, J., Colley, S., Anderson, R., Cook, G.T., MacKenzie, A.B., Harkness, D.D.,(1993) Holocene sediment fluxes in the Northeast Atlantic from 230Thexcess and Radiocarbon Measurements. Paleoceanography 8, 631–650.

Thomson, J., Higgs, N. C., Croudace, I. W., Colley, S., & Hydes, D. J. (1993). Redox zonation of elements at an oxic/post-oxic boundary in deep-sea sediments. *Geochimica et Cosmochimica Acta*, *57*(3), 579-595.

Thomson, J., Higgs, N. C., & Colley, S. (1996). Diagenetic redistributions of redox-sensitive elements in northeast Atlantic glacial/interglacial transition sediments. *Earth and Planetary Science Letters*, *139*(3), 365-377.

Van Andel, T. H. (1973). Texture and dispersal of sediments in the Panama Basin. *The Journal of Geology*, *81*(4), 434-457.

Van derLoeff, M.M.R., Berger,G.W.,(1993) Scavenging of Th-230 andPa-231 near the Antarctic Polar Front in the South-Atlantic. Deep-Sea Res.Part I—Oceanogr. Res.Pap. 40(2), 339–357.

Wadell, H. (1932). Volume, shape, and roundness of rock particles. *The Journal of Geology*, 443-451.

Wadell, H. (1934). Some new sedimentation formulas. *Journal of Applied Physics*, *5*(10), 281-291.

Wallace, H. E., Thomson, J., Wilson, T. R. S., Weaver, P. P. E., Higgs, N. C., & Hydes, D. J. (1988). Active diagenetic formation of metal-rich layers in NE Atlantic sediments. *Geochimica et Cosmochimica Acta*, *52*(6), 1557-1569.

Wang, Y. J., Cheng, H., Edwards, R. L., An, Z. S., Wu, J. Y., Shen, C. C., & Dorale, J. A. (2001). A high-resolution absolute-dated late Pleistocene monsoon record from Hulu Cave, China. *Science*, *294*(5550), 2345-2348.

Wang, X., Auler, A. S., Edwards, R. L., Cheng, H., Cristalli, P. S., Smart, P.L., Richards, D.A. and Shen, C.C., (2004). Wet periods in northeastern Brazil over the past 210 kyr linked to distant climate anomalies. *Nature*, *432*(7018), 740-743.

Wilson, T. R. S., Thomson, J., Colley, S., Hydes, D. J., Higgs, N. C., & Sørensen, J. (1985). Early organic diagenesis: the significance of progressive subsurface oxidation fronts in pelagic sediments. *Geochimica et Cosmochimica Acta*, *49*(3), 811-822.

Winckler, G., Anderson, R. F., & Schlosser, P. (2005). Equatorial Pacific productivity and dust flux during the mid-Pleistocene climate transition. *Paleoceanography*, *20*(4).

Winckler, G., Anderson, R. F., Fleisher, M. Q., McGee, D., & Mahowald, N. (2008). Covariant glacial-interglacial dust fluxes in the equatorial Pacific and Antarctica. *science*, *320*(5872), 93-96

Winckler, G., Anderson, R. F., Jaccard, S. L., & Marcantonio, F. (2016). Ocean dynamics, not dust, have controlled equatorial Pacific productivity over the past 500,000 years. *Proceedings of the National Academy of Sciences*, *113*(22), 6119-6124.

Yamada, M., & Tsunogai, S. (1984). Postdepositional enrichment of uranium in sediment from the Bering Sea. *Marine geology*, *54*(3), 263-276.

Yu, E.-F., R. Francois, M. P. Bacon, S. Honjo, A. P. Fleer, S. J. Manganini, M. M. Rutgers van der Loeff and V. Ittekkot. (2001) Trapping efficiency of bottom- tethered sediment traps estimated from the intercepted fluxes of 230Th and 231Pa. Deep-Sea Res. I, 48, 865-889.

Zheng, Y., Anderson, R. F., van Geen, A., & Fleisher, M. Q. (2002). Remobilization of authigenic uranium in marine sediments by bioturbation.*Geochimica et Cosmochimica Acta*, *66*(10), 1759-1772.

Ziegler, M., Diz, P., Hall, I. R., & Zahn, R. (2013). Millennial-scale changes in atmospheric CO2 levels linked to the Southern Ocean carbon isotope gradient and dust flux. *Nature Geoscience*, *6*(6), 457-461.

APPENDIX A

Ave depth (cm)	Age (kyr)	^{230}Th-derived MAR (g cm^{-2} kyr^{-1})	^{232}Th MAR (µg cm^{-2} kyr^{-1})	^{234}U/^{238}U	authigenic U (ppm)	authigenic U MAR (µg cm^{-2} kyr^{-1})	xsBa MAR (mg cm^{-2} kyr^{-1})
2	0.18	1.19	1.05	1.13	0.51	0.61	4.53
6	0.53	1.08	1.05	1.13	0.69	0.74	3.72
10	0.88	1.17	1.04	0.74	1.14	1.33	4.17
14	1.24	1.13	1.03	1.39	0.85	0.96	4.03
16	1.42	1.19	1.03	1.13	1.08	1.29	4.37
18	1.59	1.15	1.03	1.13	1.34	1.54	4.21
20	1.77	1.15	1.04	1.14	1.41	1.61	4.23
22	1.95	1.11	1.05	1.12	1.85	2.04	8.64
24	2.12	1.13	1.04	1.13	1.71	1.93	4.06
26	2.30	1.18	1.02	1.13	2.34	2.77	4.37
28	2.48	1.18	1.01	1.14	2.09	2.46	4.19
30	2.65	1.17	1.01	1.13	2.28	2.68	4.26
32	2.83	1.09	1.03	1.14	2.47	2.68	4.09
34	3.01	1.12	1.02	1.14	2.68	3.00	3.97
36	3.18	1.13	1.04	1.15	2.88	3.25	3.98
38	3.36	1.14	1.05	1.15	3.27	3.73	4.01
40	3.54	1.21	1.06	1.14	3.17	3.84	4.14
42	3.72	1.14	1.05	1.14	3.59	4.08	3.99
44	3.87	1.15	1.13	1.15	2.91	3.34	4.44
46	4.02	1.15	1.08	1.14	3.34	3.83	4.07
49	4.24	1.10	1.10	1.14	3.41	3.77	3.94
51	4.39	1.17	1.13	1.14	3.47	4.07	4.39
53	4.54	1.21	1.09	1.14	3.65	4.43	10.67
55	4.69	1.24	1.13	1.14	3.78	4.69	3.93
57	4.84	1.26	1.24	1.15	3.84	4.84	4.06
59	4.99	1.22	0.90	1.15	4.41	5.40	4.61
61	5.14	1.28	1.08	1.16	4.44	5.70	4.11
63	5.30	1.21	1.14	1.15	4.91	5.94	3.75
65	5.45	1.29	0.89	1.14	4.56	5.90	4.55
67	5.60	1.46	0.88	1.13	4.81	7.05	7.03
69	5.75	1.27	1.01	1.15	5.19	6.60	4.37
71	5.90	1.15	1.07	1.14	6.67	7.69	3.67
73	6.05	1.34	1.05	1.15	4.87	6.51	4.23
75	6.20	1.32	1.07	1.14	5.51	7.25	4.05
77	6.35	1.08	1.03	1.15	6.24	6.74	3.49
79	6.50	1.44	0.97	1.15	6.11	8.80	4.12
81	6.65	1.49	0.84	1.13	6.09	9.06	4.10
83	6.80	1.29	0.90	1.13	5.08	6.56	3.90

85	6.95	1.54	0.79	1.13	4.56	7.02	4.40
87	7.10	1.39	0.89	1.14	4.68	6.53	6.42
89	7.25	1.49	0.84	1.14	5.09	7.57	4.13
91	7.40	1.49	0.91	1.14	5.13	7.65	3.95
93	7.55	1.57	0.81	1.13	5.31	8.34	3.91
95	7.70	1.41	0.85	1.14	3.62	5.12	3.89
97	7.85	1.73	0.88	1.14	5.38	9.30	3.79
99	8.00	1.66	0.84	1.14	5.15	8.55	3.77
101	8.15	1.74	0.83	1.14	5.70	9.92	2.90
103	8.30	1.69	0.89	1.14	5.39	9.10	3.38
105	8.45	2.21	0.91	1.15	5.17	11.41	3.77
107	8.60	1.67	0.91	1.13	5.04	8.40	3.45
109	8.75	1.98	0.80	1.13	6.08	12.01	3.83
111	8.91	2.24	0.89	1.13	4.72	10.60	3.62
113	9.06	2.14	0.81	1.13	5.34	11.42	4.00
115	9.21	2.22	0.83	1.14	4.74	10.54	3.53
117	9.36	1.99	0.85	1.13	4.81	9.59	3.94
119	9.51	1.89	0.84	1.13	5.21	9.85	3.67
121	9.66	1.62	0.85	1.12	5.27	8.57	3.45
123	9.81	1.67	0.79	1.13	5.24	8.74	3.69
125	9.96	1.83	0.89	1.13	6.34	11.64	3.53
127	10.11	1.70	0.86	1.13	4.63	7.89	3.67
129	10.26	2.00	0.96	1.12	6.83	13.68	3.54
131	10.41	1.74	0.89	1.11	6.75	11.72	3.25
133	10.56	1.69	0.96	1.14	6.38	10.76	3.33
135	10.71	1.58	0.96	1.11	6.33	10.03	3.27
137	10.86	1.90	0.94	1.15	6.93	13.16	3.53
139	11.01	1.95	0.97	1.13	6.73	13.14	3.45
141	11.16	1.87	0.98	1.12	6.75	12.61	3.52
143	11.31	1.48	0.99	1.12	5.43	8.02	3.36
145	11.46	1.84	1.07	1.13	7.39	13.57	3.32
147	11.61	1.70	1.05	1.13	7.10	12.05	3.03
149	11.76	1.97	1.05	1.13	6.42	12.65	3.65
151	11.91	1.87	1.03	1.12	6.62	12.37	3.28
153	12.06	1.57	1.00	1.14	5.85	9.16	3.58
155	12.21	1.87	1.02	1.14	7.19	13.42	3.38
157	12.37	1.92	0.96	1.13	7.57	14.50	3.61
159	12.52	2.01	1.03	1.14	6.48	13.02	3.60
161	12.65	2.16	1.06	1.13	6.31	13.65	3.58
163	13.10	1.70	1.05	1.14	6.47	10.99	3.56
165	13.55	2.23	0.99	1.15	5.73	12.78	3.49
167	14.00	2.25	1.07	1.14	5.77	12.95	3.58

169	14.09	2.17	1.14	1.14	6.78	14.73	3.47
171	14.19	2.25	1.10	1.15	6.24	14.06	4.03
173	14.28	2.13	1.27	1.14	7.14	15.17	3.52
175	14.37	2.26	1.17	1.14	6.94	15.72	3.82
177	14.47	2.53	1.23	1.14	7.59	19.19	4.50
179	14.56	2.50	1.35	1.13	8.04	20.07	4.28
181	14.65	2.53	1.33	1.13	7.66	19.42	4.51
183	14.75	2.75	1.49	1.12	8.31	22.89	3.62
185	14.84	2.48	1.47	1.13	8.50	21.10	3.93
187	14.94	2.82	1.58	1.13	7.87	22.14	3.73
189	15.03	2.76	1.77	1.13	9.72	26.81	4.91
191	15.12	2.64	1.58	1.13	7.80	20.60	3.66
193	15.22	2.73	1.71	1.13	8.95	24.39	3.54
195	15.31	2.23	1.43	1.13	7.80	17.41	3.81
199	15.50	2.61	1.75	1.13	8.49	22.19	3.24
201	15.59	2.53	1.71	1.13	9.24	23.41	4.05
203	15.68	2.74	1.40	1.11	9.97	27.36	4.23
205	15.78	2.61	1.58	1.11	10.20	26.67	3.04
207	15.87	2.56	1.31	1.08	10.26	26.25	2.91
209	15.96	2.22	1.33	1.12	7.27	16.16	6.95
211	16.06	2.67	1.73	1.09	10.88	29.02	7.70
213	16.23	2.70	1.53	1.08	8.84	23.85	6.57
215	16.40	2.32	1.30	1.11	9.76	22.63	5.54
217	16.57	2.56	1.48	1.11	10.39	26.58	7.59
219	16.74	2.19	1.25	1.10	10.24	22.41	5.85
221	16.92	2.23	1.31	1.10	10.25	22.84	6.60
223	17.08	2.32	1.32	1.11	9.84	22.83	4.50
225	17.25	2.65	1.40	1.11	9.43	25.02	6.38
227	17.41	2.28	1.33	1.11	9.41	21.41	6.16
229	17.58	2.40	1.24	1.13	8.51	20.43	6.25
231	17.74	2.25	1.41	1.10	9.10	20.43	4.67
233	17.91	1.95	1.24	1.11	9.65	18.79	4.49
235	18.08	2.08	1.31	1.13	9.53	19.84	5.12
237	18.24	2.02	1.27	1.10	8.84	17.82	4.66
239	18.41	2.13	1.31	1.11	9.04	19.26	8.18
241	18.57	2.09	1.23	1.10	8.63	18.00	4.61
243	18.74	2.30	1.26	1.12	8.94	20.54	5.30
245	18.91	2.49	1.07	1.14	7.71	19.20	4.72
247	19.07	2.07	1.29	1.12	9.27	19.19	5.32
249	19.24	2.24	1.33	1.11	8.33	18.67	4.19
251	19.40	2.56	1.30	1.13	8.94	22.88	4.65
253	19.57	2.29	1.25	1.11	8.00	18.29	5.51

255	19.73	2.36	1.18	1.10	7.13	16.81	4.97
257	19.90	2.02	1.25	1.10	8.64	17.42	5.31
259	20.07	1.84	1.28	1.08	9.63	17.71	4.90
261	20.23	2.47	1.50	1.12	10.86	26.80	5.94
263	20.40	1.96	1.31	1.11	10.79	21.14	7.59
265	20.56	2.23	1.42	1.10	12.04	26.89	8.67
267	20.73	2.51	1.38	1.12	9.90	24.83	9.74
269	20.89	2.65	1.36	1.11	8.89	23.60	6.74
271	21.06	2.62	1.42	1.12	9.37	24.52	6.11
273	21.08	2.20	1.36	1.11	10.17	22.40	5.09
275	21.11	2.16	1.50	1.09	11.19	24.13	3.20
277	21.13	1.88	1.34	1.07	11.83	22.26	3.98
279	21.15	2.06	1.31	1.10	10.23	21.06	3.93
281	21.18	2.25	1.54	1.07	11.62	26.10	4.92
283	21.20	1.93	1.30	1.12	10.26	19.77	4.46
285	21.23	1.91	1.34	1.10	11.68	22.28	4.21
287	21.25	2.06	1.34	1.08	10.05	20.75	4.79
289	21.27	1.81	1.29	1.11	10.16	18.39	3.63
291	21.30	1.85	1.32	1.11	10.71	19.86	3.64
293	21.32	1.89	1.34	1.10	10.38	19.63	3.71
295	21.34	1.68	1.34	1.07	11.56	19.37	3.40
297	21.37	1.72	1.34	1.08	10.86	18.72	3.50
299	21.39	1.61	1.34	1.12	11.09	17.81	2.79
301	21.42	1.61	1.33	1.10	10.72	17.25	3.45
303	21.64	1.58	1.30	1.09	10.38	16.44	3.61
305	21.87	1.66	1.37	1.07	10.78	17.89	3.59
307	22.10	1.51	1.33	1.10	11.16	16.89	2.59
309	22.33	1.48	1.29	1.08	10.54	15.59	2.87
311	22.56	1.65	1.32	1.10	10.46	17.28	2.93
313	22.79	1.82	1.36	1.10	9.68	17.60	3.56
315	23.02	1.82	1.38	1.10	10.54	19.19	3.36
317	23.25	1.78	1.36	1.08	10.21	18.19	3.03
319	23.47	1.93	1.37	1.10	10.53	20.30	2.70
321	23.70	2.32	1.35	1.10	8.86	20.57	3.52
323	23.93	1.86	1.47	1.09	10.98	20.42	2.73
325	24.16	1.91	1.44	1.08	9.63	18.43	2.86
327	24.39	1.81	1.51	1.08	11.64	21.02	1.95
329	24.62	1.92	1.57	1.09	10.91	20.97	2.64
331	24.85	1.83	1.58	1.07	12.32	22.54	2.23
333	25.08	1.92	1.58	1.10	10.57	20.26	4.21
335	25.30	1.81	1.52	1.11	11.62	21.05	4.40
337	25.53	1.91	1.53	1.08	10.09	19.31	4.32

339	25.76	1.72	1.49	1.10	10.06	17.34	4.21
341	25.99	1.95	1.57	1.08	10.52	20.53	4.68
343	26.22	1.72	1.44	1.08	10.35	17.81	3.97
345	26.45	1.96	1.47	1.08	9.54	18.74	4.52
347	26.68	1.71	1.45	1.08	9.72	16.61	4.10
351	27.13	1.72	1.41	1.07	9.93	17.10	4.24
353	27.36	1.77	1.44	1.08	10.36	18.34	4.22
355	27.59	1.85	1.41	1.09	10.01	18.53	4.67
357	27.64	1.83	1.38	1.11	9.53	17.43	4.48
359	27.69	1.77	1.39	1.09	9.55	16.94	4.44
361	27.74	2.12	1.45	1.05	11.57	24.57	4.75
363	27.79	1.99	1.49	1.09	9.92	19.72	4.56
365	27.83	1.89	1.39	1.08	9.34	17.65	4.50
367	27.88	1.74	1.37	1.09	8.61	14.99	4.26
369	27.93	1.86	1.40	1.08	10.08	18.80	4.25
371	27.98	1.79	1.40	1.08	9.46	16.92	4.51
373	28.03	1.80	1.39	1.08	9.95	17.93	4.35
375	28.08	1.86	1.33	1.10	8.97	16.71	4.26
377	28.13	1.71	1.36	1.08	9.62	16.46	4.14
379	28.17	1.74	1.36	1.09	8.65	15.04	4.15
381	28.22	1.84	1.38	1.10	8.65	15.92	4.14
383	28.27	1.71	1.39	1.10	9.28	15.82	3.92
385	28.32	1.77	1.40	1.11	8.94	15.83	3.87
387	28.37	1.73	1.41	1.09	9.12	15.82	3.92
389	28.42	1.71	1.39	1.10	8.91	15.24	3.87
391	28.47	1.58	1.42	1.10	9.01	14.20	3.72
393	28.51	1.61	1.48	1.10	9.51	15.35	3.99
395	28.56	1.67	1.43	1.08	9.32	15.59	3.67
397	28.61	1.74	1.39	1.10	9.63	16.73	3.91
399	28.66	1.52	1.37	1.10	9.04	13.78	3.78
401	28.71	1.55	1.37	1.11	9.23	14.31	3.88
403	28.76	1.58	1.42	1.08	10.04	15.83	3.74
405	28.81	1.48	1.42	1.08	10.69	15.82	3.31
407	28.85	1.66	1.37	1.07	8.93	14.81	3.79
409	28.90	1.54	1.31	1.09	8.77	13.46	3.75
411	28.95	1.58	1.33	1.11	8.88	14.07	3.84
413	29.00	1.38	1.34	1.10	10.08	13.93	3.20
415	29.23	1.60	1.39	1.08	9.27	14.86	3.97
417	29.46	1.64	1.39	1.11	8.91	14.62	4.07
419	29.69	1.66	1.36	1.08	8.19	13.57	3.97
421	29.91	1.59	1.35	1.10	8.48	13.45	3.94
423	30.14	1.58	1.52	1.13	8.28	13.07	3.88

425	30.37	1.56	1.33	1.12	8.31	12.93	3.94
427	30.60	1.62	1.41	1.11	8.74	14.12	4.04
429	30.83	1.57	1.35	1.11	8.17	12.83	3.08
431	31.06	1.56	1.40	1.12	8.53	13.32	4.01
433	31.29	1.69	1.52	1.13	8.03	13.56	4.08
435	31.52	1.64	1.33	1.12	8.09	13.26	4.05
437	31.74	1.58	1.28	1.11	8.43	13.35	3.86
439	31.97	1.61	1.27	1.12	7.99	12.88	3.79
441	32.20	1.65	1.35	1.11	8.36	13.76	3.96
443	32.40	1.76	1.39	1.10	8.05	14.21	4.08
445	32.60	1.66	1.37	1.11	7.89	13.13	3.96
447	32.80	1.73	1.35	1.11	8.03	13.86	4.52
449	33.00	1.74	1.35	1.10	7.64	13.33	4.04
451	33.20	1.84	1.39	1.11	7.42	13.63	4.10
453	33.40	1.84	1.40	1.10	8.31	15.27	4.09
455	33.60	1.91	1.37	1.11	8.34	15.91	4.13
457	33.80	1.95	1.31	1.11	7.51	14.67	4.27
459	34.00	1.89	1.29	1.11	7.61	14.39	4.26
461	34.20	1.94	1.36	1.10	7.54	14.64	4.21
463	34.40	2.05	1.29	1.10	7.00	14.38	4.34
465	34.60	1.97	1.27	1.12	7.16	14.13	6.40
467	34.80	2.02	1.37	1.11	7.12	14.37	6.44
469	35.00	1.87	1.27	1.11	7.51	14.09	3.91
471	35.20	2.15	1.33	1.09	6.94	14.91	8.25
473	35.40	2.08	1.31	1.10	6.93	14.41	4.14
475	35.60	1.97	1.30	1.09	7.22	14.23	4.06
477	35.80	2.01	1.29	1.09	7.58	15.25	4.05
479	36.00	2.11	1.24	1.10	6.97	14.73	4.06
481	36.20	2.01	1.23	1.10	7.27	14.58	3.95
483	36.40	2.10	1.27	1.10	7.68	16.16	4.24
485	36.60	2.22	1.31	1.09	7.21	16.00	4.12
487	36.80	2.11	1.28	1.09	7.44	15.69	3.45
489	37.00	2.25	1.31	1.11	6.65	14.95	4.32
491	37.20	2.20	1.35	1.10	6.74	14.79	4.15
493	37.40	2.14	1.35	1.11	6.76	14.46	4.14
495	37.60	2.01	1.29	1.12	6.58	13.19	3.78
497	37.80	1.97	1.47	1.13	6.41	12.62	3.87
501	38.20	1.75	1.32	1.12	6.81	11.92	3.59
503	38.40	2.05	1.61	1.13	7.14	14.65	4.07
505	38.60	1.99	1.56	1.13	7.08	14.07	3.93
507	38.80	2.01	1.59	1.12	6.89	13.85	4.04
509	38.93	1.95	1.69	1.11	6.94	13.50	4.17

511	39.06	1.94	1.56	1.11	6.84	13.29	3.94
513	39.19	1.98	1.65	1.11	6.82	13.48	4.21
515	39.32	1.88	1.66	1.11	6.95	13.08	4.25
517	39.46	1.83	1.54	1.12	6.87	12.55	3.97
519	39.59	1.81	1.54	1.10	6.96	12.63	3.71
521	39.72	1.72	1.48	1.11	7.39	12.72	3.72
523	39.85	1.77	1.58	1.12	7.03	12.44	3.78
525	39.98	1.74	1.46	1.12	7.00	12.17	3.79
527	40.11	1.66	1.33	1.11	7.38	12.24	3.73
529	40.24	1.60	1.29	1.11	7.50	12.00	3.73
533	40.51	1.67	1.31	1.11	7.96	13.31	3.81
535	40.64	1.64	1.27	1.12	7.88	12.89	3.71
537	40.77	1.69	1.31	1.12	7.78	13.18	3.76
539	40.90	1.66	1.25	1.11	7.89	13.13	3.57
541	41.03	1.66	1.34	1.13	8.19	13.60	3.69
543	41.16	1.65	1.34	1.11	8.32	13.70	3.77
545	41.29	1.48	1.32	1.10	8.84	13.12	3.24
547	41.42	1.57	1.40	1.11	8.55	13.39	3.43
549	41.55	1.51	1.36	1.11	8.64	13.01	3.34
551	41.69	1.80	1.57	1.12	8.74	15.77	3.75
553	41.82	1.61	1.42	1.10	8.74	14.07	3.45
555	41.95	1.57	1.36	1.10	9.14	14.37	3.30
557	42.08	1.47	1.35	1.10	10.11	14.83	3.48
559	42.21	1.70	1.34	1.10	8.86	15.06	3.39
561	42.34	1.89	1.34	1.11	8.23	15.57	3.68
563	42.47	1.88	1.34	1.11	8.41	15.82	3.62
565	42.60	1.81	1.38	1.10	9.80	17.75	3.69
567	42.74	1.77	1.37	1.11	9.42	16.65	3.44
569	42.87	1.79	1.21	1.11	8.16	14.60	3.47
571	43.00	1.72	1.21	1.09	8.95	15.41	3.54
573	43.13	1.57	1.21	1.08	9.78	15.35	3.53
575	43.26	1.73	1.19	1.09	8.83	15.31	3.56
577	43.39	1.68	1.15	1.10	8.81	14.81	3.44
579	43.52	1.74	1.18	1.08	9.04	15.71	3.63
581	43.65	1.62	1.12	1.11	9.07	14.66	3.56
583	43.79	1.92	1.30	1.10	9.44	18.13	3.88
585	43.92	1.54	1.13	1.10	7.58	11.69	2.94
587	44.05	2.48	1.36	1.10	7.26	17.97	3.69
589	44.18	2.20	1.43	1.09	8.53	18.77	3.91
591	44.31	2.02	1.41	1.10	9.22	18.60	3.77
593	44.59	1.94	1.53	1.08	10.03	19.48	4.05
595	44.88	1.78	1.50	1.08	10.26	18.21	3.69

597	45.16	1.61	1.36	1.09	10.08	16.20	3.37
599	45.44	1.81	1.49	1.07	11.03	20.01	4.15
601	45.73	1.68	1.42	1.06	10.50	17.67	3.86
603	46.01	1.54	1.35	1.07	10.19	15.73	3.55
605	46.29	1.64	1.33	1.08	9.73	15.99	3.72
607	46.57	1.49	1.20	1.08	10.04	14.94	3.45
609	46.86	1.71	1.29	1.08	9.30	15.92	3.73
611	47.14	1.86	1.36	1.07	10.04	18.65	4.18
613	47.42	1.67	1.25	1.08	9.68	16.19	3.80
615	47.71	1.84	1.45	1.04	9.90	18.16	4.14
617	47.99	1.94	1.32	1.08	8.48	16.44	3.81
619	48.26	2.01	1.50	1.06	9.20	18.47	4.40
621	48.54	1.97	1.49	1.07	8.93	17.59	4.34
623	48.81	1.82	1.36	1.05	9.29	16.90	7.03
625	49.09	1.86	1.32	1.07	8.49	15.75	5.65
627	49.36	1.90	1.41	1.06	8.96	17.05	7.79
629	49.64	1.76	1.33	1.06	8.93	15.74	9.39
631	49.91	1.80	1.33	1.07	8.37	15.08	8.21
633	50.19	1.84	1.30	1.07	7.88	14.47	6.47
635	50.46	1.74	1.24	1.07	8.32	14.51	6.21
637	50.74	1.84	1.22	1.07	8.02	14.75	7.03
639	51.01	2.03	1.26	1.07	8.59	17.45	7.45
641	51.29	1.86	1.17	1.08	8.15	15.15	4.90
643	51.56	1.92	1.16	1.09	7.93	15.23	4.38
645	51.84	1.98	1.18	1.10	7.85	15.52	4.58
647	52.11	2.15	1.20	1.10	7.40	15.90	4.70
653	52.93	1.93	1.11	1.09	6.83	13.15	4.21
655	53.21	2.18	1.20	1.09	7.07	15.42	4.60
657	53.48	2.12	1.14	1.10	6.96	14.76	4.47
659	53.76	2.11	1.21	1.09	6.75	14.28	4.51
661	54.03	2.24	1.30	1.08	6.41	14.37	4.50
663	54.31	2.22	1.13	1.09	6.81	15.14	4.43
665	54.58	2.50	1.28	1.07	7.69	19.25	5.09
667	54.86	2.57	1.22	1.07	7.19	18.50	5.10
669	55.13	2.68	1.27	1.10	6.41	17.15	4.63
671	55.41	2.30	1.25	1.12	6.26	14.39	4.42
673	55.68	2.20	1.27	1.11	6.08	13.35	4.23
675	55.96	2.20	1.20	1.10	5.99	13.20	4.19
677	56.23	2.31	1.33	1.10	6.17	14.22	4.52
679	56.51	2.45	1.49	1.11	6.39	15.68	4.87
681	56.78	2.80	1.64	1.11	6.18	17.30	5.32
683	57.06	2.61	1.64	1.11	5.95	15.53	4.94

685	57.33	2.22	1.41	1.10	6.20	13.74	3.97
687	57.60	2.23	1.35	1.10	5.97	13.34	3.84
689	57.88	2.08	1.30	1.10	6.19	12.89	3.73
691	58.15	2.16	1.42	1.10	5.82	12.55	3.70
693	58.43	2.11	1.44	1.08	5.90	12.43	3.88
695	58.70	2.26	1.62	1.09	5.98	13.53	4.04
697	58.98	2.33	1.67	1.10	5.74	13.39	3.97
699	59.25	2.15	1.60	1.09	6.00	12.89	3.87
701	59.53	2.48	1.64	1.10	5.46	13.56	4.05
703	59.80	2.47	1.67	1.09	5.79	14.28	4.18
705	60.13	2.37	1.60	1.10	5.63	13.32	4.03
707	60.46	2.48	1.88	1.09	5.75	14.27	5.44
709	60.78	2.23	1.44	1.11	5.60	12.50	3.91
711	61.11	2.29	1.33	1.11	5.56	12.75	4.29
713	61.43	2.38	1.62	1.11	5.76	13.71	4.30
715	61.76	2.40	1.49	1.09	5.50	13.21	4.55
717	62.09	2.17	1.31	1.11	5.17	11.23	4.19
719	62.41	2.47	1.36	1.11	5.02	12.40	4.75
721	62.74	2.24	1.30	1.10	5.15	11.55	4.27
723	63.07	2.18	1.34	1.11	5.43	11.84	4.26
725	63.39	2.17	1.26	1.10	5.41	11.75	4.04
727	63.72	1.97	1.27	1.11	5.43	10.69	4.09
729	64.05	1.93	1.32	1.10	5.65	10.90	3.94
731	64.37	1.83	1.31	1.09	6.21	11.38	3.84
733	64.70	2.00	1.43	1.11	5.90	11.80	4.33
735	65.03	1.73	1.39	1.11	6.31	10.94	3.67
737	65.35	2.26	1.58	1.10	5.80	13.11	4.69
739	65.68	1.92	1.62	1.10	6.64	12.74	3.77
741	66.01	2.21	1.99	1.06	7.67	16.98	4.58
743	66.33	2.03	1.99	1.06	8.66	17.55	4.33
749	67.31	1.85	1.99	1.06	8.04	14.86	3.95
751	67.64	2.21	2.23	1.07	7.19	15.89	4.50
753	67.97	1.84	2.05	1.06	7.82	14.35	4.04
755	68.29	1.75	1.93	1.07	7.38	12.91	3.70
757	68.62	1.55	1.77	1.08	6.93	10.73	3.30
759	68.95	1.78	1.92	1.07	7.30	12.97	3.64
761	69.27	1.40	1.63	1.09	6.67	9.32	3.14
763	69.60	1.47	1.66	1.09	6.36	9.36	3.20
765	69.92	1.45	1.64	1.08	6.42	9.33	3.18
767	70.25	1.46	1.68	1.07	6.92	10.11	3.26
769	70.58	1.91	2.22	1.10	7.11	13.60	4.40
771	70.90	1.95	2.26	1.10	6.77	13.22	4.44

773	71.23	2.29	2.40	1.11	6.64	15.19	5.28
775	71.56	2.74	2.81	1.11	7.18	19.66	6.20
777	71.88	1.97	2.38	1.10	7.01	13.82	4.61
779	72.21	1.78	2.20	1.10	6.88	12.25	4.61
781	72.54	1.84	2.36	1.11	7.19	13.25	4.19
783	72.86	2.28	2.58	1.11	6.40	14.56	5.07
785	73.17	1.90	2.47	1.10	6.32	12.00	5.21
787	73.49	1.71	2.29	1.09	6.63	11.37	5.03
789	73.81	1.44	2.10	1.12	6.65	9.58	4.30
791	74.13	1.38	2.11	1.11	6.17	8.49	3.70
793	74.45	0.95	1.67	1.07	6.40	6.06	3.21
795	74.77	0.88	1.59	1.08	6.69	5.90	2.58
797	75.08	0.88	1.58	1.08	6.70	5.92	3.05
799	75.40	0.84	1.64	1.09	6.79	5.72	3.00
803	76.04	0.89	1.62	1.07	6.95	6.18	3.05
805	76.36	0.91	1.67	1.08	7.00	6.37	2.67
807	76.68	0.95	1.57	1.10	6.91	6.55	3.11
809	76.99	0.94	1.53	1.06	7.00	6.58	3.20
811	77.31	0.93	1.53	1.07	7.15	6.65	3.17
813	77.63	0.88	1.54	1.08	7.13	6.28	3.05
815	77.95	0.88	1.48	1.08	7.06	6.18	3.04
817	78.27	0.97	1.67	1.08	6.75	6.53	3.22
819	78.59	1.01	1.78	1.07	6.64	6.74	3.21
821	78.91	1.12	2.01	1.08	6.68	7.45	3.43
823	79.22	0.98	1.79	1.08	6.30	6.18	2.85
825	79.54	1.10	1.94	1.08	6.41	7.05	3.12
827	79.86	1.12	2.03	1.08	6.06	6.81	3.41
829	80.18	1.12	2.19	1.09	5.61	6.31	3.31
831	80.50	1.07	1.79	1.10	5.72	6.10	2.90
833	80.82	1.07	2.03	1.09	5.08	5.43	3.10
835	81.13	1.38	2.81	1.09	4.74	6.55	4.19
837	81.45	1.21	2.75	1.08	4.74	5.73	3.74
839	81.77	1.22	3.03	1.09	4.63	5.64	3.70
841	82.09	1.26	3.53	1.09	4.80	6.05	3.56
843	82.41	1.26	3.68	1.08	4.95	6.21	3.65
845	82.73	1.30	5.13	1.06	4.90	6.36	3.44
847	83.04	1.52	7.36	1.05	4.39	6.69	3.53
849	83.36	1.78	10.26	1.04	3.96	7.04	3.59
851	83.68	2.01	14.66	1.07	3.42	6.86	3.56
853	84.00	2.96	28.78	1.02	2.61	7.72	3.58
855	84.32	1.86	12.73	1.04	3.19	5.93	3.31
857	84.64	1.32	5.52	1.05	4.33	5.70	3.23

859	84.96	1.03	2.10	1.06	5.04	5.21	2.99
861	85.27	1.05	2.16	1.06	5.05	5.32	3.17
863	85.59	1.07	1.78	1.08	4.76	5.10	3.26
865	85.91	1.09	2.20	1.06	4.84	5.29	3.18
867	86.23	1.32	1.66	1.08	3.91	5.15	3.84
869	86.55	1.11	1.78	1.08	5.04	5.57	3.25
871	86.87	1.12	1.56	1.08	4.27	4.79	3.31
873	87.18	0.99	1.56	1.08	4.69	4.63	2.95
875	87.50	1.65	1.64	1.09	3.60	5.96	5.12
877	87.82	1.02	1.46	1.07	4.73	4.81	3.33
879	88.14	0.99	1.42	1.07	4.82	4.78	3.26
881	88.46	0.86	1.22	1.08	5.20	4.48	2.91
883	88.78	0.90	1.34	1.06	5.16	4.65	3.07
885	89.09	0.88	1.08	1.09	4.41	3.88	3.26
887	89.41	0.88	1.09	1.09	4.48	3.95	3.18
889	89.73	1.07	1.21	1.09	4.54	4.86	3.87
891	90.05	0.80	1.20	1.07	4.52	3.61	2.79
893	90.37	0.80	1.30	1.08	4.48	3.58	2.88
895	90.69	0.85	1.39	1.08	4.24	3.62	3.02
897	91.01	0.86	1.40	1.08	4.11	3.54	3.10
899	91.32	0.87	1.42	1.09	4.03	3.49	3.13
901	91.64	0.94	1.43	1.07	4.04	3.82	3.45
903	91.96	0.95	1.21	1.07	3.81	3.60	3.37
905	92.28	0.93	1.13	1.09	3.63	3.38	3.29
907	92.60	0.91	1.18	1.08	3.58	3.27	3.21
909	92.92	0.93	1.16	1.10	3.56	3.32	3.31
911	93.23	0.93	1.14	1.09	4.08	3.78	3.15
913	93.55	0.97	1.24	1.09	3.75	3.63	3.36
915	93.87	0.96	1.11	1.10	3.70	3.53	3.42
917	94.19	0.97	1.27	1.09	3.79	3.68	3.24
919	94.51	0.98	1.28	1.08	3.66	3.57	3.22
921	94.83	0.94	1.33	1.10	3.58	3.35	3.14
923	95.14	0.89	1.25	1.08	4.78	4.25	2.69
925	95.46	0.96	1.31	1.07	4.28	4.11	3.33
927	95.78	1.02	1.49	1.07	4.30	4.37	3.44
929	96.10	1.00	1.39	1.10	4.06	4.04	3.43
931	96.42	0.79	1.08	1.10	4.67	3.71	2.53